THE UNIVERSITY OF CHICAGO

SIMULATING PHYSICAL PROCESSES IN THE ACTIN CYTOSKELETON

A DISSERTATION SUBMITTED TO
THE FACULTY OF THE DIVISION OF THE PHYSICAL SCIENCES
IN CANDIDACY FOR THE DEGREE OF
DOCTOR OF PHILOSOPHY

DEPARTMENT OF PHYSICS

BY
SIMON FREEDMAN

CHICAGO, ILLINOIS
DECEMBER 2018

For Ellen, who made it all possible. For Mom and Abba, for unending encouragement.

TABLE OF CONTENTS

LIST OF FIGURES

LIST OF TABLES

ACKNOWLEDGMENTS

My parents sent me to an advanced physics class in the summer after 8th grade (I wanted to do chemistry, because explosions, but it was full). My math skills weren't really on par with my camp-mates, and I was lost from the first day onward when we were discussing significant figures. But I remember being mesmerised by the teacher swinging a bucket of water 360° and nothing falling out- so their plan might have worked. My parents are always there to give me a push in the right direction, and encourage trying new things and failing; they claim its more fun. They continue to be an inspiration, by composing musicals, performing piano recitals, running nation-wide research surveys, and writing in academic journals, all between seeing patients. Living nearby them and my siblings, has made my PhD significantly easier, as they're always ready to provide us with a meal or take the kids.

I've also had many encouraging and helpful academic mentors. At Fasman Yeshiva High School, Rabbi Shmuel Weiss presented calculus and precalculus with clarity that gave me a solid foundation, while keeping the math fun. In college (Illinois Tech) I had many fun and engaging professors, including Prof. Ed Reingold, who pushed me to go into research, and whose Discrete Math class introduced me to many new problem solving methods and ways of thinking. Prof. Hugh Scott got me interested in both classes he taught, Statistical Mechanics and Biophysics, and helped me see that physics needn't concern quarks or galaxies, but could be used as a toolkit to solve open problems in biology. By showing some of his research in class (simulations of lipid membranes) he introduced me to computational biophysics, and subsequently helped me find a lab at IIT to do research.

In graduate school I've benefited from being immersed in an outstanding research environment, with classmates and lab mates who are extremely helpful to bug with questions and bounce ideas off, and are generally fun people to be around. I've had brilliant but helpful postdoc mentors, Shiladitya Banerjee and Glen Hocky, who I could always bother with questions on physics, biology, or how to navigate the academic world, as well as awesome experimental collaborators in the Gardel group, including Sam Stam and Kim Weirich. Prof.

Margaret Gardel introduced me to actin in her Biophysics course in my first year, and since then has always been available to help me figure out interesting angles and analyses for my research. I've enjoyed my conversations with Prof. Murugan about machine learning and its applications to biophysics, and greatly benefited from his feedback on my thesis. I am also thankful to Prof. Son who lucidly taught Statistical Mechanics in my first year, and has had encouraging and helpful feedback on my thesis. Mostly, I've benefited from having a patient and helpful thesis advisor, Aaron Dinner, who always has an open door, and has provided thorough guidance from algorithm development to presenting data to writing papers to getting a postdoc. Aaron manages to teach and advise while treating his students like peers, gives us freedom to explore but always provides sufficient direction. I feel extremely priveleged to have gone to graduate school at the University of Chicago and pursued my PhD in the Dinner Group.

I could not have done a PhD without the constant support of Ellen May, my amazing wife, who keeps us afloat financially, and doesn't ignore our two children. I am thankful everyday for her constant love, support, encouragement, and ability to make me laugh. My kids make it fun to come home, and arguing with Sarah's two-year-old logic has definitely honed my skills in responding to peer-reviewers. My nine-month-old Talia teaches the other approach: "scamper away and never let them hold you"; I'm sure that will be useful in the future too.

To echo Herbert Goldstein [57], תושלב"ע.

ABSTRACT

The actin cytoskeleton is a network of proteins that provides infrastructure for a cell to maintain its shape, divide, transmit forces and enable intracellular transport. We developed and benchmarked a computer program, AFINES, that can accurately simulate the mechanical and kinetic components of this network, including semi-flexible filaments, crosslinkers that bind filaments into force propagating networks, and motors that enable filament sliding and network contraction. Motivated by recent *in vitro* experiments that controllably combine actin filaments, myosin motors, and crosslinkers, and generate broad structural diversity, we use our simulation to systematically vary molecular properties and densities and outline new structural phase spaces accessible to these assemblies. We test the possible biophysical function of different structures and show tunability of network viscoelasticity and motor transport dynamics. We also elucidate the microscopic processes that produce global contractility in actomyosin assemblies with varying stiffnesses and determine how the mechanical and kinetic properties of filaments and crosslinkers contribute to crosslinker sorting. Together, these results demonstrate how a parameterized computational model can efficiently motivate future experiments and determine the underlying physics of a complex biophysical system.

CHAPTER 1

INTRODUCTION

Biological cells exhibit an enormous range of mechanical and dynamical behaviors, such as division, motility, and shape maintenance, which rely on the collective behavior of millions of proteins. Understanding how biomolecules produce these mechanisms can benefit medicine, for example, in determining how cancer cells become motile and metastasize [184], and how to control cell shape and fate in embryonic stem cell development [53]. Additionally, this understanding could enable the design of active biomimetic materials that yield a desired response to an energetic perturbations [108].

Broadly, we are interested in developing maps between the underlying biochemical behavior of microscopic entities, the molecules in cells, to macroscopic mechanical and dynamic properties of the cell. In large systems with trivial pairwise interactions, statistical mechanics can be used to solve these types of problems; for example, one can calculate the temperature of an ideal gas from the mass and average speed of the particles [1]. Complex pairwise interactions, such as those present between molecules in the cell, make it difficult to determine macroscopic state characteristics, either because they are difficult to describe mathematically as functions of thermodynamic variables, or because those equations cannot be solved analytically. Furthermore, the macroscopic state of a system may rely on mesoscale mechanisms, such as molecules binding to each other to form complexes.

Using computer simulation, one can describe a system with arbitrarily complex interparticle interactions, and evolve the state of the system in time to discover and analyze the macroscopic system behaviors. In this work, I use computer simulation to generate the collective behavior of a group of molecules that compose the actin cytoskeleton, a specific structural component of cells responsible for many of its materials properties. I then use tools from statistical mechanics to analyze the trajectories that yielded these behaviors, determine their underlying mesocopic mechanisms, and the relationships between constituent components and macroscopic state. In the remainder of this introduction, I provide a short

background to the molecular system, the computational approaches we use in modeling and simulation, and recent progress in understanding how physical processes emerge in cytoskeletal networks.

1.1 Actin and Actin Binding Proteins

Actin exists as a $(\sim 5\text{nm})^3$ monomer, G-actin (globular actin), and a polymer, F-actin (filamentous actin) [104]. The monomer has a somewhat triangular shape, with two lobes separated by a cleft, which results in the polymer having polarity: subunits all point in the same direction, so one end of the filament is pointed, in that the cleft is in contact with the rest of the filament, and one end is barbed, in that the cleft is in contact with the surrounding medium [104]. This polarity has implications for polymerization, as actin monomers are added at a significantly higher rate to the barbed ("+") end than the pointed ("-") end due to the cleft's ability to bind ATP/ADP, and has implications for interactions with other proteins, such as myosins (described below) [104]. F-Actin filaments have further substructure, in that they consist of two twisted polymer strands, with the full twist consisting of 13 monomer subunits [48].

The length of actin filaments depends on the molecular composition of its surrounding medium, but in the absence of inhibiting factors, filaments can grow to ~ 10 μm long, but remain thin with a diameter ~ 6 nm [48, 30]. Mechanically, filaments are worm-like chains, or nearly inextensible but bendable [30]. The length scale that characterizes the bending rigidity is called the persistence length (L_p), and is the contour length at which tangent vectors to the polymer are completely decorrelated; for actin, $L_p = 17$ μm, meaning longer (~ 10 μm) filaments bend via thermal fluctuations, while shorter (~ 1 μm) filaments require significant force to bend [131].

Many proteins (so called actin binding proteins, or ABPs) bind to actin filaments. One class of ABPs are crosslinkers, which typically have two actin binding sites, and thus can connect two filaments [104]. Short crosslinkers tend to bind pairs of filaments into bundles.

Whether or not the bundle maintains the filament's polarity depends on the crosslinker; fimbrin or fascin, for example, only bind parallel actin filaments, thereby yielding a polar bundle, while others (such as α-actinin) bundle filaments regardless of polarity [183, 159]. Bundles are significantly more rigid than filaments (since for a rod of thickness d, $L_p \propto d^4$ [56]), and therefore enable actin to have diverse mechanical behavior. For example, polar bundles may use polymerization to push against the cell membrane and form protrusions (filopodiae) that can act as anchors for a motile cell (Fig. 1.1A) or enable cell scale structural characteristics, such as the erectedness of a sensory (Fig. 1.1C). Thicker, non-parallel bundles can form stress fibers that maintain a cell's shape in cytoskeletal networks such as the lamellum (Fig. 1.1A,B). Larger crosslinkers, such as filamin (150 nm), can crosslink without bundling, and yield disorganized mesh like structures such as the cell cortex [149](Fig. 1.1D).

ABPs often have characteristics beyond crosslinking; for example, cofilins promote severing of actin filaments [70], while formins promote actin polymerization [104]. The Arp 2/3 complex binds to actin at a 70° angle, and promotes polymerization, yielding branched actin networks which compose a network at the leading edge of motile cells called the lamellopodium (Fig. 1.1A,B) [136]. A broad range of active, structural characteristics are driven by myosins, a class of ABPs that are also molecular motors.

Myosins exert force on actin filaments through the sliding crossbridge mechanism [71]. In this process, the head domain of a myosin molecule binds to an actin filament, and unbinds via ATP hydrolisis in a way that propels the head toward the barbed end of the actin filament [104]. Subsequent rebinding of the myosin molecule to actin pulls the actin filament with respect to the tail domain of the myosin molecule (or, from the reference frame of the actin filament, the myosin walks toward the barbed end) [104]. A common isoform of myosin molecules is myosin II, in which the tails of two myosin molecules entangle to yield a myosin dimer. In muscle cells, myosins aggregate further, via tail-domain entanglement, and myosin dimers form myosin thick filaments, which can have dozens to hundreds of actin binding sites [120]. Myosin thick filaments can thus exert significant force on multiple actin

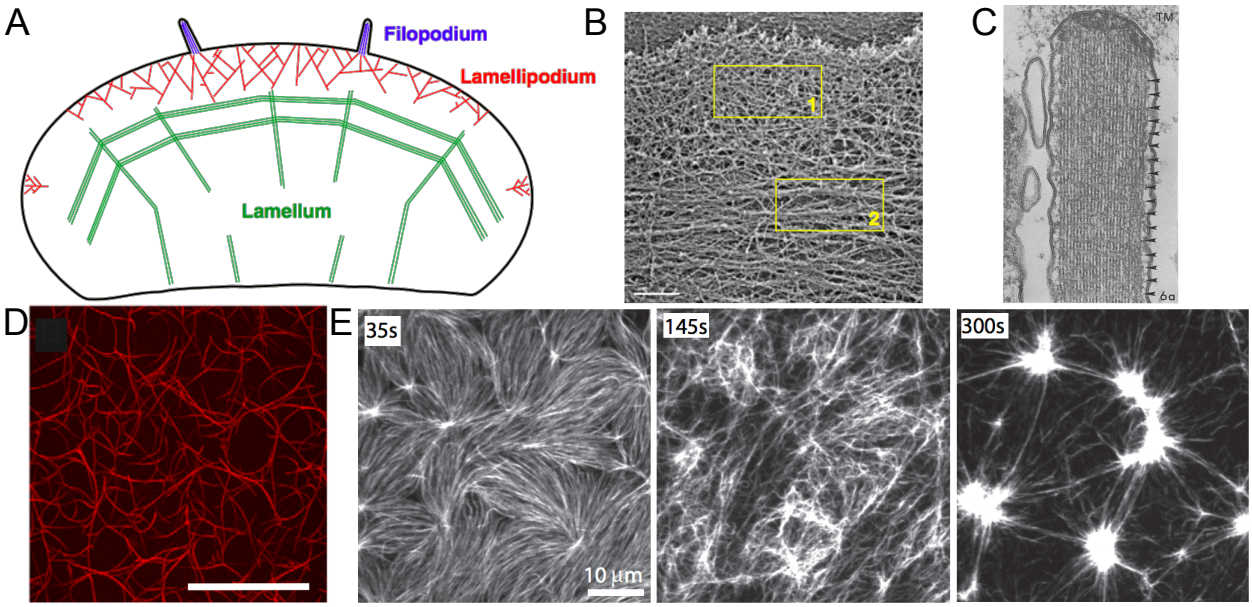

Figure 1.1: Actin filaments build diverse networks and exhibit active dynamics. (A) Examples of actin networks in a migrating, metazoan cell, including filopodiae protrusions at the edge of the cell that emerge from actin polymerizatoin, and fascin bundling; the lamellipoduium, a branched network of actin filaments which results from actin interacting with the ARP 2/3 complex, amongst other ABPs necessary for mechanosensing; and the lamellum, a structure formed primarily of actin and α-actinin, which forms stress fibers that can maintain a cell's shape. Adapted from Ref. 113. (B) Electron micrograph image of lamellopodium (area 1) and lamellum (area 2). Scale bar is 1 μm. Adapted from Ref. 17. (C) Transmission electron micrograph of actin by the ABP fimbrin in an auditory hair cell. Scale bar is 0.1 μm. Adapted from Ref. 166. (D) Network of actin and filamin reconstituted *in vitro*. Scale bar is 100 μm. Adapted from Ref. 149. (E) An entangled quasi-2D actin network reconstituted *in vitro*. Upon the addition of muscle myosin II, the network contracts. Adapted from Ref. 123

filaments simultaneously, as they can bind at multiple points to different filaments.

1.2 Coarse Grained Molecular Dynamics Simulation

At the time of this writing, the largest atomistic protein simulations capture dynamics on time scales of miliseconds and system-size scales of 10^6 atoms, including solute and solvent. In a 1 μm actin filament there are 10^6 atoms, and cytoskeletal dynamics occur at cellular length scales, with thousands of actin filaments that can be micrometers long, immersed in solvent, and interacting with tens of thousands of binding proteins. Thus, to simulate a

cytoskeletal network, one must reduce the number of components in the system, or develop a coarse grained representation. We briefly outline our technique here; for a more detailed explanation see Chapter 2, Materials and Methods.

We reduce the number of simulation components by representing the actin and ABPs as mechanical objects with a small number of beads (points in space whose position is tracked): actin filaments (~ 10 beads), crosslinkers (2 beads) and motors (2 beads). Typical simulations have hundreds of filaments, hundreds of motors, and thousands of crosslinkers, yielding 10^4 beads. Since these objects are large, the characteristic time scales for their interactions is also significantly larger than for atoms, which enables us to simulate these systems for hundreds of seconds.

The trajectories and interactions of individual molecules in these systems are then determined using Langevin dynamics, a phenomonological equation for incorporating the surrounding medium's viscosity and temperature into its force balance [148]. Viscosity is incorporated as a damping force, proportional to the object's velocity, in order to approximate the fluid in which the object is immersed and temperature is incorporated via a thermostat, in this case a Brownian perturbation to the objects' positions. The forces which must be balanced against viscosity and temperature effects stem from mechanical characteristics of the molecules, such as their rigidity and size.

Additional characteristics of the trajectories are included using Markov processes, and other agent-based approaches. For example, crosslinker binding and unbinding is incorporated by ascribing a state to a crosslinker of being bound or unbound to a filament, and detailing the rules for binding. The rules for unbinding are then determined using the principle of detailed balance, and transition probabilities between states are determined using the Metropolis algorithm [112]. Unlike crosslinkers, motors are considered non-equilibrium entities; when bound they move along actin filaments, toward their barbed end, at tension dependent speeds [126]. Furthermore, these objects can form complexes: when motors and crosslinkers are bound to filaments, their forces are propogated onto the filaments to which

they are bound. This approach which models molecules as physical entities can be used to determine how the proteins in actin networks combine to form active materials.

1.3 Cytoskeletal Actin Networks

The cytoskeleton of muscle cells is organized; anti-parallel actin bundles are slid toward each other by myosin thick filaments yielding muscular contraction [71]. However, in non-muscle cells, actin does not exhibit global organization or alignment, and yet myosin driven contraction can still yield diverse active material behaviors, such as enabling a cell to reshape in response to the mechanical properties of its environment [34], constrict into two daughter cells during cell division [154], and pull its trailing edge forward during cell migration [136]. How do these biophysical phenomena emerge from seemingly disorganized assemblies of proteins?

In this work, I address four aspects of this question.

1. Given a particular subset of ABPs, with known shapes and kinetics, what structures can those ABPs form?

2. What biophysical function might a particular structure have in a cellular environment?

3. What mesoscale mechanisms bridge the gap between the properties of the underlying molecular components and the macroscopic structure or dynamics of an actin assembly?

4. If structures depend on particular subsets of ABPs, what mechanisms are at play to sort those ABPs to their correct spatial location?

These questions have been at the center of many experimental, theoretical, and computational works over the past half century. In experiment, one can isolate specific cytokseletal proteins from the cell and reconstitute networks *in vitro* to determine the structure and dynamics of a particular subset of molecular components [7, 123, 120, 159]. For example, adding the crosslinker filamin may yield a mesh-like network of actin bundles, at particular actin

and crosslinker densities (Fig. 1.1D), while combining it with muscle myosin II contracts the initially homogenous distribution of actin into dense aggregates. Thus, these experiments have been extremely useful in determining the necessary components for cellular actin networks, such as the dependence of actomyosin contractility on crosslinker density [7, 123] (see Chapter 3 for more examples).

As these networks exhibit dynamics, they are typically imaged through fluorescence microscopy. Thus it is possible to observe how the bulk material changes, but difficult to observe the molecular interactions that yield these changes, since they happen at length scales below the diffraction limit. Nevertheless, extensive image analysis can be used to extract dynamical quantities and biophysical function from these experiments, such as anomalous diffusion of motors on cytoskeletal networks [164] and the velocity flow field of actin [120]. Additionally, experimental techniques such as oscillatory shear, have been useful in determining the biophysical function of such networks, such as their viscoelastic response to mechanical perturbation [51, 78]. Careful imaging techniques, such as sparse labeling of actin filaments, have also made it possible to extract dynamic mechanisms from experiments, such as filament buckling, which was shown to be a necessary mechanism in actomyosin contractility [123]. Recent experiments have also used isolated systems to exhibit passive and signal-driven sorting of ABPs [183].

Computational models and theories, while prone to approximations, enable significantly more control over and observation of these materials. Many theoretical models treat the cytoskeleton as an active gel: a continuous material that incorporates the non-equilibrium forces from myosin motors and actin polymerization and the non-constant connectivity generated by ABPs [139]. These models enable predicting biophysical function from thermodynamic constraints, such as the total stress on a network, as one can directly extract or calculate viscoelastic properties of materials [65, 89, 5]. Additionally, they have recently been used to exhibit more complex active dynamics, such as actomyosin contractility [142]. However, it is difficult to parse the connection between the molecules that comprise the

network and the resultant material.

An alternative to this approach are coarse-grained molecular models, described above. These simulations enable independent modification of ABP properties that is not typically possible in experiment; i.e., if one wanted to experimentally test how network dynamics varied based on the size of a crosslinker, then they could use different crosslinkers, but these might bind to actin at different rates. In simulation size and binding affinity can be parameterized and tuned independently, enabling one to directly test hypotheses about the mechanical and kinetic molecular properties that lead to larger materials properties. These simulations also allow one to rapidly explore a large number of initial conditions, which is difficult in experiment, as each ABP may have a different procedure for extraction and fluroescent labeling. The output of these simulations are typically the trajectories and states of the individual molecular components, enabling one to easily measure dynamical quantities without image analysis.

Coarse-grained molecular models have become useful tools for exploring cytoskeletal dynamics over the past 20 years. Most prominently, the Cytosim software package has been used extensively to simulate microtubule networks, a cytoskeletal network that also includes motors and filaments (albeit with slightly different properties than actin) and determine conditions under which microtubules combine to form asters, vortices, or active nematics [124, 126]. These simulations rely heavily on approximations to the mechanical and kinetic properties of their components, and a challenge in their development is determining the appropriate experimental regime where they are applicable. Thus, despite the similarities between microtubule and actin cytoskeletal networks, since actin filaments are significantly more flexible and form different structures than microtubules, it is not immediately clear that Cytosim could be used to explore the actin cytoskeleton (although see Refs. 35, 6 for recent applications).

We determined a set of biophysical benchmarks for a coarse-grained model of the actin cytoskeleton, based on well-understood material properties and experiments involving actin

filaments, myosin motors, and actin crosslinkers, and built our own computational model, described in Chapter 2, so that it could pass those benchmarks (see the Supplemental Information of that chapter for a detailed comparison with Cytosim). In Chapter 3 we show how using simulation, one can independently test the effect of varying individual kinetic and mechanical characteristics of actin binding proteins, and systematically sweep through large swaths of parameter space, to determine the structures accessible to mixtures of actin filaments, motors, and crosslinking proteins. In Chapters 4 and 5, we use the simulation to solve outstanding experimental problems. In Chapter 4, we use simulation to reproduce a surprising experimental example of actomyosin contraction, test dependence of contractility on network connectivity and filament rigidity, and measure the underlying filament interactions that make the network contractile. In Chapter 5, we form a thermodynamic model to explain the observation that bundling crosslinkers sort into domains in a single actin bundle, and test the model by varying its parameters in simulation, and comparing our results with experiments. Taken together, we show that simulation can play an integral role in understanding the complex mechanical and kinetic behavior in the actin cytoskeleton.

CHAPTER 2

A VERSATILE FRAMEWORK FOR SIMULATING THE DYNAMIC MECHANICAL STRUCTURE OF CYTOSKELETAL NETWORKS

This chapter was originally published as Ref. 44 with coauthors Shiladitya Banerjee, Glen Hocky, and Aaron Dinner.

Computer simulations can aid in understanding how collective materials properties emerge from interactions between simple constituents. Here, we introduce a coarse-grained model that enables simulation of networks of actin filaments, myosin motors, and crosslinking proteins at biologically relevant time and length scales. We demonstrate that the model qualitatively and quantitatively captures a suite of trends observed experimentally, including the statistics of filament fluctuations, mechanical responses to shear, motor motilities, and network rearrangements. We use the simulation to predict the viscoelastic scaling behavior of crosslinked actin networks, characterize the trajectories of actin in a myosin motility assay, and develop order parameters to measure contractility of a simulated actin network. The model can thus serve as a platform for interpretation and design of cytoskeletal materials experiments, as well as for further development of simulations incorporating active elements.

2.1 Introduction

The actin cytoskeleton is a network of proteins that enables cells to control their shapes, exert forces internally and externally, and direct their movements. Globular actin proteins (G-actin) polymerize into polar filaments (F-actin) that are microns long and nanometers thick. Many different proteins bind to actin filaments; such proteins often have multiple binding sites that enable them to crosslink actin filaments into networks that can transmit force. Myosin proteins are composed of head, neck, and tail domains and aggregate via their tails to form minifilaments that can attach multiple heads to actin filaments [128].

Each myosin head can bind to actin and harness the energy from ATP hydrolysis such that a minifilament can walk along an actin filament in a directed fashion—i.e., it is a motor. These dynamics have been extensively studied, and it is well understood, for example, how they give rise to muscle contraction. In muscle cells, myosin II minifilaments bind to regularly arrayed antiparallel actin filaments and walk toward the barbed ends [71]. In other types of cells lacking this level of network organization, however, the ways in which the elementary molecular dynamics act in concert to give rise to complex cytoskeletal behaviors remain poorly understood.

Addressing this issue requires a combination of experiment, physical theory, and accurate simulation. The last of these is our focus here—we present a nonequilibrium molecular dynamics framework that can be used to efficiently explore the structural and dynamical state space of assemblies of semiflexible filaments, molecular motors, and crosslinkers. By allowing independent manipulation of parameters normally coupled in experiment, this computational model can guide our understanding of the relationship between the microscopic biochemical protein-protein interactions and the macroscopic mechanical functions of assemblies. Additionally, because the model simulates filaments, motors, and crosslinkers explicitly, we can elucidate microscopic mechanisms by studying its stochastic trajectories at levels of detail that are experimentally inaccessible. The fact that complex behaviors can emerge from simple interactions also allows simulations to be used to evaluate predictions from theory.

In this work we detail the model and demonstrate that, it reproduces an array of known experimental results for actin filaments, assemblies of actin and crosslinkers (passive networks), and assemblies of actin and myosin (active networks). We go further to provide new experimentally testable predictions about these systems. For single polymers, we reproduce the spatiotemporal fluctuation statistics of actin filaments. For passively crosslinked networks, we reproduce known stress-strain relationships and predict the dependence of the shear modulus on crosslinker stiffness. For active networks, we reproduce velocity distributions of actin filaments in myosin motility assays and show how one can

tune their dynamical properties by varying experimentally controllable parameters. In separate studies, we use the model to clarify microscopic mechanisms of actomyosin contractility and investigate how assemblies of actin filaments and crosslinkers can be tunably rearranged by myosin motors to form structures with distinct biophysical and mechanical functions [159]. The collection of this benchmark suite is itself useful, as prior models [106, 65, 181, 80, 29, 36, 177, 126, 35, 59, 79] have focused on specific cytoskeletal features, making the tradeoffs needed to capture the selected behaviors unclear.

Indeed, our model builds on earlier studies, which we briefly review to make clear similarities and differences of the models (see also [137] for a list of cytoskeletal simulations). The most finely detailed simulations focus on the motion of a myosin minifilament with respect to a single actin filament. Erdmann and Schwarz [36] used Monte Carlo simulations to verify a master equation describing the attachment of a minifilament and, in turn, the duty ratio and force velocity curves as functions of the myosin assembly size. Stam et al. [158] used simulations to study force buildup on a single filament by a multi-headed motor and found distinct timescale regimes over which different biological motors could exert force and act as crosslinkers. These models of actin-myosin interactions are important for understanding the mechanics at the level of a single filament, and their results can be incorporated into larger network simulations.

A number of publications have dealt with understanding the rheological properties of crosslinked actin networks [106, 65, 181, 80]. For example, to study the viscoelasticity of passive networks, Head et al. [65] distributed filaments randomly on a two-dimensional (2D) plane, crosslinked filament intersections to form a force-propagating network, sheared this network, and let it relax to an energy minimum. From this model, they were able to identify three elastic regimes that were characterized by the mean distance between crosslinkers and the temperature. Dasanyake and coworkers [29] extended this model to include a term in the potential energy that corresponded to myosin motor activity and observed the emergence of force chains that transmit stress throughout the network. These studies address questions

about how forces propagate and how crosslinker densities alter mesh stiffness.

Other studies characterized network structure and contractility as functions of model parameters. Wang and Wolynes [177] considered a graph of crosslinkers (nodes) and rigid filaments (edges) in which motor activity was simulated via antisymmetric kicks along the filaments. They calculated a phase diagram for contractility as a function of crosslinker and motor densities. Such a simulation can provide qualitative insights into general principles of filament networks, but the model did not account for filament bending, and structures were sampled via a Monte Carlo scheme that was not calibrated to yield information about dynamics. Cyron et. al. [28] used Brownian dynamics simulations to investigate structures that can form via mixtures of semiflexible filaments and crosslinkers and determined a phase diagram and phase transitions [117] between differently bundled actin networks that form as one varies crosslinker density and crosslinker-filament binding angle. Nedelec and coworkers performed dynamic simulations of assemblies of semiflexible microtubules and kinesin motor proteins, which share features with assemblies of F-actin and myosin; they used their simulation package, CytoSim, to understand aster and network formation in microtubule assays [126] and showed recently that the model can be adapted to treat actin networks [35]. Gordon et al. [59], Kim [79], and most recently Popov et al. [137] similarly simulated dynamics of F-actin networks and included semiflexible filaments, motors and crosslinkers. By varying motor and crosslinker concentrations, Gordon et al. [59] and Popov et al. [137] showed various structures that can emerge from assemblies of this type, and Kim [80, 79] additionally quantified how these changes could effect force propagation within the network.

We have strived to include many of the best features of these preceding models in our model. We use the potential energy of Head et al. [65] for filament bending and stretching. However, in contrast to [65, 29], which simply relax the network, we simulate the stochastic dynamics, including thermal fluctuations, crosslinkers and motors binding and unbinding, and the processive activity of myosin. The force propagation rules and kinetic equations for binding and unbinding are similar to those of [126, 59], while the length and time scales

simulated are on the order of those performed in [79, 35]. We expand on these works by combining and documenting key elements in a single model, demonstrating that the model can capture experimentally determined trends for cytoskeletal materials quantitatively, and illustrating how the model can be used to study systems of current experimental interest.

2.2 Materials and Methods

To access the time and length scales relevant to cytoskeletal network reorganization, we treat actin filaments, myosin minifilaments, and crosslinkers as coarse-grained entities (Fig. 2.1A). We model actin filaments as polar worm-like chains (WLC) such that one end of the WLC represents the barbed end of an actin filament and the other represents the pointed end. We model crosslinkers as Hookean springs with ends that can bind and unbind from filaments. Thus, the connectivity of a network and, in turn, its capacity for force propagation varies during simulations. We model molecular motors similarly to crosslinkers except that each bound motor head can walk toward the filament barbed end with a load-dependent speed. The motors can slide filaments, translocate across filaments, and increase network connectivity. We simulate the system using Langevin dynamics in 2D because the *in vitro* experiments we wish to interpret are quasi-two-dimensional, and approximating the system as 2D allows us to treat larger systems for longer times. To account for the fact that a three-dimensional (3D) system would have greater conformational freedom, we do not include steric interactions for our filaments, motors and crosslinkers. This implementation of filaments, motors and crosslinkers, which we detail below, allows for motor-driven filament sliding and filament buckling, as seen in Fig. 2.1D-E. A complete list of model parameters, their values, and references is provided in Table 2.1.

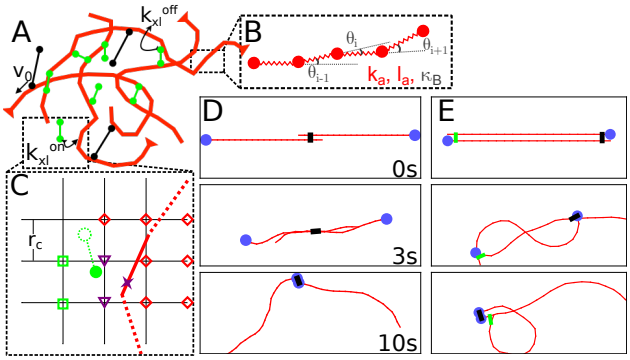

Figure 2.1: Overview of the model. See Section 2.2 for details. (A) Schematic of a configuration of the model. Filaments are red, crosslinkers are green, and motors are black. (B) Expanded view of the actin filament representation: a chain of beads connected by springs with spring constant k_a, rest length l_a, and bending modulus κ_B, as detailed in Section 2.2.1. (C) The process by which a crosslinker finds a filament to bind, as detailed in Section 2.2.2. The solid red link is indexed to the grid points marked with either red or purple stars, and the solid green motor head searches the grid points marked with either green or purple stars for links to bind. The crosslinker head then stochastically binds to the nearest spot on the filament (see Section 2.6.1 and Fig. 2.8A in the Supporting Materials) here marked with a purple $\times$. (D) Successive images of two antiparallel 10 μm filaments (barbed end marked in blue) interacting with one motor at the center. The motor binds to both filaments and slides them past each other. (E) Similar to (D) but with a crosslinker that pins the top filament's pointed end to the bottom filament's barbed end. The motor, bound to both, walks toward the barbed end of the bottom filament and buckles the top filament.

2.2.1 Filaments

The WLC model for actin filaments is implemented as a chain of $N+1$ beads connected by N harmonic springs (links) and $N-1$ angular harmonic springs, as depicted in Fig. 2.1B. The N linear springs penalize stretching and keep the filament's average end-to-end length approximately constant. The $N-1$ angular springs penalize bending and determine the persistence length for a free filament. The filament configurations are governed by the

potential energy U_f:

$$\begin{aligned} U_f &= U_f^{stretch} + U_f^{bend} \\ U_f^{stretch} &= \frac{k_a}{2} \sum_{i=1}^{N} (|\vec{r}_i - \vec{r}_{i-1}| - l_a)^2 \\ U_f^{bend} &= \frac{\kappa_B}{2l_a} \sum_{i=2}^{N} \theta_i^2, \end{aligned} \tag{2.1}$$

where $\vec{r}_i$ is the position of the i^{th} bead on a filament, θ_i is the angle between the i^{th} and $(i-1)^{th}$ links, k_a is the stretching force constant, κ_B is the bending modulus, and l_a is the equilibrium length of a link. In practice, U_f enters the simulation through its Cartesian spatial derivatives (i.e., the forces in Eq. 2.6). In this regard, it is important to note that linearized forms for the bending forces are employed in the literature for filaments whose length is constrained via Lagrange multipliers [126], but we found that it was necessary to use the full nonlinear force to obtain consistent estimates for the persistence length, L_p, for bead-spring-chain filaments (see Section 2.4.1, below). We thus employ the full nonlinear Cartesian forces throughout this work, using the expressions in Appendix C of [1] following the implementation in the LAMMPS Molecular Dynamics Simulator [134].

The bending force constant is derived from the persistence length L_p such that $\kappa_B = L_p k_B T$, where k_B is Boltzmann's constant, and T is the temperature [144]. Experimentally, $L_p = 17$ μm, so $\kappa_B = 0.068$ pNμm^2 for $T = 300$ K [131]. The elasticity per unit length measured for actin filaments with lengths on the order of a micron is 55 ± 15 pN/nm [84, 68]. This implies that a reasonable value for the segment stretching force constant, k_a, would be of this order of magnitude. However, simulating a network of such stiff filaments is computationally infeasible since the maximum timestep of a simulation is inversely proportional to the largest force constant in the simulation [91]. Therefore, we set k_a to a smaller value than estimated from experiment. We note that prevalent extensile behavior, which occurs when filaments interact with two populations of motors with opposite polarities [171], would necessitate using a more realistic k_a. However, because $k_a \gg \kappa_B / l_a^3$ still, upon compres-

sion, filaments prefer bending to stretching, and, as we show, the ability of our model to capture contractile network properties quantitatively is not compromised. Unless otherwise indicated, we use $l_a = 1$ μm, because it is the largest segment length that results in the expected spatial and temporal fluctuations for filaments (see Section 2.4.1, below). We note that very high motor densities can cause filaments to buckle at length scales of ~ 1 μm, and in these cases it would be necessary to use a smaller l_a to capture those effects [14].

2.2.2 Crosslinkers

There are a variety of different actin binding proteins that serve as crosslinkers in the cell cortex, including filamin, fascin, and α-actinin. Crosslinkers connect filaments dynamically and propagate force within the network. Thus, the crosslinkers in our model must be able to attach and detach from filaments with realistic kinetic rules and be compliant when bound. To this end, we model them as Hookean springs with stiffness k_{xl} and rest length l_{xl}. Like actin filaments, the Young's modulus of most crosslinkers is significantly higher than would be reasonable to simulate; therefore, for network simulations without large external forces, we set $k_{xl} = k_a$ so that the bending mode of actin filaments is significantly softer than the stretching mode of crosslinkers. The rest length l_{xl} corresponds to the size of the crosslinker and therefore differs based on the particular actin binding protein one wishes to study.

The statistics of the bound (*on*) and unbound (*off*) states of each crosslinker are determined by a potential energy of the form

$$\begin{aligned} U_{xl} &= U_{xl}^{stretch} + U_{xl}^{bind}(I_1 + I_2) \\ U_{xl}^{stretch} &= \frac{1}{2} k_{xl}(|\vec{r}_1 - \vec{r}_2| - l_{xl})^2 \\ U_{xl}^{bind} &= -k_B T \ln\left(k_{xl}^{on}/k_{xl}^{off}\right) \end{aligned} \tag{2.2}$$

where $\vec{r}_{1(2)}$ is the position of head 1(2), $I_{1(2)}$ is 1 if head 1(2) is bound and 0 otherwise, and k_{xl}^{on} (k_{xl}^{off}) are the rates of binding (unbinding).

Owing to the form of Eq. 2.2 and the Monte Carlo rule for binding (below), it is inefficient for a crosslinker to attempt attachment to every filament link in the simulation box. Rather, we assign a cutoff distance $r_c = \sqrt{k_B T / k_{xl}}$ such that if the distance between a motor and a filament is greater than r_c the probability of attachment is zero. This implementation allows us to use the following neighbor list scheme, illustrated in Fig. 2.1C, to determine crosslinker-filament attachment. A grid of lattice size of at least r_c is drawn on the 2D plane of the simulation, and each filament link is indexed to the smallest rectangle of grid points that completely enclose it. In practice the lattice size is generally larger than r_c due to memory constraints, and is denoted by the model parameter g, the number of grid points per μm in both the x and y directions. Since a crosslinker head cannot bind to a filament link that is farther away than r_c, it suffices for a crosslinker head to only attempt attachment to the nearby filament links indexed to its four nearest grid points.

At each timestep of duration Δt, we enumerate the accessible filament links available to each unbound head. For each link, we determine the nearest point to the head's present position and compute a Metropolis factor for moving to that point: $P_{xl,i}^{off \to on} = \min[1, \exp(-\Delta U_{xl,i}^{stretch} / k_B T)]$ [112]. The head then binds to accessible filament link i with probability $(k_{xl}^{on} \Delta t) P_{xl,i}^{off \to on}$ and stays unbound with probability $1 - \sum_i (k_{xl}^{on} \Delta t) P_{xl,i}^{off \to on}$ [54].

At each timestep, we attempt to move each bound head to a position $\vec{r}_u$ generated by reversing the displacement made upon binding, rotated to account for filament reorientation in the intervening time. This choice of $\vec{r}_u$ allows us to satisfy detailed balance for binding and unbinding by accepting the unbinding transition with probability $(k_{xl}^{off} \Delta t) \min[1, \exp(-\Delta U_{xl}^{stretch} / k_B T)]$, as explained in Section 2.6.1 in the Supporting Materials.

When both crosslinker heads are attached to filaments, the crosslinker is generally stretched or compressed. We propagate the tensile force stored in the crosslinker onto the filaments via the lever rule described in [125, 59]. Specifically, if the tensile force of

a crosslinker head at position $\vec{r}_{xl}$ between filament beads i and $i+1$ is $\vec{F}_{xl}$, then,

$$\begin{aligned} \vec{F}_i &= \vec{F}_{xl}\frac{|\vec{r}_{i+1} - \vec{r}_{xl}|}{|\vec{r}_{i+1} - \vec{r}_i|} \\ \vec{F}_{i+1} &= \vec{F}_{xl} - \vec{F}_i \end{aligned} \tag{2.3}$$

are the forces on beads i and $i+1$ respectively due to the crosslinker.

2.2.3 Motors

In the present work, we focus on the motor protein myosin II. As mentioned above, tens of myosin II proteins aggregate into bipolar assemblies called myosin minifilaments [158]. For both myosin minifilaments, and monomeric myosin, motility assay experiments have shown that, on average, bound myosin heads walk toward the barbed end of actin filaments at speeds in the range $0.2 - 4$ μm/s [86, 168, 62, 41]. Since myosin also functions to increase the local elasticity of networks where it is bound, we model a motor similarly to a crosslinker, in that it behaves like a Hookean spring with two heads, a stiffness k_m, and a rest length l_m. The two heads of this spring do not correspond directly to individual myosin protein heads; rather each of them represents tens of myosin molecules. Experimentally minifilaments have a very high Young's modulus, and it is unlikely that their lengths change noticeably in cytoskeletal networks. As with the passive crosslinkers, we set $k_m = k_a$ so that filament bending is still the softest mode. The rest length was set to the average length of minifilaments, $l_m = 0.5$ μm [128]. Attachment and detachment kinetics, as well as force propagation rules for motors, are the same as for crosslinkers, subscripted with m instead of xl in Eqs. (2.2) and (2.3).

Unlike crosslinkers, motors move towards the barbed end of actin filaments to which they are bound at speeds that decrease with tensile force along the motor. Myosin motors have been observed to stop walking when the force on them exceeds the stall force, $F_s \approx 4$ pN, and most do not step backward [143, 140]. We model this behavior by giving each motor head a positive velocity in the direction of the barbed end of the filament to which it is

attached; this velocity linearly decreases with the motor's tension projected on the filament, i.e.,

$$v(\vec{F}_m) = v_0 \max\left\{1 + \frac{\vec{F}_m \cdot \hat{r}}{F_s}\ ,\ 0\right\}, \tag{2.4}$$

where v_0 is the unloaded motor speed, $F_m = -k(|\vec{r}_1 - \vec{r}_2| - l_m)$ is the spring force on the motor, and $\hat{r}$ is the tangent to the filament at the point where the motor is bound; $\hat{r}$ points toward the pointed end of the filament. In the simulations below, we use a value of $v_0 = 1$ μm/s, which is within range of experimental measurements, but we use a lower value of $F_s = 0.5$ pN, so that motors are not stretched to unphysical lengths as they walk.

If the length of a motor's step is larger than the remaining length of filament, then the myosin moves to the barbed end of the filament. At the barbed end, it has speed $v_0 = 0$, and detachment rate k_m^{end}. We found that $k_m^{end} = 10k_m^{off}$ yielded reasonable results for motility assay and contractile network simulations. In experiments, where each myosin minifilament contains many myosins, a lower barbed end affinity may arise from fewer of the minifilament's myosins remaining attached to the actin filament. In the program, we treat crosslinkers and motors with equivalent objects, but set $v_0 = 0$, and $k_{xl}^{end} = k_{xl}^{off}$ for the crosslinkers.

2.2.4 Dynamics

We use overdamped Langevin dynamics to solve for the motion of filament beads, motors, and crosslinkers. The Langevin equation of motion for a spherical bead of mass m, radius R at position $\vec{r}(t)$ at time t, forced by $\vec{F}(\vec{r}(t))$ in a medium with dynamic viscosity ν is

$$m\ddot{\vec{r}}(t) = \vec{F}(\vec{r}(t)) + \vec{B}(t) - \dot{\vec{r}}(t)/\mu, \tag{2.5}$$

where $\vec{B}(t)$ is a Brownian forcing term that introduces thermal energy, and we use the Stokes relation $\mu = (6\pi R\nu)^{-1}$ in the damping term. The fastest motions in this simulation are the filament bead fluctuations. Taking the bead radius to be 0.5 μm, the maximum speed to be $(2k_BT\mu/\Delta t)^{1/2} = 200$ μm/s and the dynamic viscosity to be $\nu = 0.001$ Pa·s (corresponding

to water), the Reynolds number is very low: $Re \approx 10^{-4}$. Hence, we treat the dynamics as overdamped and set $m = 0$ in Eq. 2.5. Furthermore, in the limit of small Δt, we may write $\dot{\vec{r}}(t) \approx (\vec{r}(t + \Delta t) - \vec{r}(t))/\Delta t$. These two approximations allow us to rewrite Eq. 2.5 as

$$\vec{r}(t + \Delta t) = \vec{r}(t) + \vec{F}(\vec{r}(t))\mu\Delta t + \vec{B}(t)\mu\Delta t. \tag{2.6}$$

For the Brownian term, we use the form of Leimkuhler and Matthews [92]:

$$\vec{B}(t) = \sqrt{\frac{2k_BT}{\mu\Delta t}}\left(\frac{\vec{W}(t) + \vec{W}(t - \Delta t)}{2}\right), \tag{2.7}$$

where $\vec{W}(t)$ is a vector of IID random numbers drawn from the standard normal distribution. This numerical integrator minimizes deviations from canonical averages in harmonic systems; given that all the mechanical forces in our model are harmonic, we expect this choice to yield accurate statistics in the present context as well. The value for Δt in Eq. 2.6 is most strongly dependent on the largest force constant in the simulation, k_a, but also depends on other simulation parameters for both motors and crosslinkers, such as v_0, k^{on}, and k^{off}. Table 2.1 can be used as a rough guide for how high one can set the value of Δt for a given set of input parameters; e.g., for a contracting network with $k_a = 1$ pN/μm, $v_0 = 1$ μm/s, $k_{xl}^{on} = k_m^{on} = k_m^{end} = 1$ s^{-1}, $k_{xl}^{off} = k_m^{off} = 0.1$ s^{-1}, and $k_m^{end} = 10$ s^{-1}, a value of $\Delta t = 2 \times 10^{-5}$ s is just low enough to iteratively solve Eq. 2.6 without accumulating large errors.

2.2.5 Environment

In general we use periodic boundary conditions so as to limit finite-size effects. We implemented square boundaries to model closed systems, as well as Lees-Edwards boundaries for shearing simulations [1]. The dimensions of the simulation box (Table 2.1) were chosen to be five times the contour length of filaments so as to be large enough to avoid artifacts due

to the self-interaction of constituent components.

To ignore steric interactions, the fraction $\phi = N_f \pi (D/2)^2 L/V$ of N_f actin filaments (length L and diameter D) in a volume V must be lower than the critical volume fraction at which steric interactions yield an isotropic to nematic transition, which for long worm-like chains ($D \ll L_p$ and $D \ll L$) is $\phi_c = 5.4D/L$ [138, 130]. For a network of 500 filaments of length $L = 10$ μm and diameter $D = 0.01$ μm, in a $50 \times 50 \times 0.1$ μm^3 plate, this condition is fulfilled, since $\phi = 0.0015 < \phi_c = 0.0054$. While it is difficult to estimate the exact thickness of *in vitro* experimental actomyosin assays due to the complexity of their preparation, we estimate that they are not thinner than 0.1 μm [122]. We have also ignored hydrodynamic interactions between filament beads; the restriction to low packing fraction obviates the need to incorporate anisotropic drag, so we take μ to be equivalent for both transverse and longitudinal motion [9].

2.3 Implementation

The model is implemented as an open source C++ package called Active Filament Network Simulation (AFINES) that is available for download at http://dinner-group.uchicago.edu/downloads.html. Installation instructions are available in the README file in the top directory of the AFINES package, and all information needed to reproduce the materials in this paper are available in the subfolder "versatile_framework_paper". To run a simulation, a user must compile the code into an executable (e.g., with the provided Makefile) and create an output directory. A user can set parameters using command line arguments or a file. For example, if the user has compiled the code into the executable "afines", created the output directory "test", and wants to run a simulation of 500 10 μm actin filaments (with $l_a = 1$ μm), interacting with 0.2 motors/μm^2, and 1 crosslinker/μm^2 (passive motors), in a cell that is 50 μm $\times$ 50 μm, for 100 s, he or she could write the following to the file my_config.cfg

```
xrange=50 # system size in X
yrange=50 # system size in Y

npolymer=500 # number of actin filaments
nmonomer=11 # number of actin beads per filament

a_motor_density=0.2 # motor density
p_motor_density=1 # crosslinker density

tf=100 # duration of simulation
dir=‘‘test’’ # output directory
```

and then run the code using the command

```
afines -c my_config.cfg
```

Alternatively, the user could bypass the configuration file and issue the following command:

```
afines --xrange 50 --yrange 50 --npolymer 500 --nmonomer 11 \
--a_motor_density 0.2 --p_motor_density 1 --tf 100 --dir test
```

In this example, all other parameters were set to their default values (see README file for full list of program parameters). With an executable compiled using g++ with the -O3 optimization flag and run on an Intel E5-2680 node with 2 Gb of memory and a 2.7 GHz processor, this example required less than 1.5 days of wall-clock time. In general, the wall-clock time of the simulation scales linearly with system size (Fig. 2.2).

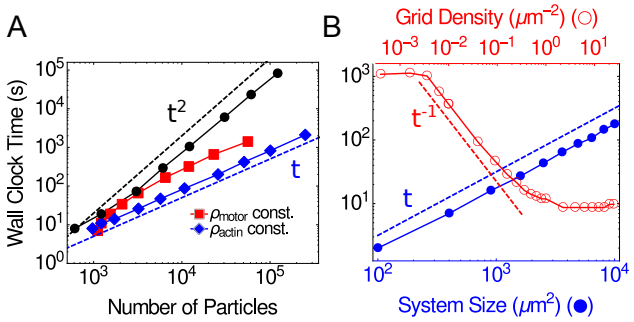

Figure 2.2: Wall clock time for a 10000-step simulation with step size $\Delta t = 0.0001$ s. (A) For a constant system size, run time scales linearly or sublinearly as both filament density (red dots) and motor density (blue dots) are increased independently. If both are increased together (black dots), a quadratic scaling is approached for large numbers of particles. (B) Blue: At constant motor, filament, and grid densities, run time scales linearly with system size (i.e., the area of the simulation box, XY). Red: At constant system size, run time decreases with increasing grid density, g^2, and thereby the number of neighbor-list grid elements, g^2XY, used to calculate motor-filament interactions. All benchmarks are for an Intel E5-2680 node with 2 Gb of memory and a 2.70 GHz processor.

Table 2.1: Parameter Values

Symbol	Description (units) (references)	Simulation			
		L_p	Shear	Motility Assay	Network
	Actin Filaments				
N_f	Number of filaments	20	500	1	500
N_B	Number of beads per filament	$[21, 201]$	11	$[2, 26]$	11
l_a	Link rest length (μm)	$[0.1, 1]$	1	1	1
k_a	Stretching force constant (pN/μm)	$[0.01, 1000]$	1000	1	1
κ_B	Bending modulus (pNμm^2) [131]	$[0.005, 800]$	0.068	0.068	0.068
	Myosin Motors				
ρ_m	Motor density (μm^{-2})	n/a	n/a	$[0, 9]$	0.2
l_m	Rest length (μm) [128]	n/a	n/a	0.5	0.5
k_m	Stiffness (pN/μm)	n/a	n/a	1	1
k_m^{on}	Max attachment rate (s^{-1})	n/a	n/a	$[0.001, 2]$	1
k_m^{off}	Max detachment rate (s^{-1})	n/a	n/a	1	0.1
k_m^{end}	Max detachment rate at barbed end (s^{-1})	n/a	n/a	10	1
v_0	Unloaded speed (μm/s) [86]	n/a	n/a	1	1
F_s	Stall force of myosin (pN) [173]	n/a	n/a	0.5	0.5
	Crosslinkers				
ρ_{xl}	Crosslink density (μm^{-2})	n/a	0.42	n/a	1
l_{xl}	Rest length (Filamin) (μm) [40]	n/a	0.150	n/a	0.150
k_{xl}	Stiffness (pN/μm)	n/a	$[0.1, 1000]$	n/a	1
k_{xl}^{on}	Max attachment rate (s^{-1})	n/a	1	n/a	1
k_{xl}^{off}	Max detachment rate (s^{-1})	n/a	0.1	n/a	0.1
	Environment				
Δt	Dynamics timestep (s)	$[10^{-6}, 10^{-3}]$	10^{-7}	0.00005	0.00002
T_F	Total simulated time (s)	2000	0.5	1000	400
X, Y	Length and width of assay (μm)	n/a	75	50	50
g	Grid density (μm^{-1})	n/a	2	2	2
T	Temperature (K)	300	300	300	300
ν	Dynamic viscosity (Pa·s)	0.001	0.001	0.001	0.001
$\Delta\gamma$	Strain (%) [161]	n/a	0.001	n/a	n/a
t_{relax}	Time between sequential strains (s)	n/a	0.001	n/a	n/a

2.4 Results and Discussion

In this section, we numerically integrate the model to obtain stochastic trajectories and compare their statistics to known analytical results for semiflexible polymers and networks, as well as experimental observations. We also use the model to investigate these systems, including how the viscoelasticity of semiflexible polymer networks depends on crosslinker stiffness, and how the extent of directed motion in actin motility assays depends on filament and motor characteristics. Finally, we use the model to show how one can quantify contractility in a simulated actin network.

2.4.1 Actin filaments exhibit predicted spatial and temporal fluctuations

The persistence length of a semiflexible filament with bending modulus κ_B is expected to be $L_p = \kappa_B/k_BT$. However, when simulating the dynamics, approximations can enter both the evaluation of the forces and the discretized numerical integration of the equations of motion. Because the persistence length is a measure of filament bending fluctuations, and not an input to the simulation, its dependence on simulation parameters must be determined numerically. As discussed in Section 2.2.1 and further below, some care is required to obtain reliable estimates of L_p.

For a two dimensional filament it is possible to show analytically that if a small bend between links i and $i-1$ of an N link chain results in a local change in free energy of $(\kappa_B/2l_a)\theta_i^2$, then

$$\langle \theta^2(l) \rangle = l/L_p \tag{2.8}$$

$$\langle \cos(\theta(l)) \rangle = \exp\left(-l/2L_p\right), \tag{2.9}$$

where $\theta(l) = \theta_j - \theta_i$, $l = l_a(j-i)$ $(2 \leq i < j \leq N)$ [47]. To test our WLC model against these predictions, we let 20 filaments of $L = 20$ μm and $\kappa_B = 0.068$ pNμm^2 fluctuate at $T = 300$ K for $T_f = 2000$ s and measured the resulting filament configurations. The configurations

saved were chosen to be 2 s apart, since the decorrelation time for $\theta(l)$ was at most 1.1 s (see Section 2.6.2 and Fig. 2.9 for details). The first 100 s of each simulation was disregarded as filaments had not yet equilibrated. For each of the 20 filaments, we evaluated $\langle\theta^2(l)\rangle$ and $\langle\cos(\theta(l))\rangle$ for each $l \in 1, 2, \ldots, 19$ μm from its 1900 saved configurations. We show the average for each of these values over all filaments in Fig. 2.3B, along with the expected behavior, given the input κ_B.

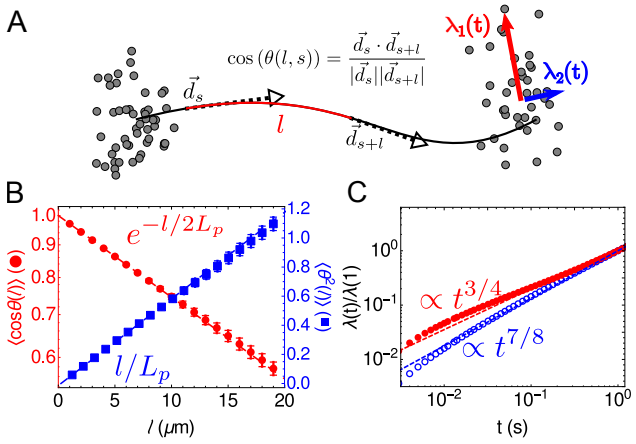

Figure 2.3: Spatial and temporal fluctuations of the bead-spring WLC. (A) Schematic of a filament and the order parameters that characterize its fluctuations. Spatial fluctuations are characterized by the angle between two tangent vectors $\vec{d}_s$ and $\vec{d}_{s+l}$ along the filament as a function of the contour length between them, l. Temporal fluctuations are characterized by the eigenvalues $\lambda_{1,2}(t)$ of the covariance matrix of filament endpoint positions as a function of time. The red arrow indicates the larger moment (λ_1, measuring transverse fluctuations) while the blue arrow indicates the smaller moment (λ_2, measuring longitudinal fluctuations). (B) Decorrelation of tangent vectors (red circles) and fluctuations in angles between links (blue circles) as a function of the arc length between them. For the $N = 20$ filaments analyzed, the blue (red) dots show the mean of $\langle\theta(l)^2\rangle$ ($\langle\cos(\theta(l))\rangle$) and the error bars show their standard errors, $\sigma/\sqrt{N}$, where σ is their standard deviation. Dashed lines show expected behavior for $\kappa_B = 0.068$ pNμm^2. (C) Eigenvalues of covariance matrices for the positions of endpoints of filaments as a function of time. Red dots show $\lambda_1(t)$, which is expected to be proportional to $t^{3/4}$ (red line) while blue dots show $\lambda_2(t)$, which is expected to be proportional to $t^{7/8}$ (blue line). Standard error is smaller than the size of the data points.

As alluded to above, the numerical integration can make the persistence length depend on simulation parameters in nonobvious ways. Consequently, we measured the sensitivity of L_p to independent variations of κ_B, l_a, and k_a. The results shown in Fig. 2.4 are obtained

from using the definition $L_p = 1/(d\langle\theta^2(l)\rangle/dl)$ (i.e., the inverse of the slope of the "blue" line in 2.3B). Fig. 2.4A shows that in the range of $\kappa_B \in [1, 10^5]$ μm$\times k_BT$, L_p determined from the simulation agrees well with the input bending modulus, and can be easily tuned to simulate filaments of varying rigidity. Fig. 2.4B shows that for a wide range of link stiffnesses, L_p is independent of k_a. We also tested the dependence of L_p on the link rest length, l_a. In thermal equilibrium, the variance of the link lengths is $\langle\Delta l_a^2\rangle = k_BT/k_a$. Thus, to keep the fluctuations in the filament's contour length L constant, one should set $k_a \propto l_a^{-2}$. In practice, this scaling is computationally difficult to achieve when $l_a < 0.3$ μm because high k_a requires a very small Δt in Eq. 2.6. We therefore used a less steep variation, $k_a = 1$ pN$/l_a$, and show in Fig. 2.4C that consistent values of L_p are obtained when $l_a \in [0.1, 1]$ μm. We thus see that, there is a range in which L_p is independent of the filament link parameters, k_a and l_a, although high stiffness and low link length both require using a small timestep, and therefore limit the duration of the simulation. In Section 2.6.3 (Fig. 2.11) we measure the persistence length of fibers simulated using Cytosim and obtain similar results.

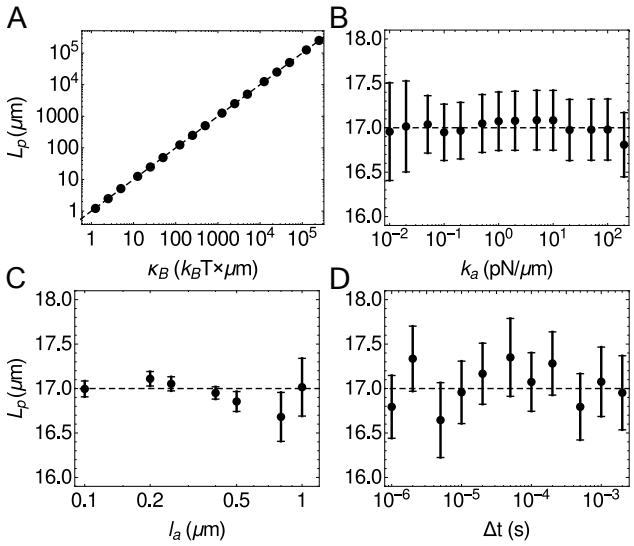

Figure 2.4: Dependence of the persistence length on the parameters for numerically integrated semiflexible filaments. Error bars are $\sigma/\sqrt{N}$, where σ is the standard deviation of the values of L_p obtained from fitting a line to the first 5 data points of $\langle\theta^2(l)\rangle$ for each of the $N = 20$ filaments simulated. The dashed lines show the predicted persistence length, based on the input bending modulus κ_B. The default parameters are $\kappa_B = 17\mu\text{m}\times k_BT$, $k_a = 1$ pN/μm, and $l_a = 1\mu$m. In (A)-(C), $\Delta t \geq 10^{-6}$ s, and the largest Δt that yielded stable integration was used. In (C), $k_a = 1\text{pN}/l_a$.

The statistics of temporal fluctuations are also known for semiflexible filaments. Fluctuations transverse to the filament orientation increase as $\langle dr_\perp^2\rangle \propto t^{3/4}$, while longitudinal fluctuations increase as $\langle dr_{||}^2\rangle \propto t^{7/8}$ [38]. To determine if our simulations agreed with these theoretical scaling relations, we followed the procedure outlined in [38] and generated $N = 100$ initial filament configurations of a 20 μm filament. This length was chosen because it satisfied the constraint provided in [38] for the fluctuations of the two ends of the filament to be uncorrelated at long times (here $t = 1$ s); i.e., $20\ \mu\text{m} > (tk_BT/\nu)^{1/8}\,(\kappa_B/k_BT)^{5/8} = 7\ \mu\text{m}$. For each configuration we ran $M = 1000$ simulations of the filament diffusing freely for 1 s. We denote each of the M positions for each endpoint at each time by $\vec{r}_e(t)$. For each of the clouds of points shown in Fig. 2.3A, we calculated the moments, as the eigenvalues of the covariance matrix with elements $\langle(\vec{r}_e(t)\cdot\hat{i} - \langle\vec{r}_e(t)\cdot\hat{i}\rangle)(\vec{r}_e(t)\cdot\hat{j} - \langle\vec{r}_e(t)\cdot\hat{j}\rangle)\rangle$ for $i, j \in \{x, y\}$. The larger eigenvalue $\lambda_1(t)$ corresponds to the transverse fluctuations (i.e., $\lambda_1(t) \propto t^{3/4}$) while the smaller eigenvalue corresponds to the longitudinal fluctuations ($\lambda_2(t) \propto t^{7/8}$). We

show these results in Fig. 2.3C. Each data point is the average over the $2NM$ eigenvalues for $\lambda_1(t)$ and $\lambda_2(t)$. As evident, the computed scaling relations are in good agreement with theoretically predicted behaviors.

2.4.2 Tunable elastic behavior of crosslinked filament networks

The mechanical properties of crosslinked F-actin have important ramifications for force generation and propagation within a cell. They are generally inferred from rheological measurements of *in vitro* networks [51, 82, 78, 100]. In a typical experiment, actin and crosslinker proteins are mixed to form a crosslinked mesh and then sheared in a rheometer by a prestress, σ_0. The prestressed network then undergoes a sinusoidal differential stress of magnitude $d\sigma \ll \sigma_0$. By measuring the resulting strain, one can calculate the differential elastic modulus $G(\sigma_0) = d\sigma/d\gamma$. Results from such experiments indicate that, in contrast to a purely viscous fluid, crosslinked F-actin networks resist shear, and G increases nonlinearly with stress indicative of shear stiffening.

In experiments using a stiff crosslinker, such as scruin, the dependence of the differential modulus on high prestress is $G \propto \sigma_0^{3/2}$ [51, 100]. Force-extension experiments with semiflexible filaments, in which one directly measures the force F required to extend a filament by a distance l, yield a remarkably similar relationship, $dF/dl \propto F^{3/2}$ [19, 110]. As remarked in [51], this suggests that the shear stiffening is a direct result of the nonlinear force-extension relationship of actin. Rheology studies using more compliant crosslinkers, such as filamin, have found a softer response, $G \propto \sigma_0$, indicating that a significant amount of stress is mediated through the crosslinkers, and not the filaments [78]. These results suggest that the strain stiffening behavior of a crosslinked network can be tuned by varying the crosslinker stiffness.

To test this possibility and benchmark our simulations, we subjected passive networks comprised of filaments and crosslinkers to shear. We initialized each simulation with $N = 500$ randomly oriented filaments of length 15 μm in a square box of area 75 μm $\times$ 75 μm. A

0.150 μm crosslink (corresponding to the length of filamin) was initially placed at each filament intersection. To inhibit network restructuring, the detachment rate of the crosslinkers was set to zero. We performed 24 such simulations, each with a different crosslinker stiffness in the range $0.1 - 1000$ pN/μm.

Simulating shear rheology experiments requires modifying the equations of motion and the boundary conditions to achieve a planar Couette flow. In general, planar Couette flow can be simulated via molecular dynamics using Eq. (4.1) in [37]:

$$\begin{aligned} m\ddot{x} &= F_{int,x} + \dot{\gamma} y \\ m\ddot{y} &= F_{int,y}, \end{aligned} \tag{2.10}$$

where x and y are the Cartesian coordinates of a particle being sheared, $F_{int,x}$, $F_{int,y}$ are the internal forces on those particles and γ is the strain. Simultaneously, the upper and lower boundaries must be sheared by the total strain on the simulation box [1]. Comparing Eq. 2.10 with Eq. 2.5, we substitute $F_{int,x} = F(x(t)) + B_x(t) - \dot{x}(t)/\mu$. In the overdamped limit, $\ddot{x}_i = 0$, so implementing Eq. 2.10 is equivalent to updating filament bead positions via Eq. 2.6, and shifting the horizontal position of a bead (x_i) by

$$x_i \to x_i + \Delta\gamma \left(\frac{y_i}{Y}\right), \tag{2.11}$$

where $\Delta\gamma = \dot{\gamma}\Delta t$ and Y is the simulation cell height. The boundary conditions follow the Lees-Edwards convention [1].

Since moving the particles $\Delta\gamma$ is equivalent to the addition of a significant external force on the system, it is necessary to let the network relax for a specified amount of time t_{relax} after each shear event, before measuring the network's internal energy. The magnitude of t_{relax} depends on $\Delta\gamma$, which in turn depends on the chosen discretization of the strain and the timestep Δt. As shown in Section 2.6.2 and Fig. 2.10, we found that $\Delta\gamma = 0.001$, $\Delta t = 10^{-7}$ s, and $t_{relax} = 0.001$ s yielded a stable planar Couette flow, with high enough

strains to observe strain stiffening. This protocol was performed for $T_f = 0.5$ s yielding a total strain of $\gamma = \Delta\gamma T_f / t_{relax} = 0.5$.

We measured the elastic behavior of the network for each crosslinker stiffness by calculating w, the strain energy density at each timestep:

$$w(t) = \frac{1}{XY}\left(\sum_f U_f + \sum_{xl} U_{xl}\right), \tag{2.12}$$

where U_f is the mechanical energy of individual filaments (Eq. 2.1) and U_{xl} is the mechanical energy of each crosslink (Eq. 2.2). By averaging over windows of size t_{relax}, we determine $w(\gamma)$. Fig. 2.5 shows the results of these calculations for various values of k_{xl}. For extremely low k_{xl}, the strain energy scaled linearly with strain, $w \propto \gamma$, indicating that the network showed no resistance to shear: $G = d^2w/d\gamma^2 = 0$. For high k_{xl}, we observe a neo-Hookean strain stiffening behavior, $w \propto \gamma^4$ [155]. Thus, we can tune the material properties of crosslinked semiflexible networks from being liquid-like, with $w \propto \gamma$, through the Hookean elastic regime of $w \propto \gamma^2$ up to the strain stiffening regimes of $w \propto \gamma^3$ and $w \propto \gamma^{3.5}$, as previously reported in experiments [51, 78]. We show in Section 2.6.4 and Fig. 2.12 that the monotonic increase in scaling for low k_{xl} corresponds to a regime where the strain energy is mostly stored in the crosslinkers, while the plateau at high k_{xl} corresponds to a regime where the strain energy is mostly stored in filaments.

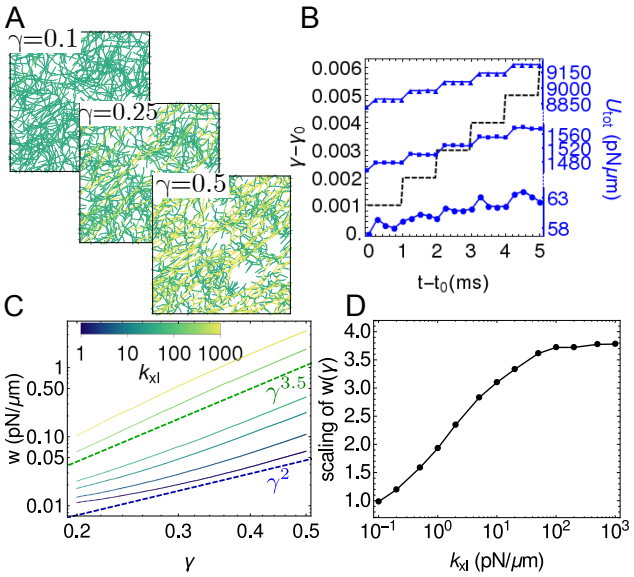

Figure 2.5: Tunable elasticity of crosslinked networks. (A) Snapshots of a strained network (k_a = 1000 pN/μm, k_{xl} = 20pN/μm) at $\gamma = 0.1$, $\gamma = 0.25$, and $\gamma = 0.5$. Color indicates stretching energy on each link, with green being the lowest and yellow being the highest. For all snapshots, $t = \gamma \times 1$ s. (B) The potential energy of the network as a function of time shown at different strains $\gamma_0 = 0.1$ (circles), $\gamma_0 = 0.25$ (squares), and $\gamma_0 = 0.4$ (triangles), where $t_0 = \gamma_0 \times 1$ s. Black dashed line shows the strain protocol. (C) Strain energy density ($w = U/XY$) for various values of crosslinker stiffness k_{xl}. Blue dashed line indicates expected behavior for a linearly elastic solid ($w \propto \gamma^2$) and green dashed line indicates strain stiffening behavior of $w \propto \gamma^{3.5}$ as expected for semiflexible polymer networks [51, 100]. (D) The power-law exponent of $w(\gamma)$ as a function of crosslinker stiffness, evaluated by least squares fitting $\ln(w)$ as a function of $\ln(\gamma)$.

2.4.3 Ensembles of motors interacting with individual filaments simulate actin motility assays

While the attachment, detachment and speed of an individual myosin motor is a model input (described in Section 2.2.2 and Section 2.2.3, above), the collective action of many motors on a filament is an output that can be compared with actin motility assays [140, 176]. In the canonical motility assay experiments, a layer of myosin is attached to a glass coverslip, and actin filaments are distributed on top of the layer of myosin motors. The fixed motors translocate the actin filaments. The speed of an actin filament has been reported to depend nonlinearly on the concentration of myosin and the concentration of ATP in the sample [62,

168]. Thus, by allowing the filaments to interact with more motors, one can monotonically increase the filament speed to a constant value.

To explore the dynamics of such an assay, we randomly distributed motors on a 50 μm $\times$50 μm periodic simulation cell and tethered one head of each motor to its initial position. These model motors represent myosin minifilaments with dozens of heads, and therefore have a high default duty ratio ($r_D = 0.5$), and rest length $l_m = 0.5$ μm [128, 72]. Filaments were then introduced in the simulation cell and allowed to interact with the free motor heads. The strength of motor-filament interactions was manipulated in three ways: by varying the motor concentration ρ_m, the filament contour length L, and the duty ratio $r_D = k_m^{on}/(k_m^{on} + k_m^{off})$. While L and r_D are difficult to modulate experimentally in a well-controlled fashion, as they require the addition of other actin-binding proteins to the assay, they are predicted to impact the dynamics of actin by varying the number of myosin heads bound to an actin filament at any one time [62]. Since they are both simple functions of the model's parameters, we were able to test this hypothesis directly. We plot our simulation results in Fig. 2.6 as functions of the dimensionless control parameter $\mathcal{M} = \rho_m l_m L r_D$ (where $\rho_m l_m$ is the linear motor density), which represents the average number of bound motor heads per filament.

Our findings are qualitatively similar to the previously reported experimental results and expand on them by collapsing the trends observed while varying ρ_m, L, and r_D into a single effective parameter. At low $\mathcal{M}$, i.e., low motor density, filament length, or duty ratio, Fig. 2.6B shows that transverse motion dominates over longitudinal motion as the filament is not propelled by motors faster than diffusion, and transverse filament fluctuations are larger than longitudinal fluctuations (consistent with Fig. 2.3C). However, as $\mathcal{M}$ increases, longitudinal motion dominates. Consistent with experimental results [86, 62], the longitudinal speed of the filament plateaus at $v_{||} \approx 1$ μm/s, which is the input unloaded speed of a single motor. In Fig. 2.6C, we plot the mean squared displacement (MSD) of the filament, $\langle \Delta r^2 \rangle = \langle |\vec{r}(t + \delta t) - \vec{r}(t)|^2 \rangle$ with angle brackets indicating an average over time t. We show that low $\mathcal{M}$ yields diffusive behavior with $\langle \Delta r^2 \rangle \propto \delta t$, and high $\mathcal{M}$ yields ballistic motion

with $\langle \Delta r^2 \rangle \propto \delta t^2$. We obtain similar results for motility assay behavior with a corresponding Cytosim simulation, as shown in Section 2.6.5 (Fig. 2.13).

An interesting outcome of these simulations is how the direction of a filament changes over time for varying $\mathcal{M}$. Specifically, we calculate the directional autocorrelation of a filament and, in turn, the persistence length of the path of the filament by applying Eq. 2.9 to the center of mass of the filament at frames separated by $\Delta t = 1$ s (Fig. 2.6D). Scaling arguments suggest that the path's persistence length depends strongly on motor density, duty ratio, and filament length [32]. In the limit of high $\mathcal{M}$, the distance between motors that are bound to a filament is sufficiently short that the filament does not diffuse transversely; however, fluctuations in the filament configuration still allow directional decorrelation, and consequently the path's persistence length is L_p. At low $\mathcal{M}$, the distance between bound motors is sufficiently large that rotational diffusion causes the filament's path to be completely decorrelated, such that the path's persistence length approaches 0. In Fig. 2.6D, we show that the simulation agrees with theoretically predicted scaling laws at low and high $\mathcal{M}$ [32]. Our results delineate the values of $\mathcal{M}$ at which there are crossovers between the predicted limiting regimes.

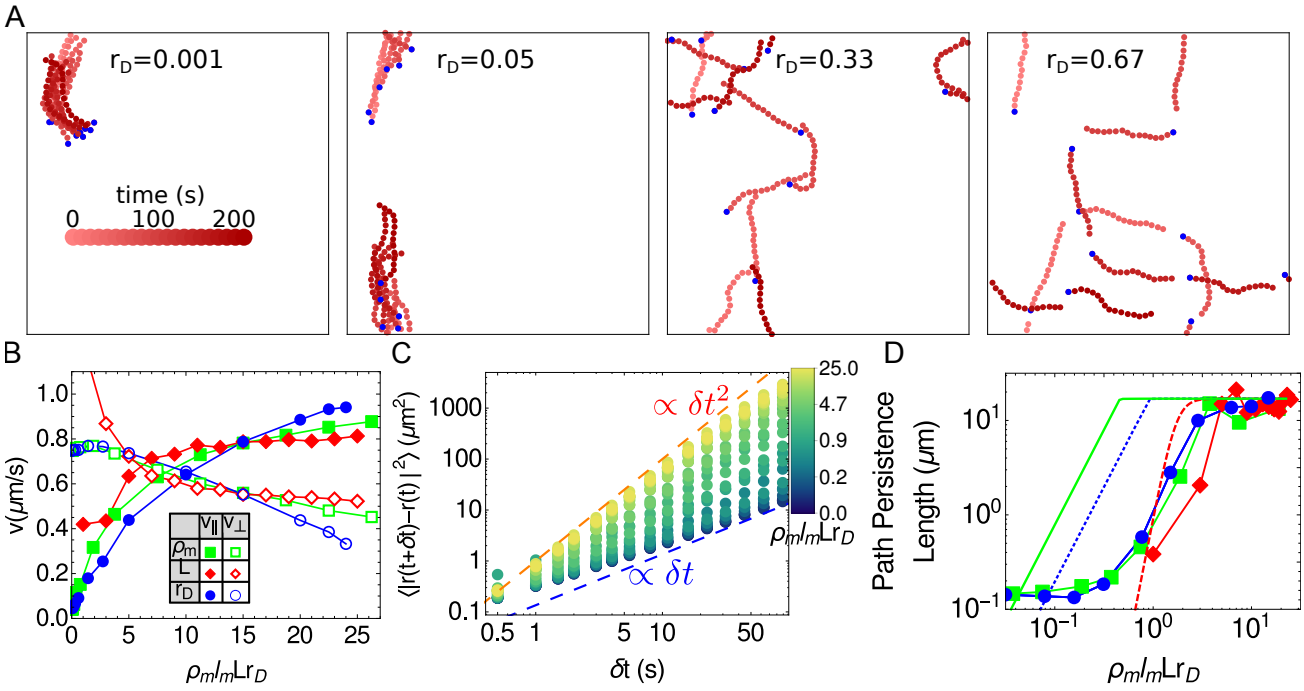

Figure 2.6: Nonlinear dependence of filament motility on motor-filament interaction probability. (A) Trajectory of a filament for $\rho_m = 4\ \mu\text{m}^{-2}$ and $L = 15\ \mu$m as a function of time for different values of the duty ratio, r_D. Depth of color indicates time of the snapshot, as indicated by the scale. Blue dot marks the barbed end. (B) Filament speed decomposed into longitudinal (filled circles) and transverse (empty squares) components as a function of the dimensionless parameter $\mathcal{M} = \rho_m l_m L r_D$, by independently varying ρ (green), L (red), and r_D (blue). The default parameters were $\rho = 4\ \mu\text{m}^{-2}$, $L = 15\ \mu$m, and $r_D = 0.5$. (C) Mean squared displacement for various values of $\mathcal{M}$. Blue dashed line shows diffusive behavior and orange dashed line shows ballistic behavior. (D) Path persistence length for simulations described in (B), evaluated via Eq. 2.9 over 5 replicates. Dashed lines are theoretical predictions for these values using equations (1)-(6) in [32].

2.4.4 Molecular motors cause flexible, crosslinked networks to contract

When motors, crosslinkers, and filaments are combined into a single assembly, simulated networks contract. The structure and dynamics of these networks exhibits a rich dependence on motor and crosslinker densities, binding/unbinding kinetics, and stiffness parameters. Here, we show one illustrative example to demonstrate that our model reproduces actomyosin contractility for a reasonable choice of parameters (Fig. 2.7A). The network is initialized by randomly orienting 500 filaments, each 10 μm long, within a 50 μm $\times$ 50 μm simulation

cell. We distribute 0.15 μm long crosslinkers throughout the simulation cell at a density of 1 μm^{-2}, and 0.5 μm long motor oligomers at a density of 0.2 μm^{-2}. As the simulation evolves, the actin density becomes more heterogenous as motors condense actin filaments into dense disordered aggregates. This density heterogeneity can be quantified by the radial distribution function of actin filaments, $g(r) = P(r)/(2\pi r \delta r \rho_f)$, where $P(r)$ is the probability that two filaments are separated by a distance r, $\delta r = 0.1$ μm is the spatial bin size, and ρ_f is the filament density. As shown by Fig. 2.7B, $g(r) \approx 1$ at $t = 0$ for all r as the actin filaments are homogeneously distributed. However, over time it becomes more peaked at lower separation distances between filaments, indicating filament aggregation.

To measure the contractile activity of the network, we evaluate the divergence of its velocity field. This is done by calculating the velocity of each of the actin beads, followed by a grid-based interpolation of a velocity vector field from those values (black arrows in Fig. 2.7C; interpolation scheme described in Section 2.6.6). One can then evaluate the divergence $\nabla \cdot \vec{v}$ of the interpolated field at every spatial location (color of Fig. 2.7C). Since there is no flux of actin into the simulation box, the total divergence of the flow field is zero at all times (i.e., $\int (\nabla \cdot \vec{v})\, dA = 0$). Therefore, we weight the divergence of each patch of the network by its local density and measure $\int \rho_a \langle \nabla \cdot \vec{v} \rangle dA$ where $\rho_a = n_a/dA$ is the number density of actin beads and $\langle \nabla \cdot \vec{v} \rangle$ is the average actin divergence in the patch of size dA. As shown in Section 2.6.6, this order parameter shows consistent behavior for small patches ($dA \leq (10\ \mu\text{m})^2$) and a range of step sizes ($h \leq 20$ s) for the velocity calculation (Eq. 2.19). We also measure the average filament strain $\overline{\Delta s}$, in the network, where

$$\Delta s = \left(1 - \frac{|\vec{r}_N - \vec{r}_0|}{\sum_{i=1}^{N} |\vec{r}_i - \vec{r}_{i-1}|} \right), \tag{2.13}$$

$\vec{r}_i$ is the position of the i^{th} bead on an $(N+1)$-bead filament, and the bar denotes an average over all filaments. Fig. 2.7D shows the results of measuring network divergence and filament strain from 20 simulations with the same parameter choices as in Fig. 2.7A, but with

different random number seeds. The divergence measurement (blue) shows that the network is contractile, since the density weighted divergence is negative, and its shape echoes the experimental results in [120], where the magnitude of contractility decreases to a minimum before plateauing. The filament strain measurement (red) shows that as the network is contracting, individual filaments are buckling. This supports the notion that the mechanism behind contractility in disordered actomyosin networks is actin filament buckling [95, 123]. We note that, while the parameterization of motors that we used for the motility assays yields contractile networks (Fig. 2.14), using a lower value of k_m^{off} resulted in kinetics closer to those observed in experiment [120]. This improvement with higher motor affinity may reflect differences in the number of participating motor heads in contractility and motility assays.

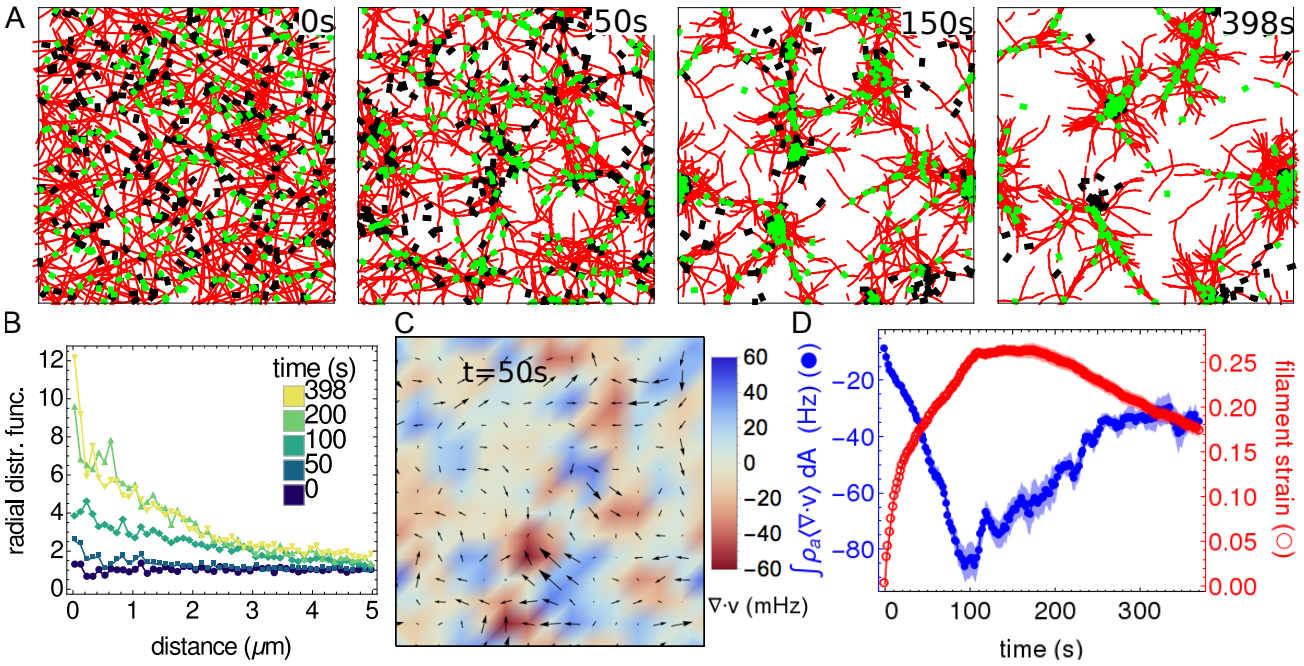

Figure 2.7: Contractility of a crosslinked filament network driven by motors. Filaments are red, motors are black, and crosslinkers are green. (A) Network configurations at $t = 0$, 50, 150, and 398 s. While all filaments are shown, only 10% of crosslinkers and 50% of motors are shown for clarity. (B) Radial distribution function at frames corresponding to (A). (C) Quantification of the motion at $t = 50$ s. Arrows (directions and sizes) indicate the filament-bead velocity field generated by the procedure in Section 2.6.6. Colors map the corresponding divergence. (D) The density weighted divergence (blue; $dA = (1\ \mu\text{m})^2$) and average filament strain (red) of actin filaments for contractile networks. Dark lines for both curves shows the mean $\mu(t)$ of these results at each time t over $N = 20$ simulations. Shaded areas show the standard error of the mean $\mu(t) \pm \sigma(t)/\sqrt{N}$ where $\sigma(t)$ is the standard deviation.

2.5 Conclusion

In this paper, we have introduced an agent-based modeling framework that can accurately and efficiently simulate active networks of filaments, motors, and crosslinkers to aid in the interpretation and design of experiments on cytoskeletal materials and synthetic analogs. While our focus here has been on selecting parameters that are representative of the actin cytoskeleton, we expect that this framework can be adapted to treating other active polymer assemblies as well, such as microtubule-kinesin-dynein networks. We demonstrated that the model gives rise to both qualitative and quantitative trends for structure and dynamics

observed in experiments and provides experimentally testable predictions. Specifically, we reproduced the experimentally observed and theoretically described fluctuation statistics of actin filaments. We also captured strain stiffening scalings and predicted how network elasticity can potentially be tuned via crosslinker stiffness. We modeled sliding filament assays and determined specific system parameters that lead to the crossover from transversely diffusive to longitudinally processive motion first predicted in [32]. In separate studies, we use our model to explore the phase space of various network structures and the dynamics that lead to them [159].

While our model captures many experimental observations, we simplified certain features to limit both computational cost and model complexity. First, the structure of myosin minifilaments is significantly more complex than a two-headed spring. As mentioned, minifilaments have dozens of heads, which allows them to attach to more than two filaments simultaneously, significantly increasing local network elasticity [101] and enabling more complex motor dynamics [151]. Second, filaments do not polymerize, depolymerize, or sever in the simulations; it is clear, however, that recycling of actin monomers, actin treadmilling and, to a lesser degree, filament severing play important roles in contraction and shape formation [182, 123]. Third, our simulations are restricted to 2D, without steric or hydrodynamic interactions. This can play a role in motility assays, for example, where at high actin densities, actin filaments organize into polar patterns with characteristic autocorrelation times [147]. It would be valuable to make the model a progressively more faithful representation of reality in the future to better understand how each of these choices impacts the behavior of the model and in turn the implications for the associated physics.

2.6 Supplementary Information

2.6.1 Calculation of crosslinker head position during binding and unbinding

In this section, we describe how we update the binding state ($I_{1(2)}$ in Eq. 2.2) and position ($\vec{r}_{1(2)}$) of a crosslinker head. The binding states and positions of the two heads of a crosslinker are coupled only through the potential energy (Eq. 2.2).

We first discuss binding. An unbound crosslinker head with position $\vec{r}_u$ can attempt to bind to the closest point on each nearby filament link. Let $\vec{l_i} = \vec{r}_i - \vec{r}_{i-1}$, where $\vec{r}_i$ is the position of the i^{th} bead on the filament to which the link belongs. Then, we propose a bound state with binding point

$$\vec{r}_b = \begin{cases} \vec{r}_{i-1} & |\vec{l_i}| = 0 \text{ or } p \leq 0 \\ \vec{r}_i & p \geq 1 \\ \vec{r}_{i-1} + p\vec{l_i} & \text{otherwise} \end{cases} \tag{2.14}$$

where $p = (\vec{r}_u - \vec{r}_i) \cdot \vec{l}_i$. Eq. 2.14 can be interpreted easily in a reference frame in which $\vec{l_i}$ is oriented vertically (Fig. 2.8A): if $\vec{r}_u$ is below the link, $\vec{r}_b = \vec{r}_{i-1}$; if it is above the filament then $\vec{r}_b = \vec{r}_i$; otherwise $\vec{r}_b$ is the intersection of $\vec{l_i}$ with the line perpendicular to $\vec{l_i}$ that passes through $\vec{r}_u$. If $|\vec{r}_b - \vec{r}_u| < r_c$, the changes in binding state and position are accepted with probability $(k_{xl}^{on}\Delta t)P_{xl,i}^{off\to on}$ (see main text, Section 2.2.2).

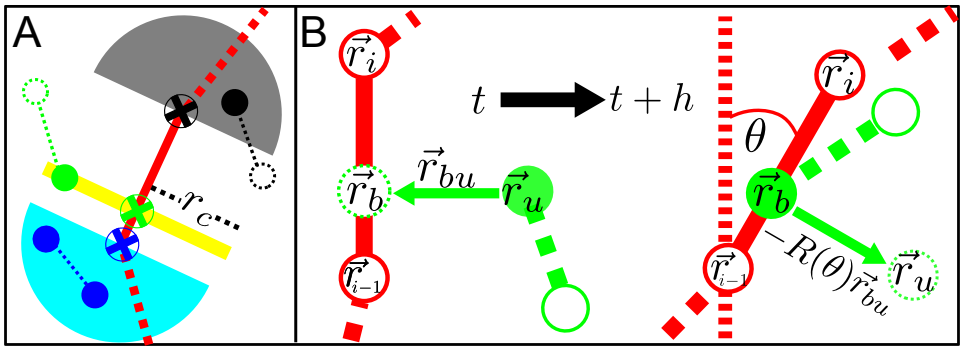

Figure 2.8: Position of crosslinker head upon binding or unbinding. (A) Any crosslinker head in the aqua, yellow, and gray areas (such as the filled blue, green, and black circles) can bind to the blue, green, and black binding points (circles with crosses), respectively. (B) The process by which a crosslinker generates an unbinding point (r_u) at time $t+h$ using its original displacement at time t when it snapped to the binding point r_b.

For unbinding, we do the following. At the time of binding (t), we record the displacement vector, $\vec{r}_{bu} = \vec{r}_b(t) - \vec{r}_u(t)$, and the vector connecting the ends of the filament link, $\vec{l}_i(t) = \vec{r}_i(t) - \vec{r}_{i-1}(t)$. At the time that we attempt unbinding ($t+h$), we determine the angle of rotation of the filament link:

$$\theta = \arccos\left(\frac{\vec{l}_i(t)\cdot\vec{l}_i(t+h)}{|\vec{l}_i(t)||\vec{l}_i(t+h)|}\right). \tag{2.15}$$

Then, the position to which the crosslinker head tries to jump is

$$\vec{r}_u(t+h) = \vec{r}_b(t+h) - \begin{pmatrix} \cos(\theta) & -\sin(\theta) \\ \sin(\theta) & \cos(\theta) \end{pmatrix} \vec{r}_{bu}(t) \tag{2.16}$$

as shown in Fig. 2.8B. This jump is accepted with probability $(k_{xl}^{off}\Delta t)P_{xl,i}^{on\rightarrow off}$. The motivation for this scheme is that it ensures that a head that jumps onto (off) a filament link returns to its original position if it unbinds (rebinds) immediately. Detailed balanced consistent with Eq. 2.2 can thus be satisfied through the acceptance probabilities $(k_{xl}^{on}\Delta t)P_{xl,i}^{off\rightarrow on}$ and $(k_{xl}^{off}\Delta t)P_{xl,i}^{on\rightarrow off}$.

2.6.2 Relaxation times scales

In this section, we present data on filament and network time scales that inform our choices of sampling frequencies.

Decorrelation of filament angles

The evaluations of persistence length in Section 2.4.1 in the main text average over independent configurations of filaments. To determine the amount of time between independent configurations in a trajectory of a single filament, we evaluated the integrated autocorrelation time of the angles θ_i for $i \in [2 \dots 20]$ between links along a 21 bead filament. Fig. 2.9A shows the autocorrelation

$$R(\theta, s) = \frac{\langle \theta(t)\theta(t+s) \rangle - \langle \theta(t) \rangle^2}{\langle \theta(t)^2 \rangle - \langle \theta(t) \rangle^2} \tag{2.17}$$

where s is the time between realizations and the angle brackets represent an average over all 19 angles and all 1900 saved configurations. Fig. 2.9B shows the integrated autocorrelation time τ as a function of the simulation cutoff time t_{final}, where

$$\tau(\theta) = \int_0^{t_{final}} R(\theta, s) ds. \tag{2.18}$$

For all choices of t_{final}, $\tau < 2$ s and therefore configurations that are separated by at least 2 s should be independent realizations with respect to angles between subsequent filament links.

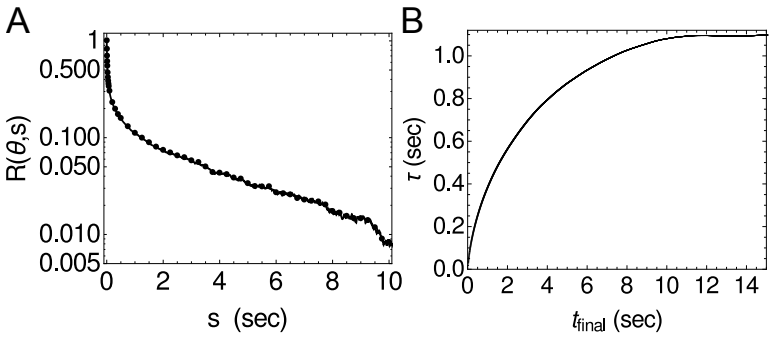

Figure 2.9: Estimation of the characteristic decorrelation time for persistence length measurements. (A) Decorrelation of angles between filament links for a 21 bead filament with $k_a = 1$ pN/μm, $l_a = 1$ μm, and $\kappa_B = 0.068$ pNμm^2. (B) Measurement of the integrated autocorrelation time τ for different values of the cutoff time t_{final}.

Shear relaxation times

One extra parameter that must be set for shear simulations is the relaxation time (t_{relax})—i.e., the minimum time between strain steps for responses to be history independent. We probed this question computationally by determining if the parameter of interest (total potential energy of filaments and crosslinkers) varied significantly for different periods of relaxation between steps of $\Delta\gamma = 0.001$. Fig. 2.10 shows that while very small t_{relax} values do yield higher energies at equivalent strains, as t_{relax} is increased, the curves collapse for identical strains. In the shear simulations in the main text (Section 2.4.2), $t_{relax} = 1$ ms (yellow curve).

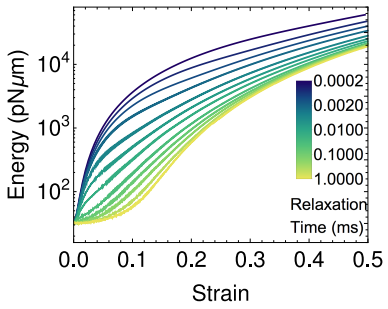

Figure 2.10: Total potential energy as a function of strain for various relaxation times. Simulation parameters, are otherwise identical to the shear simulations in the main text.

2.6.3 Comparison with CytoSim

Cyotsim is a freely available C++ software package developed to simulate active polymer networks and described in [126]. While AFINES shares many of the same features, for clarity we enumerate the technical differences.

- **The filament model.** AFINES uses a bead spring chain and CytoSim uses a chain constrained via Lagrange multipliers.

- **Attachment of motors and crosslinkers.** CytoSim uses a continuous-time Monte Carlo procedure (the Gillespie algorithm [54]) to calculate when a motor should attempt attachment to a filament, while AFINES attempts with the probability computed for each discrete timestep of fixed duration. In Cytosim, the attachment of a motor to a filament is not dependent on the distance from the filament, other than that it must be below a threshold, whereas in AFINES, a closer motor has a higher probability of attachment, due to detailed balance considerations.

- **Detachment of motors and crosslinkers.** CytoSim has a force dependent detachment of crosslinkers. This was not a necessary detail to reproduce the benchmarks shown in the results section, and detailed balance would require altering the motor and crosslinker dynamics, so we have not included it in the present version. We plan in the future to understand how this detail effects cytoskeletal networks in general and add it as an option to AFINES.

- **Capabilities present in one and not the other.** AFINES implements network shearing. CytoSim implements filament polymerization and depolymerization, microtubule asters, and spherical geometries.

To compare the two packages, we have used CytoSim to run the benchmarks associated with filament fluctuations (Fig. 2.11) and motility assays (Fig. 2.13, below). For the filament fluctuation benchmarks, shown in Fig. 2.11, we find that while CytoSim is able to yield nearly

the correct persistence length of filaments, at long segment lengths it performs worse than AFINES, perhaps because it uses linearized versions of the angle forces [126].

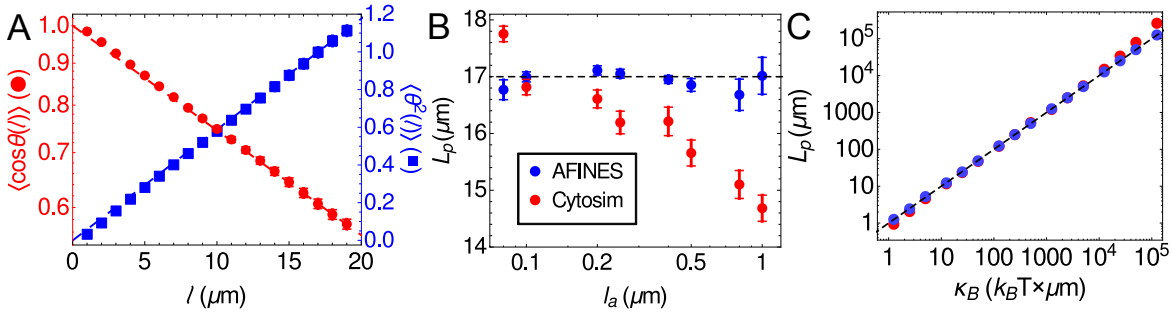

Figure 2.11: Measurements of persistence length for CytoSim filaments (red) compared with the same measurements for AFINES (blue). (A) Cosine correlation function and $\Delta\theta^2$ correlation function for 20 CytoSim fibers with $L_p = 17$ μm fluctuating for 2000 seconds. See Section 4.1 of the main text for details. (B) Measurement of L_p as function of segment length, l_a, using the fit to the first 5 data points of $\langle\Delta\theta^2\rangle$ in (A). (C) Measurement of L_p as a function of input bending modulus for CytoSim and AFiNes. Colors are the same as panel B.

2.6.4 Parsing the energy in sheared networks

To further examine the source of the energy scalings shown in Fig. 2.5D, we measure the fraction of the total energy density w from each of its sources in the network, the stretching energy of filaments, the stretching energy of crosslinkers, and the bending energy of filaments, as shown in Fig. 2.12. In general, we find that shearing the network stretches and bends actin filaments, and also stretches crosslinkers, as in Fig. 2.12A-C. Fig. 2.12B-C show that, as crosslinkers become more stiff, more of the energy from the strain is concentrated on the filaments. Fig. 2.12A shows that for crosslinkers, the trend is not monotonic. When $k_{xl} < 100$ pN/μm, increasing crosslinker stiffness results in more energy in the crosslinkers, and in this regime, the scaling of $w(\gamma)$ increases monotonically. However, for $k_{xl} \geq 100$ pN/μm, the trend reverses, and the strain energy density concentrates on the filaments more than the crosslinkers, as seen in Fig. 2.12D-E. In this regime, the scaling of $w(\gamma)$ plateaus near the value 3.5, reflecting the prediction for the differential shear modulus in a strain controlled

rheology experiment, $G = d^2w/d\gamma^2 \propto \gamma^{3/2}$ [51].

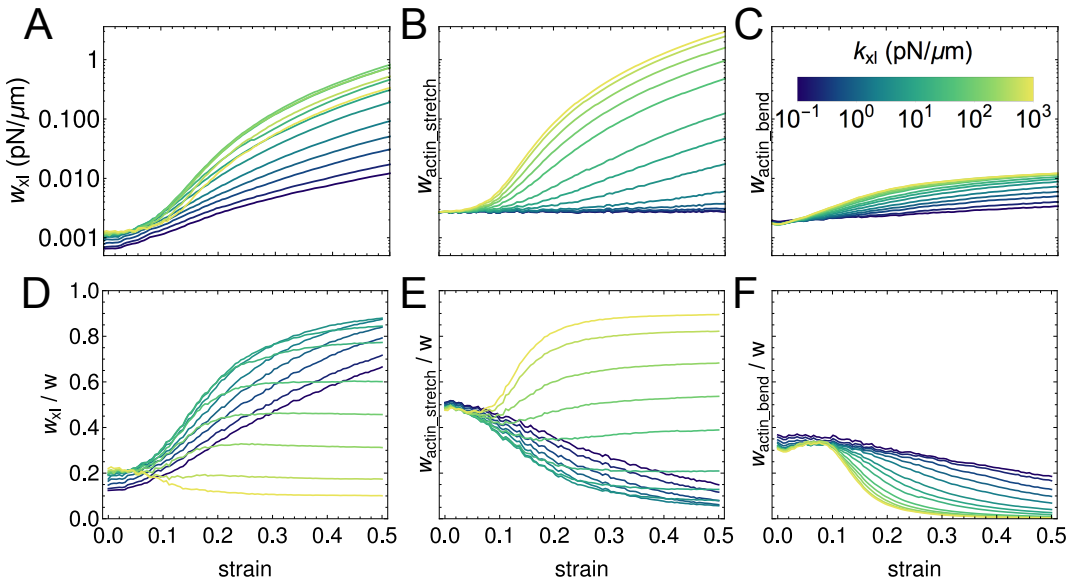

Figure 2.12: Absolute (A-C) and relative (D-F) energy contributions from crosslinkers stretching (A, D), filaments stretching (B, E), and filaments bending (C, F) for the sheared network discussed in Section 2.4.2.

2.6.5 Comparison with Cytosim for motility assays

We also used Cytosim to simulate the motility assays described in the main text (Section 2.4.3). The results, shown in Fig. 2.13, are generally congruent with the results from AFINES in Fig. 2.6. We find that increasing motor density, filament length, and duty ratio increase longitudinal motion and decrease transverse motion of the filament (Fig. 2.13B), and makes the filament move more ballistically (Fig. 2.13C). Furthermore, the path persistence length plots (Fig. 2.13D) are nearly identical to the measurements obtained using AFiNES. Thus, it is reassuring that the two models agree to this extent despite the differences in filament and binding implementations.

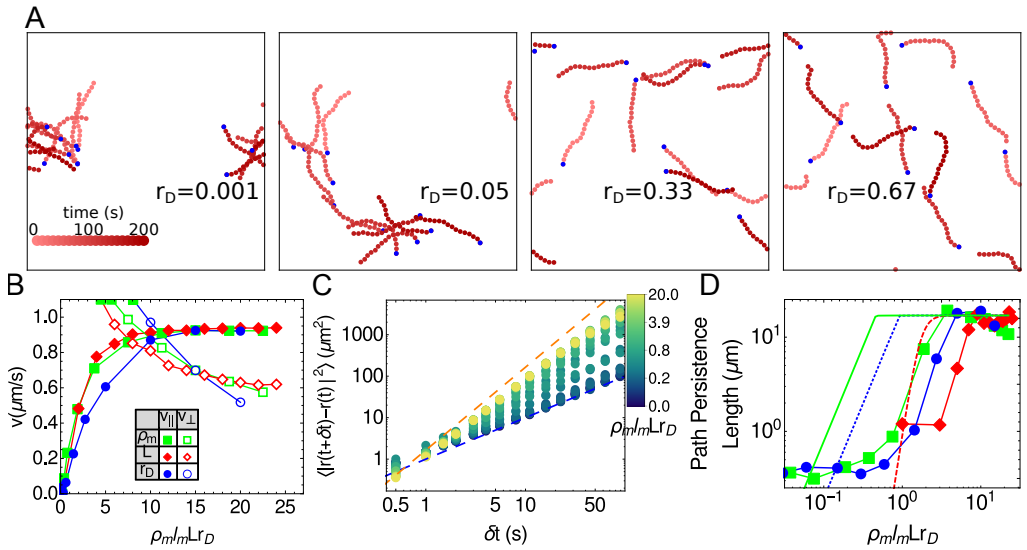

Figure 2.13: Motility measurements at varying motor density, filament length, and duty ratio generated using CytoSim. For a detailed description of this calculation see main text, Section 2.4.3.

2.6.6 Procedure for quantifying contractility

An actin assay can be considered contractile if it has regions to which most of the actin aggregates. In an experiment with a limited field of view, the net flux of actin into the field of view is positive when the system is contractile. This flux corresponds mathematically to a negative value for the integral of the divergence of the velocity field over the area [123, 120]. However, in our simulations, all particles' positions are known and there is no flux of material into or out of the simulation region owing to the periodic boundary condition. Thus the total divergence obtained by integrating over the simulation box must be zero. Nevertheless, we can still compute the density-weighted divergence to quantify contractility, as we now describe.

To ensure that the divergence is well-defined at all points, we first interpolate a continuous velocity field. When the data are experimental images, the velocity field is determined using Particle Image Velocimetry (PIV). Here, we take a similar approach, with the advantage that positions of actin beads are a direct output of the simulation, analogous to tracer particles in experiments. To this end, for each filament bead i with position $\vec{r}_i(t)$ at time t, we calculate

the velocity by forward finite difference:

$$\vec{v}_i(\vec{r}_i, t) = \frac{\vec{r}_i(t+h) - \vec{r}_i(t)}{h}, \tag{2.19}$$

where h is a suitable amount of time to characterize motion. We calculate the average velocity of each (5 μm)^2 bin. Similarly to PIV, we lower the noise further by setting a threshold, and only consider bins with at least n actin beads. We then interpolate the bin values with Gaussian radial basis functions (RBFs):

$$\vec{v}(\vec{r}) = \sum_{k=1}^{M} \vec{w}_k e^{-(|\vec{r}-\vec{r}_k|/\epsilon)^2} \tag{2.20}$$

where M is the number of bins with at least n actin beads, ϵ is a constant related to the width of the Gaussian RBFs, and $\vec{w}_k$ are their weights. The optimal value for ϵ is generally close to the value of the average distance between RBFs [67]; we found $\epsilon = 5$ μm and a threshold of $n = 10$ yielded a robust interpolation across many different actin structures. We use the scipy.interpolate.Rbf Python package to determine the weights [67]. We calculate the divergence of the resulting field $dv_x(\vec{r})/dx + dv_y(\vec{r})/dy$ by using finite difference approximations for the derivatives of Eq. 2.20. Examples of this velocity field and the local divergence are shown in Fig. 2.7C and Fig. 2.14C.

As noted above, given $\nabla \cdot \vec{v}$, we quantify the contractility by the density weighted divergence, $\int \rho_a \langle \nabla \cdot \vec{v} \rangle dA$. In Fig. 2.14E we show an example where the density weighting has the effect of significantly increasing the magnitude of the areas with negative divergence. To understand how the contractility varies with length scale, we replace the integral with the sum over square regions

$$\sum_k \rho_a(\vec{r}_k) \langle \nabla \cdot \vec{v} \rangle_k dA \tag{2.21}$$

and vary the size of the regions, $dA = dxdy$ (Fig. 2.14F). For the maximum size $dA =$ (50 μm)^2 (yellow curve), the density weighted divergence fluctuates around 0 as expected

from the zero actin flux. However for region sizes $dA \leq (10\ \mu\text{m})^2$, the values are consistently negative, indicating contractility; the curves decrease to a minimum before plateauing closer to 0, as seen in experiment [120]. We also show, in Fig. 2.14G, that the trend of this order parameter is independent of the time scale h used to calculate the velocity in Eq. 2.19.

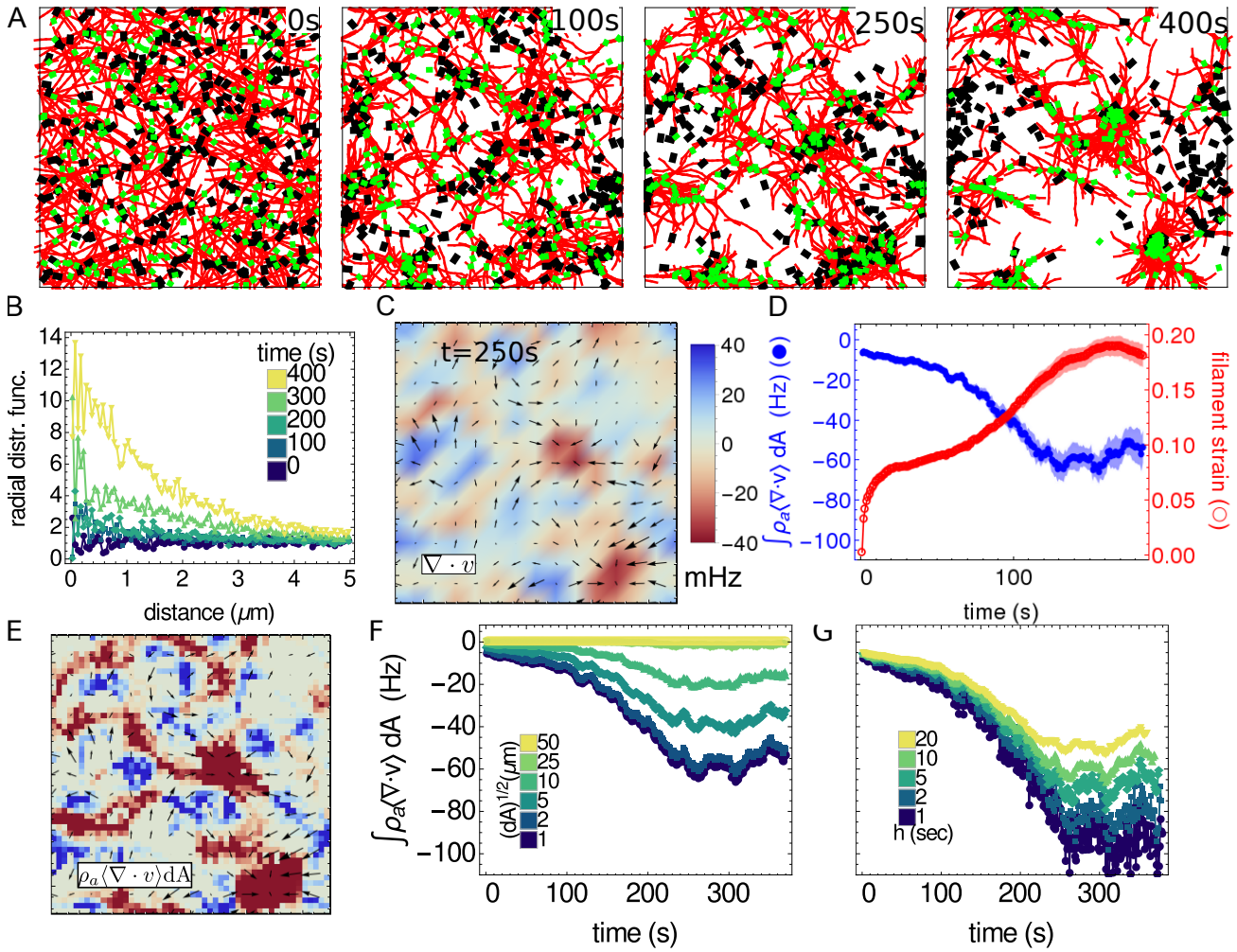

Figure 2.14: Calculation of density weighted divergence for a simulated contractile actomyosin network. (A-D) Identical to Fig. 2.7, but with $k_m^{off} = 10\ \text{s}^{-1}$, $k_m^{end} = 1\ \text{s}^{-1}$, and $\rho_m = 1\ \mu\text{m}^{-2}$. In (A), all filaments and 10% of motors and crosslinkers are shown. (E) Same as (C), but the color is weighted by the actin density ρ_a. (F) Dependence of the density weighted divergence on the patch size used for integration, $dA = dxdy$, with $h = 10$ s. (G) Dependence of the density weighted divergence on the time scale h used in calculating the velocity of actin v in Eq. 2.19 with $dx = dy = 1\ \mu$m.

CHAPTER 3

NONEQUILIBRIUM PHASE DIAGRAMS FOR ACTOMYOSIN NETWORKS

This chapter was originally published as Ref. 45 with coauthors Glen Hocky, Shiladitya Banerjee, and Aaron Dinner.

Living cells dynamically modulate the local morphologies of their actin cytoskeletons to perform biological functions, including force transduction, intracellular transport, and cell division. A major challenge is to understand how diverse structures of the actin cytoskeleton are assembled from a limited set of molecular building blocks. Here we study the spontaneous self-assembly of a minimal model of cytoskeletal materials, consisting of semiflexible actin filaments, crosslinkers, and molecular motors. Using coarse-grained simulations, we demonstrate that by changing concentrations and kinetics of crosslinkers and motors, as well as filament lengths, we can generate three distinct structural phases of actomyosin assemblies: bundled, polarity-sorted, and contracted. We introduce new metrics to distinguish these structural phases and demonstrate their functional roles. We find that the binding kinetics of motors and crosslinkers can be tuned to optimize contractile force generation, motor transport, and mechanical response. By quantitatively characterizing the relationships between the modes of cytoskeletal self-assembly, the resulting structures, and their functional consequences, our work suggests new principles for the design of active materials.

3.1 Introduction

Mechanical functions of living cells are determined by dynamic restructuring of the actin cytoskeleton, a highly conserved cellular machinery composed of filamentous actin (F-actin), myosin molecular motors, and crosslinking proteins [121]. An enormous variety of F-actin binding proteins with diverse physicochemical properties [113] can combine with F-actin to assemble function-specific cellular structures. Spatiotemporal control over these structures is

essential for coordinated force generation during cell migration [136, 105], cell adhesion [132], cytokinesis [154], and intracellular transport [119, 164]. A quantitative understanding of how diverse cytoskeletal structures are assembled from a limited set of molecular building blocks presents an outstanding challenge at the interface of soft matter physics and cell biology.

Much effort has been devoted to understanding how contracted states arise in actomyosin networks that lack sarcomeric organization. One mechanism that has emerged is that actin filaments rectify randomly directed forces to select for contractile ones because they can buckle readily but cannot stretch significantly [33, 95, 94, 123, 93, 142]. Alternatively, crosslinking can arrest relative sliding of filaments as they increase their overlap [120, 159] (see also [160] in the context of microtubules). The prevalence of these mechanisms and, in turn, contractile dynamics, depends on motor density and activity [7, 123, 120, 101, 6], network connectivity [7, 2, 35, 24], actin filament turnover [69], and filament stiffness [159].

Sufficient variation of system parameters leads to other states. Networks with low densities of motors exhibit bundled morphologies [7, 149, 28, 8]; lattice-like (lamellar) and clustered morphologies have been seen in simulations as well [28]. Consistent with experiments and simulations of microtubules [124, 163] as well as theories of active gels [88], polarity-sorted asters of crosslinked actin bundles have also been observed [159]. Understanding how these diverse structures relate and can be elicited requires systematically mapping phase diagrams for networks of filaments, motors, and crosslinkers in terms of both molecular parameters (e.g., association and dissociation kinetics, molecular sizes, binding geometries, and microscopic mechanical properties) and system parameters (e.g., molecular composition, turnover, system geometries, external forces).

In this paper, we take a step towards this goal. We investigate the structures accessible to a coarse-grained model that has been parameterized to represent actomyosin networks involving only a single crosslinking protein that binds without geometric restrictions. We consider the interplay of motor and crosslinker density, their binding kinetics, and filament length. We observe homogeneous, contracted, bundled, and polarity sorted structures and

introduce order parameters that quantify their prevalence. We then explore the materials properties of these structures. Specifically, we examine the viscoelastic response to shear strain and the motor transport properties. Our study thus unifies previously observed structures in a single model, reveals the dependence of these structures on molecular parameters, and links the structures to functional consequences.

3.2 Results and Discussion

3.2.1 Model

To study the spontaneous self-assembly of cytoskeletal structures at experimentally relevant length and time scales (microns and minutes), we use AFINES, a simulation framework we recently developed [44]. In brief, actin filaments are modeled as polar worm-like chains (represented by beads connected by springs) with defined barbed and pointed ends (Fig. 3.1); crosslinkers are modeled as linear springs with ends (heads) that can stochastically bind and unbind from F-actin via a kinetic Monte Carlo procedure that preserves detailed balance; molecular motors are modeled as active crosslinkers such that once bound, they walk toward the barbed ends of filaments at load-dependent speeds. While competing simulation frameworks are available and have their advantages [126, 137], a unique feature of AFINES is its preservation of detailed balance in the absence of motors [44]. Treating the physics of passive systems correctly facilitates their comparison with active systems and, in turn, interpretation of the simulations.

We use Brownian dynamics to evolve the positions of constituents in 2D. The choice of dimension is consistent with the fact that actomyosin networks reconstituted *in vitro* are typically restricted to a region close to a supporting substrate [149, 123, 159]. At the same time, to reflect the finite thickness of the experimental systems and enable rearrangement in 2D, we neglect excluded volume. For this reason, we restrict our attention to actin concentrations at which we expect the network connectivity to dominate the dynamics.

This precludes modeling active nematic systems [146, 186], previously studied by others [96, 11, 31]; it may also lead to quantitative artifacts in the rates of structure formation (owing to a lack of entanglement [42]) and in density-dependent statistics of states with features such as contracted clusters or bundles. Overall, however, the model yields results in good agreement with observations for many cases of experimental interest [44, 159]. The model is described in detail in Chapter 2, and Table 3.1 lists all simulation parameters.

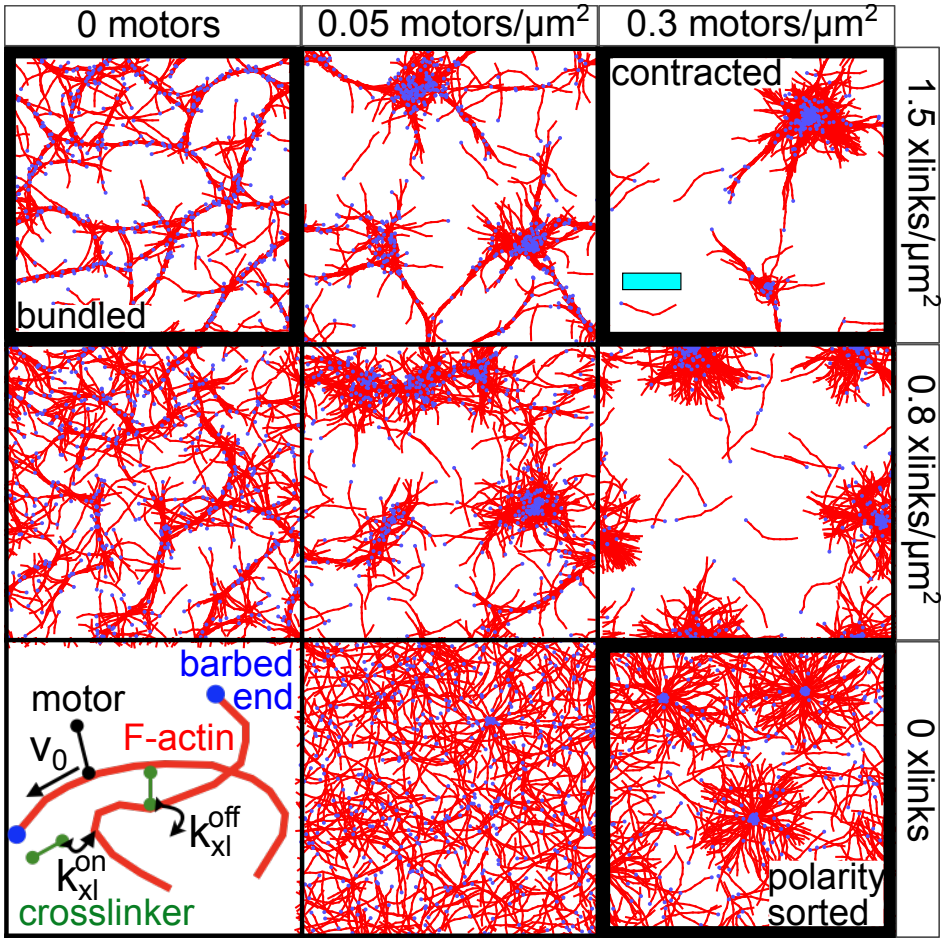

Figure 3.1: Network structures. (lower left) Schematic of the model [44] with F-actin (red), crosslinkers (green), and motors (black). Bound motors walk towards F-actin barbed ends (blue). (remaining panels) Network structures at 400 s for indicated motor and crosslinker densities. These include a bundled network (upper left) formed by filaments and crosslinkers, a polarity-sorted network (lower right) formed by filaments and motors, and a contracted network (upper right) formed from filaments, crosslinkers, and motors. For clarity, only the actin filaments are shown; the motors and crosslinkers are shown in Fig. 3.8. Cyan scale bar represents 10 μm.

3.2.2 Network structures

We observe three distinct network architectures formed from initially disordered mixtures of F-actin, motors, and crosslinkers: bundled, polarity-sorted, and contracted. Examples are shown for simulations of 500 10-μm-long filaments in Fig. 3.1. When F-actin is mixed with crosslinkers, thick bundles form and intersect to yield a well-connected mesh. When F-actin is mixed with motors, barbed ends aggregate to form a polarity-sorted network. Combining F-actin with both motors and crosslinkers results in macroscopic contraction of the filaments into dense and disconnected aggregates. These structures are qualitatively consistent with recent experimental observations [178, 159].

3.2.3 Order parameters for characterization of network structures

To systematically explore how varying the properties of the network constituents affects structure formation, we introduce order parameters that characterize each of the observed structures. We compute the spatial extent of F-actin aggregation using the radial distribution function,

$$g(r) = P(r)/(2\pi r \delta r \rho_a) \tag{3.1}$$

where $P(r)$ is the probability that two actin beads are separated by a distance in the range $[r, r+\delta r]$ (here, $\delta r = 0.05$ μm), and ρ_a is the number density of actin beads. For a homogeneous network, $g(r) \approx 1$ at all distances (Fig. 3.2A; the small peaks at integer r arise from the spacing of beads within actin filaments). In contrast, for contracted networks, $g(r) \gg 1$ for $r < 10\mu$m, indicating F-actin exceeds the bulk density, as observed experimentally [123].

While Fig. 3.2A shows that actin filaments are nearly uniformly distributed in polarity-sorted networks, Fig. 3.1 indicates that their barbed ends are concentrated. To quantify their aggregation specifically, we compute the ratio $g(r_{barb})/g(r)$, where r_{barb} is the distance between barbed ends. Fig. 3.2B shows that in polarity-sorted networks F-actin barbed ends aggregate (and have a secondary peak at 0.5μm, the rest length of motors). In contracted

networks, barbed ends also aggregate to a higher degree than in bundled networks, indicating a degree of polarity sorting. This is consistent with recent experiments that indeed show that contracted F-actin forms polarity sorted asters [159].

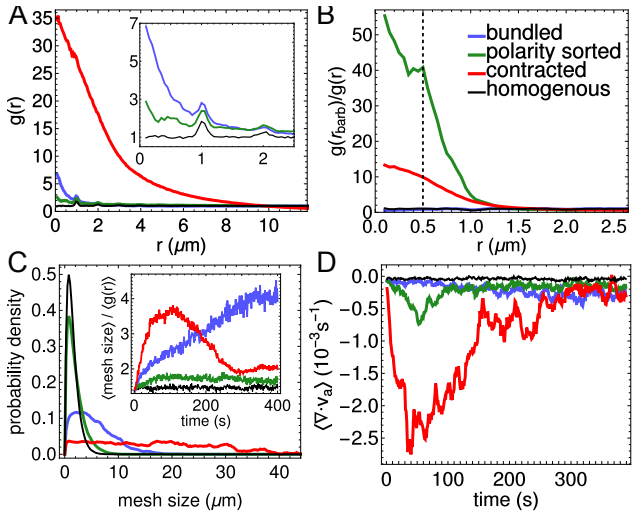

Figure 3.2: Order parameters. Bundled, polarity-sorted, and contracted cases correspond to the conditions highlighted in Fig. 3.1; the homogeneous case has no motors or crosslinkers. (A) Radial distribution function of actin, $g(r)$. (B) Radial distribution function of F-actin barbed ends, normalized by $g(r)$; the dashed line marks the motor rest length, 0.5 μm. (C) Mesh size distribution. Inset: Evolution of the average mesh size, normalized by $\langle g(r) \rangle$. (D) Spatially averaged divergence (Section 3.4.1). All averages are over the final 50 s of 5 simulations of 400 s.

The inset to Fig. 3.2A indicates that bundled networks aggregate at length scales comparable to the crosslinker rest length, $l_{xl} = 0.15\mu$m. To quantify the degree of bundling, and to distinguish it from contractility, we measure the distribution of network pore sizes by a procedure that is similar in spirit but simpler than that in Ref. 114. Namely, we grid the simulation box into $(0.25\mu\text{m})^2$ bins and compute how many filaments pass through each. For each empty bin, we determine the lengths of the contiguous vertical and horizontal stretches of empty bins that intersect it (Fig. 3.3). We average these lengths over all empty bins to obtain an average mesh size for each structure. This procedure can be used for analysis of experimental images, in addition to the simulation structures in the present study.

In Fig. 3.2C, the distributions of mesh sizes for polarity-sorted and homogeneous networks

are similar, indicating that the former does not coarsen significantly. The bundled and contracted networks exhibit larger pore sizes; indeed, contracted networks exhibit pore sizes spanning the simulation region, indicating that the network has ripped apart. We can distinguish these cases by normalizing the mesh size by $\langle g(r) \rangle = (1/R) \int_0^R g(r) dr$, (here, $R = 10\mu$m is the approximate size of a contracted aggregate under our maximally contractile conditions, as shown in Fig. 3.2A; see Fig. 3.9 for further details) which quantifies the extent of aggregation. The inset shows that, while the contracted networks initially bundle, at long times this effect is small compared to aggregation. In contrast, bundled networks have a steadily increasing normalized mesh size (Fig. 3.2C, inset), consistent with continuous coarsening of filamin crosslinked networks of long actin filament bundles [178]. We thus have a metric for the degree of bundling.

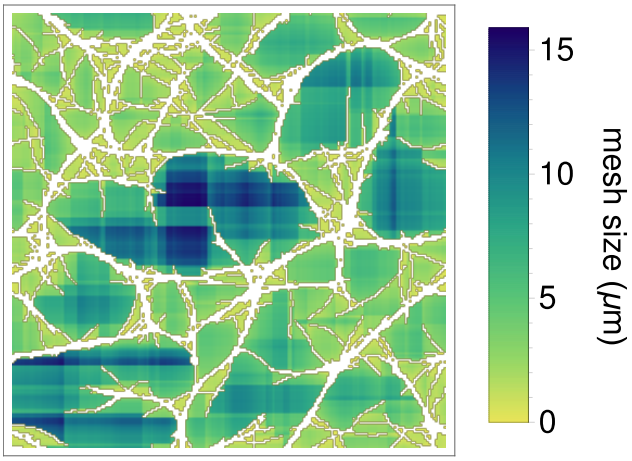

Figure 3.3: Example of mesh size calculation described in the text. Actin is shown in white (compare with bundled structure in Fig. 3.1) and the size of the local mesh corresponds to the depth of color, as indicated by the scale.

To examine the relationship between actin network structure and contractility, we use the divergence of actin's velocity field, $\langle \nabla \cdot \mathbf{v} \rangle$, where $\langle ... \rangle$ indicates spatial averaging (Section 3.4.1) [44]. As shown in Fig. 3.2D, $\langle \nabla \cdot \mathbf{v} \rangle$ becomes significantly more negative for aggregating networks than for bundling or polarity-sorted networks. Comparison with Fig. 3.2A shows that extensive contraction is associated with large $g(r)$.

3.2.4 Phase diagram for molecular composition

Using these order parameters, we map the structural phase diagram of actomyosin networks as functions of motor and crosslinker densities (Fig. 3.4). Consistent with Fig. 3.1, networks are contracted when motor and crosslinker densities are high (Fig. 3.4A), polarity-sorted when only motor density is high (Fig. 3.4B), and bundled when crosslinker density is high (Fig. 3.4C). These results echo observations in experiments and simulations that at low motor density, crosslinkers can bundle actin into meshes [7, 8], and at high motor density, crosslinkers promote contractility by increasing network connectivity [7, 33, 8, 107]. While polarity sorting is not usually observed independent of contractility in actomyosin networks, our result that increasing motor density promotes this effect is consistent with previous experimental observations and simulations of microtubules interacting with plus-end oriented motors [163]. Furthermore recent experiments on reconsituted actomyosin networks show that rigid F-actin bundles can form polarity-sorted structures without undergoing bulk contraction [159].

Interestingly, we also observe one non-monotonic trend in this phase diagram: while high motor densities inhibit bundling, a small population of motors ($\rho_m \approx 0.02\mu\text{m}^{-2}$) enhances bundling. Other non-monotonic trends have been reported, including that high crosslinker densities [7, 35], and more surprisingly, high motor force [2] can inhibit contractility and yield bundled or critically connected networks. We did not observe these effects in the ranges of densities that we considered. This may be because our crosslinker-to-filament ratios (up to 7.5:1) are lower than observed thresholds for crosslinker inhibition (ranging from 15:1 [35] to ¿90:1 [7]); we expect this threshold to depend on the kinetics of association, as we now discuss.

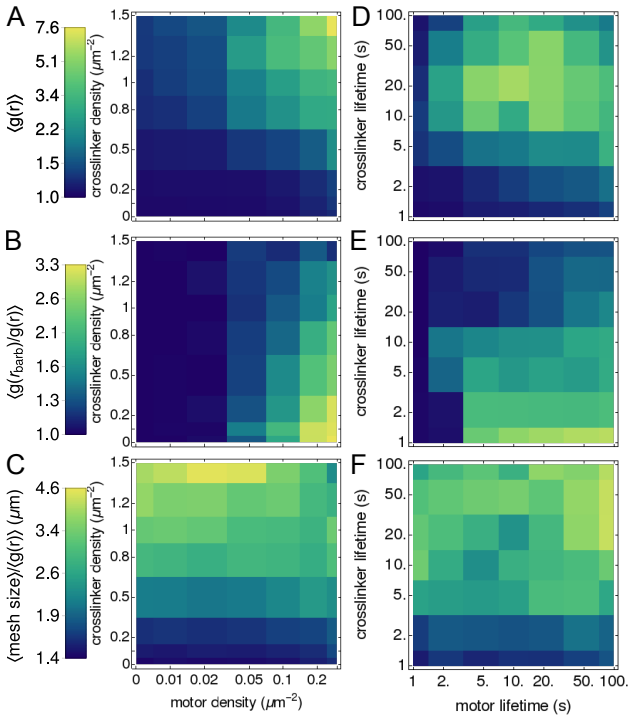

Figure 3.4: Maps of network properties. Colors indicate the values of order parameters characterizing network contractility (A,D), polarity sorting (B,E), and bundling (C,F), at constant filament length, $L = 10\mu$m, binding affinity $k_m^{\text{off}} = k_{xl}^{\text{off}} = 0.1$ s^{-1} (left), and densities $\rho_m = 0.2\mu\text{m}^{-2}$, $\rho_{xl} = 1\mu\text{m}^{-2}$ (right, plotted as a function of lifetime, $1/k_{m(xl)}^{\text{off}}$; structures shown in Fig. 3.12). Averages are over the last 50 s of five simulations of 400 s; order parameters that are functions of distance, e.g., $g(r)$, are integrated over $0 < r \leq 10\mu$m. Error bars for representative curves are shown in Fig. 3.10.

3.2.5 Phase diagram for binding kinetics

We also modulate molecular-level interaction parameters between F-actin and its binding partners (crosslinkers, motors), and dissect their relative roles in building different structures. These parameters are hard to control in experiment because they require modifying protein-protein interactions. At fixed motor and crosslinker densities, we find that cytoskeletal structures can be tuned by varying the dissociation constants, $k_{m(xl)}^{\text{off}}$ (Fig. 3.4D-F). The trends are non-monotonic, in contrast to those in Fig. 3.4A-B. In particular, contraction is highest for intermediate values of $k_{m(xl)}^{\text{off}}$ (Fig. 3.4D), similar to observations that increasing motor and crosslinker densities beyond a threshold inhibits contraction [7, 2, 35]. Bundling

is highest for low values of k_{xl}^{off} with low or high k_m^{off} (Fig. 3.4F). Notably, this non-monotonic trend only arises for a fixed simulation time, t_F. For a fixed value of $t_F k_{m(xl)}^{\text{off}}$, changing $1/k_{m(xl)}^{\text{off}}$ modulates structure formation in a monotonic manner (dashed lines in Fig. 3.5). The non-monotonic trends are important, however, for understanding how structures form in the presence of competing kinetic processes, such as turnover of different network elements [119, 46].

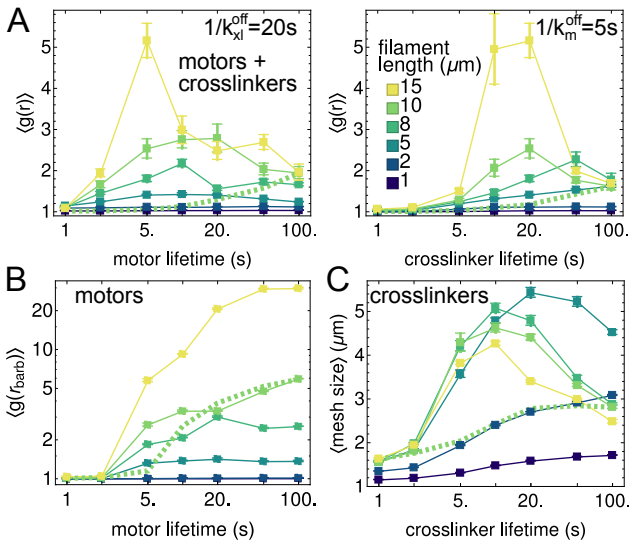

Figure 3.5: Effects of varying motor and crosslinker lifetimes, $1/k_{m(xl)}^{\text{off}}$, for filaments of different lengths, L, at $t_f = 400$ s (filled squares). (A) Contractility order parameter, radial distribution function, for mixtures of filaments, motors, and crosslinkers with $\rho_m = 0.2\mu\text{m}^{-2}$ and $\rho_{xl} = 1\mu\text{m}^{-2}$. (B) Polarity sorting order parameter, radial distribution function of barbed ends, for mixtures of filaments and motors, without crosslinkers. (C) Bundling order parameter, mesh size, for mixtures of filaments and crosslinkers, without motors. Normalizing quantities in (B) and (C) with respect to $\langle g(r)\rangle$ does not change the qualitative behaviors (Fig. 3.11). Error bars indicate standard error of the mean. The green dashed lines show how order parameters vary for one length, $L = 10\mu$m, if the corresponding green squares are rescaled such that $t_f = 4/k_{xl(m)}^{\text{off}}$.

3.2.6 Effect of filament length

As the length (L) of F-actin varies considerably within cells [116], we tested how modulating L and $k_{m(xl)}^{\text{off}}$ in tandem affects structure formation. In Fig. 3.5A, we show that increasing L favors aggregation by increasing network connectivity; short filaments ($L < 5\mu$m) do not

organize. As in Fig. 3.4D, the dependence of aggregation on binding affinity is non-monotonic whenever there is significant aggregation (i.e., $L \geq 5\mu$m). In Fig. 3.5B, we show that for networks with only motors, at low k_m^{off}, increasing filament length promotes polarity sorting. By contrast, at high k_m^{off}, short lifetimes of motor attachment suppress polarity sorting. As evident from the representative network structures in Fig. 3.13, shortening the filaments also suppresses polarity sorting.

For networks with only crosslinkers, the mesh size (Fig. 3.5C) is non-monotonic with respect to both filament length and crosslinker affinity. Low crosslinker affinity and short filament lengths prevent forming stably crosslinked networks (Fig. 3.14). Conversely, assemblies with high crosslinker affinity or long filament lengths form crosslinked networks, but they rearrange slowly, so further coarsening is impeded, and the mesh size remains small. As these non-monotonic trends only occur for $L > 5$ μm, they are more likely to impact structures with longer actin filaments found in budding yeast [22], stereocilia [99], filopodia, or reconstituted *in vitro* [178, 159] (though we note that long microtubules have been obseved to form different structures in the presence and absence of a membrane [133]). Structures with shorter filaments, as found in lamellipodia or the actin cortex (< 2 μm) [145, 24], are less likely to have a finite binding affinity that maximizes contractility. We discuss the effects of length further in conjunction with the mechanical response of networks, below.

3.2.7 Network structure tunes molecular transport

While the structures of contracted, polarity-sorted, and bundled networks clearly differ, their consequences for biophysical functions are not immediately apparent. To determine how these structures influence motor transport [15, 83], we follow the dynamics of small numbers of motors introduced after the structures form (Fig. 3.6A). In Fig. 3.6B, we plot their mean-squared displacement,

$$\text{MSD}(t_f, \Delta) = \frac{1}{t_f - \Delta} \int_0^{t_f - \Delta} [\vec{v}_m(t, \Delta)]^2 dt \tag{3.2}$$

where t_f is the length of the trajectory and $\vec{v}_m(t,\Delta) = \vec{r}_m(t+\Delta) - \vec{r}_m(t)$ is the displacement of a motor with center of mass position $\vec{r}_m(t)$ at time t after a lag of Δ. While the scaling of the mean-squared displacement is consistent with simple diffusion (Fig. 3.6B), sample trajectories (Fig. 3.6A) indicate that motors in contracted and polarity-sorted structures spend significant amounts of time trapped in aggregates of barbed ends.

We quantify caging using a previously defined metric that can distinguish different kinds of motion [18]: we compute the distribution of angles, θ, between consecutive displacement vectors $\vec{v}_m(t,\Delta)$ and $\vec{v}_m(t+\Delta,\Delta)$, at different values of Δ. We find that for all structures, there is at least one time scale in which the distribution has a broad peak at $\theta = \pi$ (Fig. 3.6C), indicating that motors are reversing direction, consistent with confinement [18]. For polarity-sorted networks, barbed ends are tightly aggregated, and the motors exhibit caging at all time scales measured. Contracted networks are partially polarity-sorted, so filaments can direct motors both in and out of aggregates, making the caging more spatially extended. Because it takes longer to explore the extended length scale, the peak has is smaller than in the polarity sorted network. Bundled networks exhibit peaks at both $\theta = 0$ and $\theta = \pi$ depending on the time scale. The former corresponds to moving steadily along a filament, while the latter corresponds to switching between oppositely oriented filaments.

Consistent with our results, it was recently shown that actin networks with different structures result in different angle distributions [152]. As in our results for bundled networks, reconstituted networks of actin and filamin supported simultaneous peaks at $\theta = 0$ and $\theta = \pi$ at short times (0.1 s)[152]. Interestingly, in our simulations, the peak at $\theta = \pi$ diminishes at intermediate times. A key feature of the experiments that is not represented in the present model is that the myosin minifilaments in the experiments have many heads [18, 151, 152], and this was previously shown to be important for observed glassy dynamics [151].

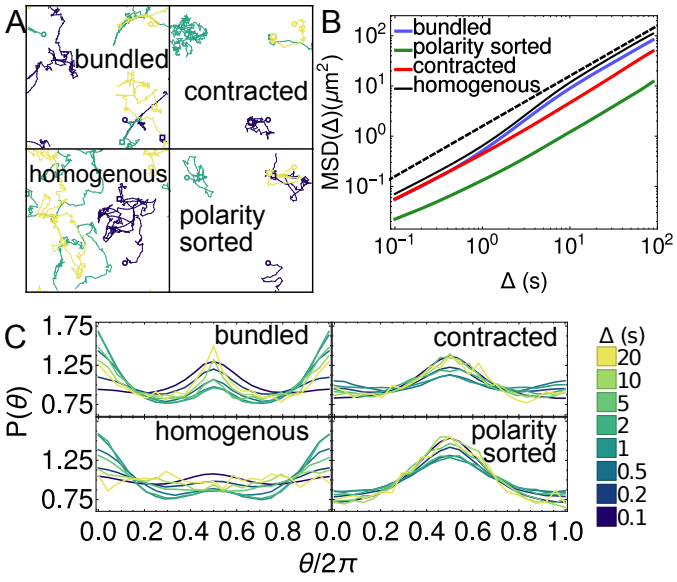

Figure 3.6: Transport properties of motors on actin structures. (A) Example trajectories of three motors (each a different color) on actin networks (filaments shown in Fig. 3.1 and Fig. 3.8). Open circles show initial position of each motor, and open squares show their final position after 500 timesteps. (B) Mean squared displacement for motors on structures. Black dashed line shows diffusive behavior, $\mathrm{MSD}(t_f, \Delta) \propto \Delta$. (C) Distributions of angles between subsequent motor displacements for different lag times, Δ[18]. Averages in (B-C) are over 770 motors over the last 100 s of 5 independent trajectories of 200 s, at each condition.

3.2.8 Network structure tunes mechanical response

Next, we evaluated how structural rearrangements in actin networks affect their ability to propagate mechanical forces over long length scales. To this end, we subjected the final network configuration to a shear strain of magnitude $\gamma = 0.5$ (Fig. 3.7A, algorithm described in Section 3.4.2) and measured the resulting strain energy. In Fig. 3.7B, we show the strain dependence of the strain energy density, $w(\gamma) - w(0)$, where

$$w(\gamma) = (U_f(\gamma) + U_m(\gamma) + U_{xl}(\gamma))/V, \tag{3.3}$$

U_f, U_m, and U_{xl} are the potential energies of the F-actin, motors, and crosslinkers, respectively, (Chapter 2) and $V = 250\mu\mathrm{m}^3$ is the simulation volume, assuming a thickness of 0.1μm. To determine the viscoelastic response of the material, we fit the computed strain

energy density to the function $1/2G\gamma^2 + \eta\dot{\gamma}\gamma$ where G is the shear modulus, η is the dynamic viscosity, and $\dot{\gamma} = 1\ \mathrm{s}^{-1}$ is the strain rate (see Section 3.4.2 for details) [13].

We found that bundled networks exhibited the most solid-like material response ($G = 1.07$ Pa, within range of experimentally measured values for actin-filamin networks [149], and $\eta = 0.007\ \mathrm{Pa \cdot s}$), while polarity-sorted and homogenous networks exhibited fluid-like responses ($G \approx 0, \eta = 0.080,\ 0.014\ \mathrm{Pa \cdot s}$ respectively). Contracted networks exhibited a viscoelastic response ($G = 0.30$ Pa, $\eta = 0.063\ \mathrm{Pa \cdot s}$), consistent with theoretical predictions from active gel models [103, 5].

We used this method to measure the material response of the broad spectrum of structures that resulted from varying motor and crosslinker densities, and the various bundled networks that resulted from varying filament length and crosslinker lifetime. We find that these structures can be elastic ($\eta \approx 0$), viscous ($G \approx 0$), or viscoelastic (nonzero G and η). The viscous systems exhibit no quadratic response to strain because they are not well-connected (indicating there exists a percolation threshold). For a given crosslinker lifetime ($1/k_{xl}^{\mathrm{off}} = 10$ s) and filament length (10μm), we find that all networks below $\rho_{xl} = 0.05\mu\mathrm{m}^{-2}$ have $G \approx 0$ and high viscosity (Fig. 3.7C,E). Therefore, $\rho_{xl} = 0.05\mu\mathrm{m}^{-2}$ defines the percolation threshold of the gel, which is independent of motor density. Above the percolation threshold, networks have a range of viscoleastic behavior, with low motor density yielding more elastic behavior, and high motor density yielding more viscous behavior. For networks without motors, increasing the crosslinker concentration yielded higher shear elastic moduli, consistent with theoretical predictions [65], experiments [51, 149], and previous simulations [80].

In Fig. 3.7D,F we show that even at high crosslinker density ($1.2\mu\mathrm{m}^{-2}$), the network can respond as a fluid if the crosslinker lifetime or filament length is sufficiently low ($1/k_{xl}^{\mathrm{off}} \leq 2$ s or $L \leq 5\mu$m). At intermediate lifetimes, such as for the crosslinker filamin ($1/k_{xl}^{\mathrm{off}} \approx 10$ s), our results agree with experiments: below a critical length, networks respond as fluids [178], and increases in filament length lead to increases in the elastic modulus [78]. At the longest filament lengths (15μm) and crosslinker lifetimes (≥ 50 s), crosslinked networks are nearly

solid with $\eta \approx 0$. A viscoelastic regime occurs at intermediate values of filament length and crosslinker lifetime, corresponding to the networks with the largest mesh sizes (Fig. 3.5C).

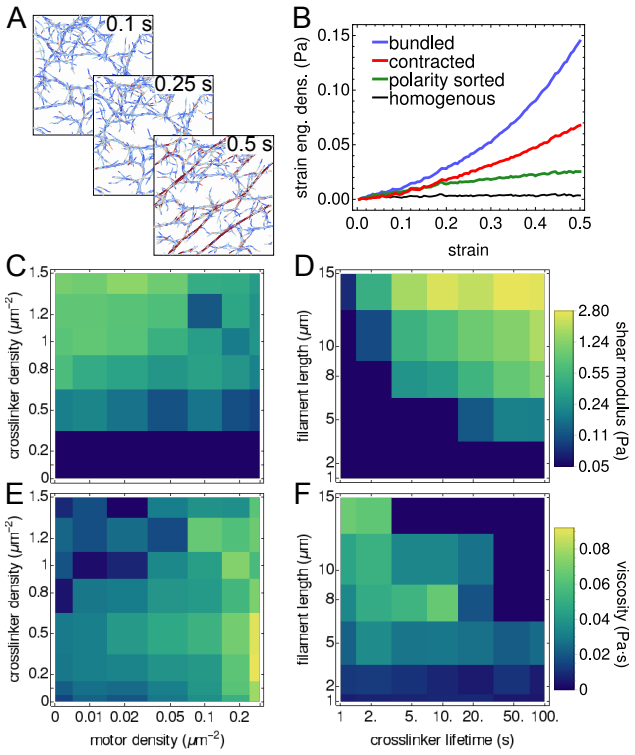

Figure 3.7: Elasticity of network structures. (A) Shearing a bundled network for 0.5 s at a strain rate of $\dot{\gamma} = 1/\text{s}$. Depth of color indicates stretch of filament. (B) Viscoelastic response of the network to a simple shear, as measured by the dependence of the strain energy density on the strain. (C-D) Shear modulus of structures (shown in Fig. 3.1) formed with constant filament length ($L = 10\mu\text{m}$) and lifetimes ($1/k^{\text{off}}_{xl,m} = 10$ s), but different motor and crosslinker densities (C), and for structures (shown in Fig. 3.14) formed without motors and constant crosslinker density ($\rho_{xl} = 1.2\mu\text{m}^{-2}$), with different filament lengths and crosslinker lifetimes (D). (E-F) Viscosity of these networks. Strain calculations in (B-F) are averaged over 5 independent trajectories.

3.3 Conclusion and Outlook

We have shown how modulating the abundance and physicochemical properties of cytoskeletal constituents can tune emergent network structures and in turn their materials properties. We also introduced order parameters that should facilitate analysis of other models and images from experiments. We find that motor and crosslinker binding affinities, as well as

filament lengths, have optimal values for maximizing contractility, bundling, and polarity sorting at finite times. From the perspective of materials design, our work demonstrates how a limited set of molecular building blocks can self-assemble diverse active materials.

In the present study, we consider only a single type of crosslinker (as defined by its stiffness and size), which binds without geometric restrictions. It would be straightforward to modify the energy function of the model to introduce geometric restrictions, and studies of passive systems indicate that such terms can introduce additional structural phases [28]. The model can also be extended to include actin polymerization and turnover, which have been shown to modulate contractility [107, 111] and bundling [42]. Finally, the model can be parameterized for other polymer assemblies, such as microtubules, kinesin, and dynein, which form vortices and polarity sorted asters [163, 127, 125].

Our framework can thus be built on to treat diverse types of crosslinkers, filaments, and motors. We expect that rich behavior can be achieved by simulating mixtures with four or more constituents. Because it is straightforward to vary the abundance and properties of the constituents computationally, they could be automatically optimized to achieve desired properties [115], and the results could inform the design and synthesis of new active materials.

3.4 Supplementary Information

Symbol	Description (units) [ref]	Value
	Actin Filaments	
ρ_l	link density (μm^{-2})	2
N_l	number of links per filament (L/l_a)	$[1, 15]$
l_a	link rest length (μm) [129]	1
k_a	stretching force constant (pN/μm)	5
κ_B	bending modulus (pNμm^2) [131]	0.068
	Myosin Minifilaments	
ρ_m	density (μm^{-2})	$[0, 0.3]$
l_m	rest length (μm) [128]	0.5
k_m	stiffness (pN/μm)	1
k_m^{on}	maximum attachment rate (s^{-1})	1
k_m^{off}	maximum detachment rate (s^{-1})	$[0.01, 1]$
k_m^{end}	maximum end detachment rate (s^{-1})	$[0.01, 1]$
v_0	unloaded speed (μm/s) [86]	1
F_s	stall force of myosin (pN) [173]	0.5
	Crosslinkers	
ρ_{xl}	density (μm^{-2})	$[0, 1.5]$
l_{xl}	rest length (filamin) (μm) [40]	0.15
k_{xl}	stiffness (pN/μm)	1
k_{xl}^{on}	maximum attachment rate (s^{-1})	1
k_{xl}^{off}	maximum detachment rate (s^{-1})	$[0.01, 1]$
	Environment	
Δt	dynamics timestep (s)	0.00002
t_F	maximum simulated time (s)	400
X, Y	length and width of assay (μm)	50
g	grid density (μm^{-1})	2.5
T	temperature (K)	300
ν	dynamic viscosity (Pa·s)	0.001

Table 3.1: Parameter Values

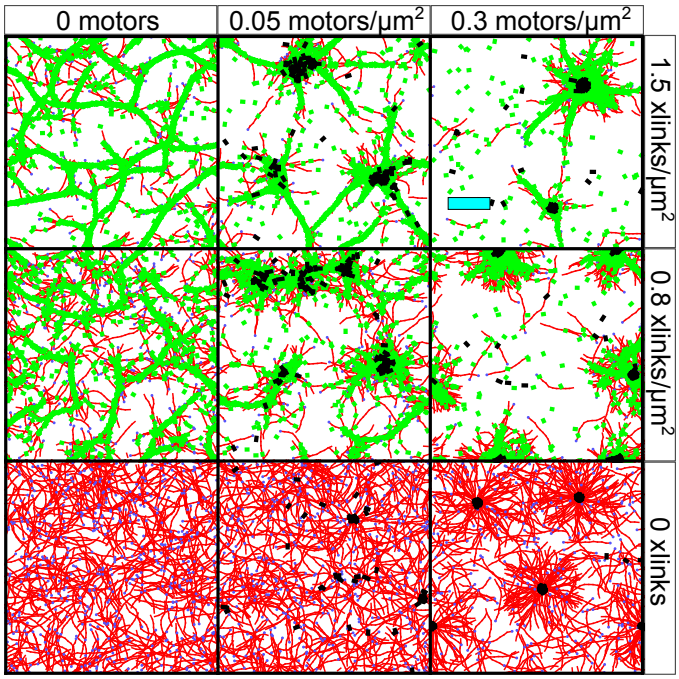

Figure 3.8: Same as Fig. 3.1, but with motors (black) and crosslinkers (green) also shown on top of actin (red, barbed ends marked by blue dots). Cyan scale bar is 10 μm. Parameters held constant: $L = 10\mu$m, $k_{xl(m)}^{\text{off}} = 0.1$ s^{-1}.

3.4.1 Actin velocity field calculation

Contraction of actin networks is typically calculated by identifying sinks in the divergence of the actin velocity field. To construct this field, we first calculate the velocity of actin beads $\vec{v}_a = (\vec{r}_a(t+h) - \vec{r}_a(t))/h$ where $\vec{r}_a(t)$ is the position of an actin bead at time t, and h is the lag time. To reduce noise, we calculate $\vec{v}_k(\vec{r_k})$, the average velocity in every bin k of size Δr^2. We then interpolate the velocity field using Gaussian radial basis functions (RBFs), such that the velocity at any position $\vec{r}$ is

$$\vec{v}(\vec{r}) = \sum_{k=1}^{M} \vec{w}_k e^{-(|\vec{r}-\vec{r}_k|/\epsilon)^2}, \tag{3.4}$$

where M is the number of bins with at least 10 actin beads, and $\vec{w}_k$ are the weights of the basis functions, determined by solving the equation $\vec{v}(\vec{r_k}) = \vec{v_k}(\vec{r_k})$ (using the scipy.interpolate.Rbf

package [67]). For Fig. 3.2B, we used a lag time of $h = 10$ s, a threshold of $n = 10$ actin beads in a local box of size $\Delta r = 5\mu$m, and a Gaussian width of $\epsilon = 5\mu$m, as we have found these interpolation values robustly capture the motion of the actin [44].

Because of the periodic boundary conditions, there is no flux of actin into the simulation cell, and $\langle \nabla \cdot \vec{v}(r) \rangle = 0$. Therefore, to measure contraction, we threshold the divergence by the local actin density and only total the divergence from $1\mu\text{m}^2$ patches that contain more than 5 actin beads in Fig. 3.2D, as in Ref. 159.

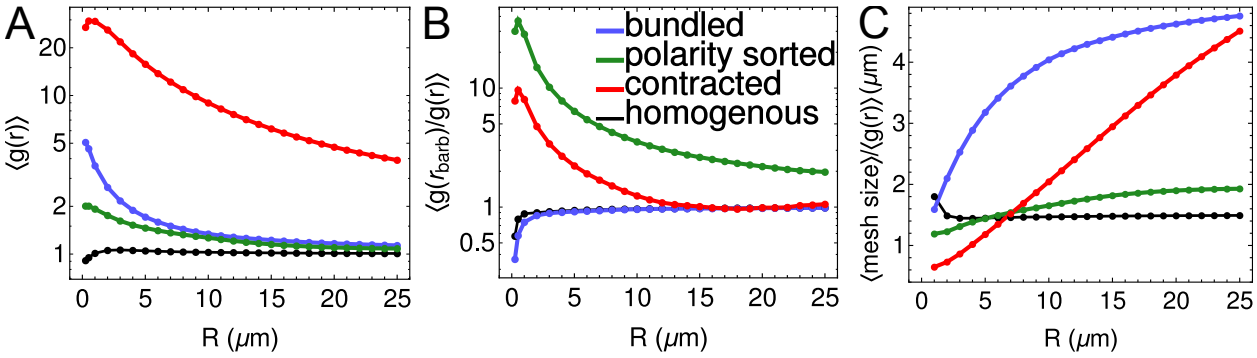

Figure 3.9: Variation of order parameters with R, the upper integration limit for $\langle g(r) \rangle$ and $\langle g(r_{barb}) \rangle$. Since the length and width of the periodic simulation cell is 50μm, the largest unambiguous distance is half that, 25μm. (A) For all values of R, $\langle g(r) \rangle$ is highest for contracted networks, followed by bundled networks. (B) For all values of R, $\langle g(r_{barb})/g(r) \rangle$ is highest for polarity-sorted networks, followed by contracted networks. (C) For $R > 1\mu$m, $\langle \text{mesh size}/g(r) \rangle$ is highest for bundled networks, consistently followed by contracted networks for $R \geq 8\mu$m.

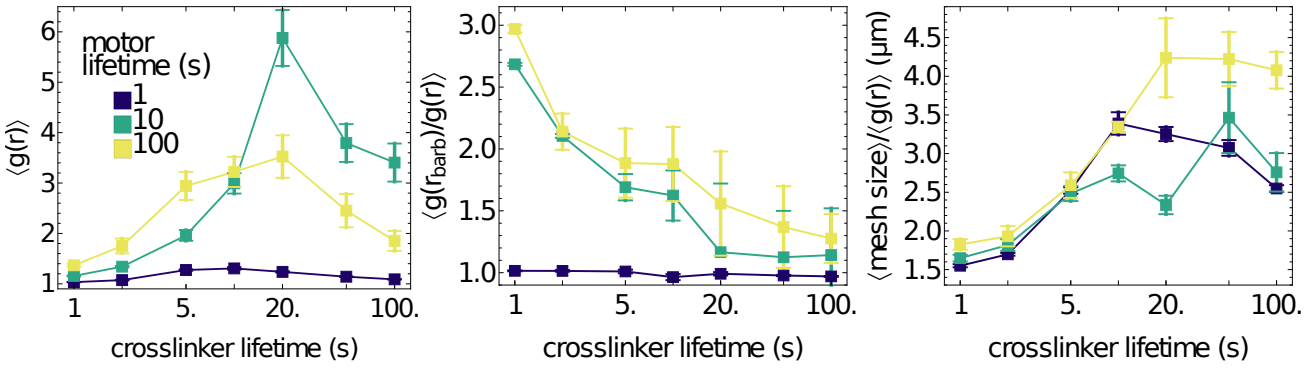

Figure 3.10: Example cuts from Fig. 3.4D-F to show typical sizes of standard errors of the means.

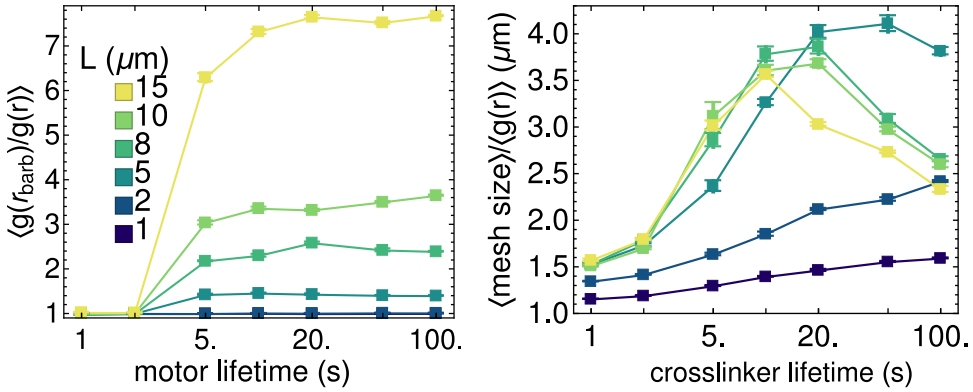

Figure 3.11: Same as Fig. 3.5B-C but normalized by $\langle g(r) \rangle$.

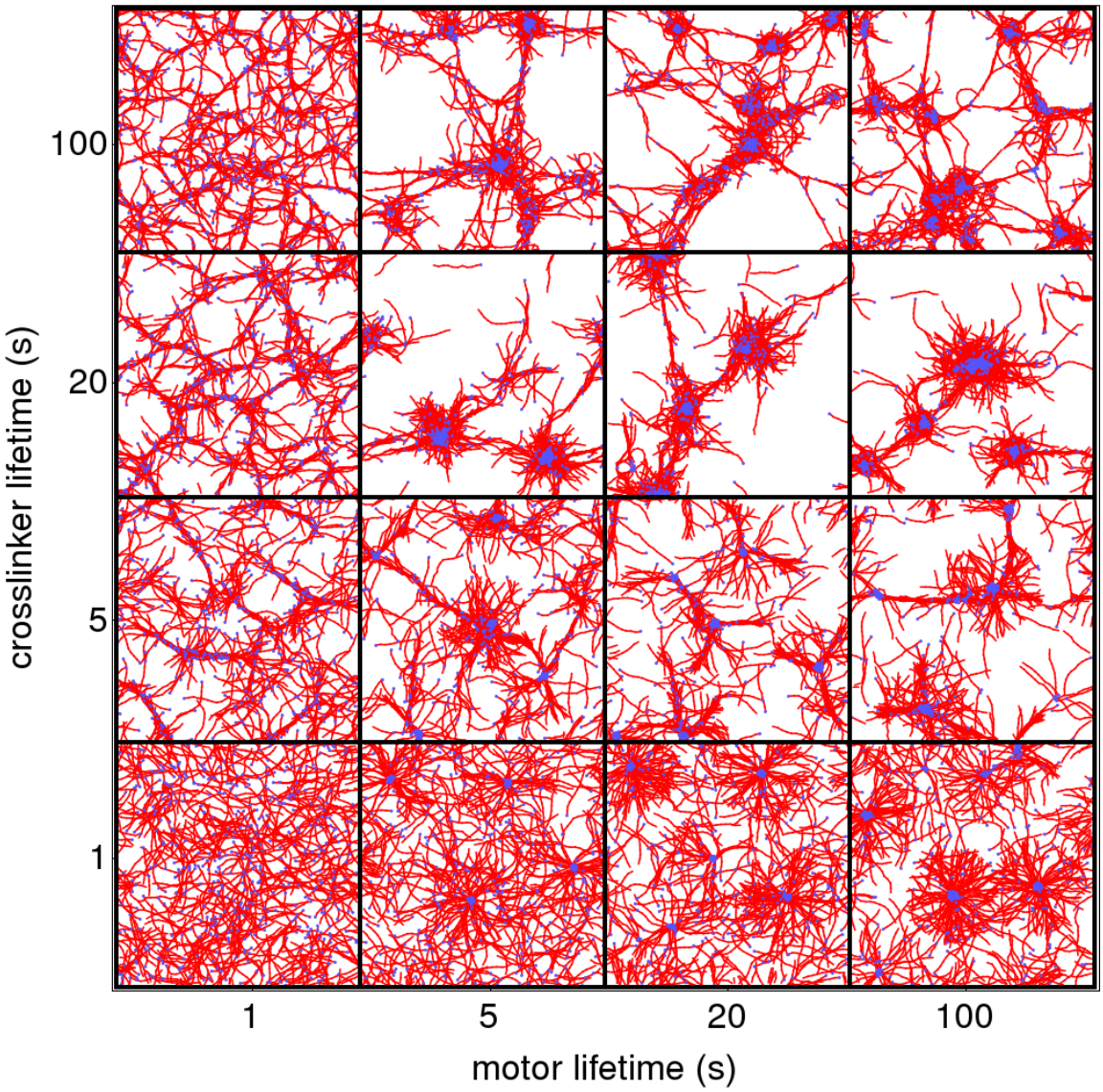

Figure 3.12: Sample structures after 400 s simulation, for varying motor and crosslinker off rates. Parameters held constant: $\rho_m = 0.2\ \mu\text{m}^{-2}$, $\rho_{xl} = 1\ \mu\text{m}^{-2}$, $L = 10\mu\text{m}$. Motors and crosslinkers not shown for clarity.

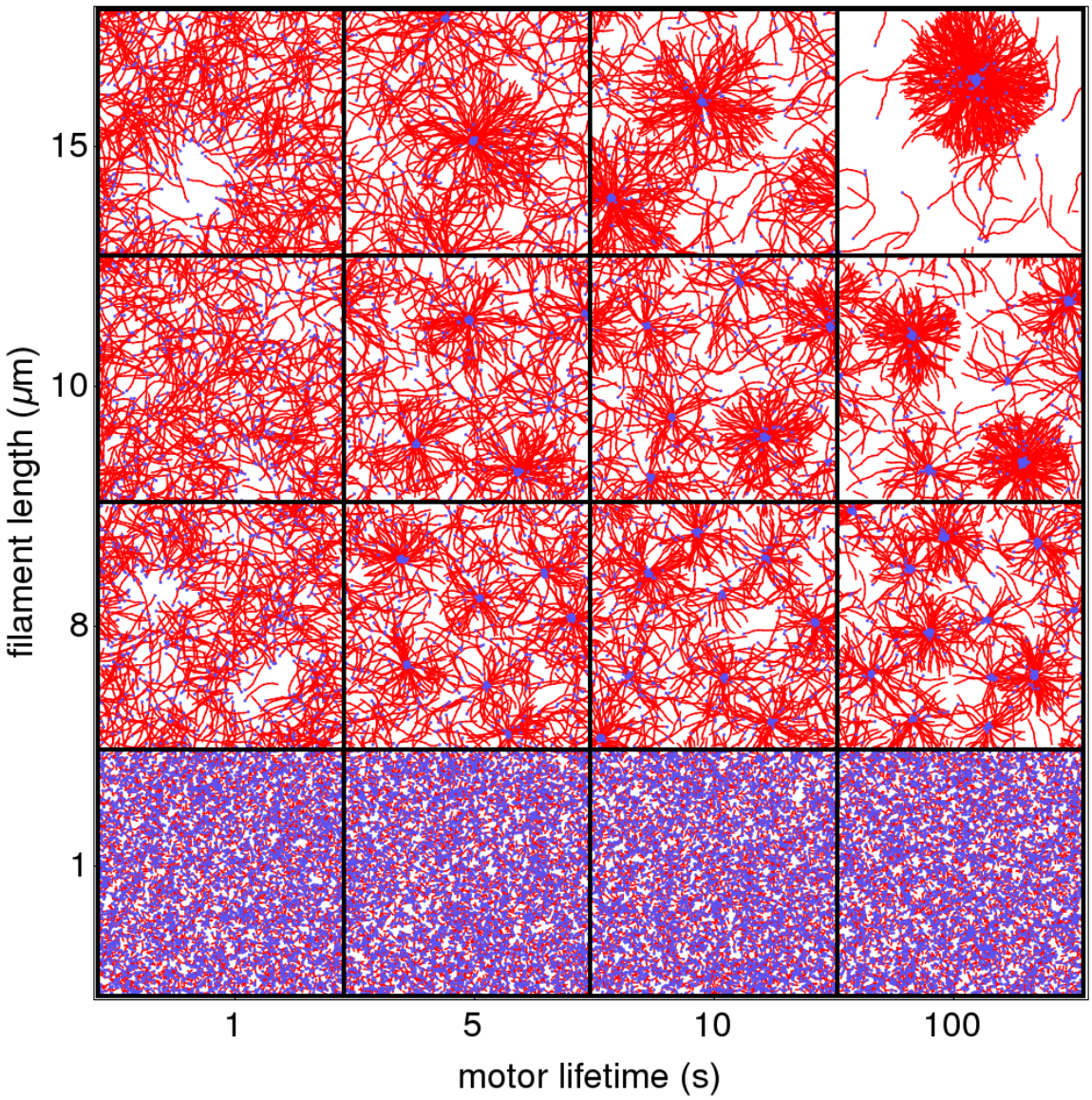

Figure 3.13: Sample structures after 400 s simulation, for varying filament length and motor off rate. Parameters held constant: $\rho_m = 0.3\ \mu\text{m}^{-2}$, $\rho_{xl} = 0$. Motors and crosslinkers not shown for clarity.

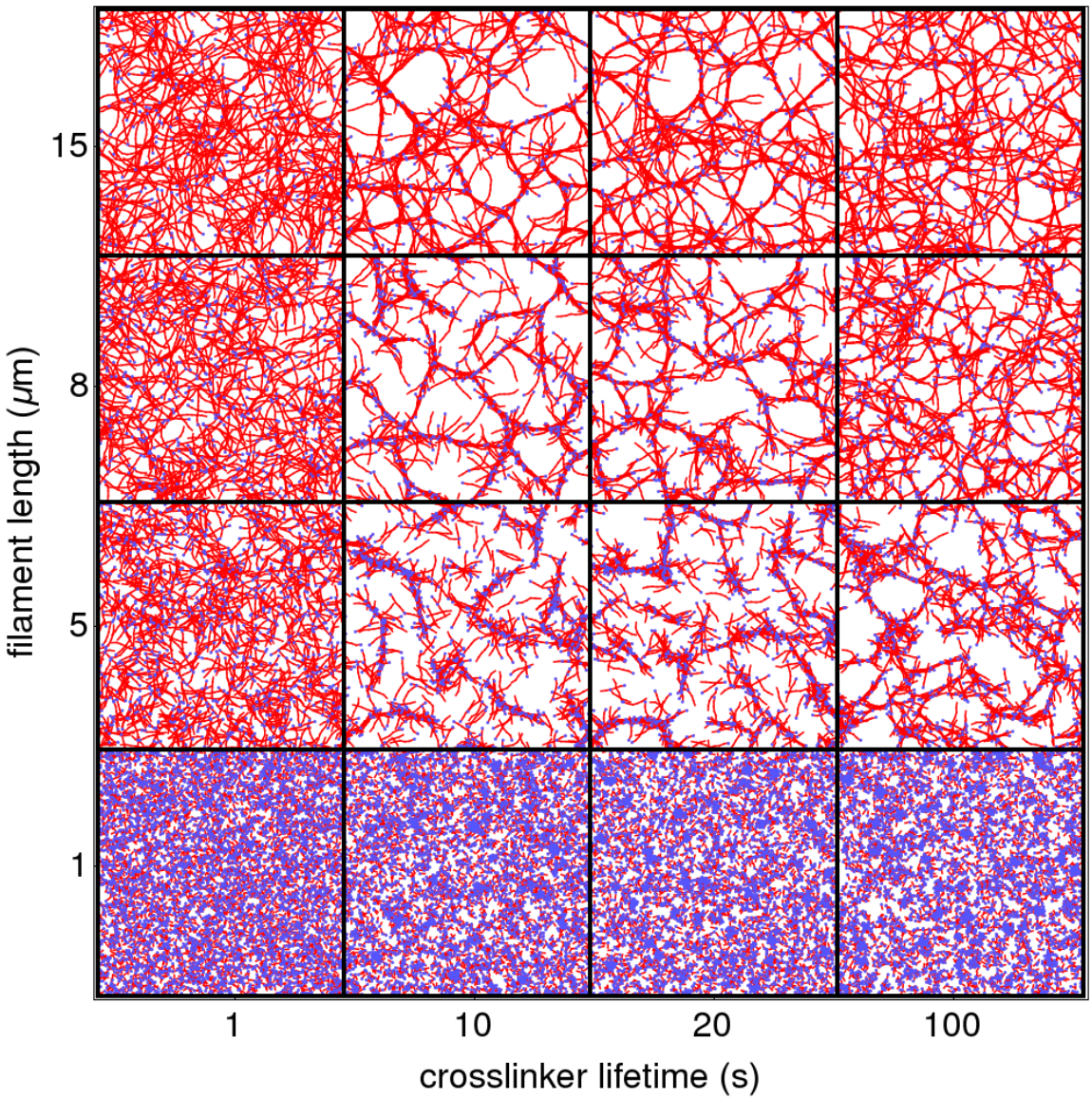

Figure 3.14: Sample structures after 400 s simulation, for varying filament length and crosslinker off rate. Parameters held constant: $\rho_m = 0$, $\rho_{xl} = 1.5\ \mu\text{m}^{-2}$. Motors, crosslinkers, and barbed ends not shown for clarity.

3.4.2 Simulating shear

To measure the stiffness of self-assembled actin networks, we simulate a controlled strain experiment and shear the final network configuration by a total strain of $\gamma = 0.5$ in a fixed amount of time $t_F = 0.5$ s. This is accomplished by supplementing the Brownian dynamics described in Chapter 2 explicitly shifting the actin bead position (x_i, y_i) such that $x_i \rightarrow x_i + \gamma(dt/t_F)(y_i/Y)$ where Y is the simulation cell height, and dt is the amount of time for a small shear [37]. Additionally, the boundary conditions follow the Lees-Edwards convention during the shear [90]. As described in [44], we do not perform this shift at every time step; rather $dt = \Delta t + t_{relax}$ where Δt is the simulation time step and t_{relax} is a suitable amount of time for the simulation to relax from the large external force imposed by the shear. In Fig. 3.2F, we used $\Delta t = 10^{-7}$ s and $dt = 10^{-3}$ s.

The viscoelastic response of a network undergoing simple shear is typically measured by computing the stress σ on the network as a function of the strain γ. In general, this response is frequency dependent, such that if the system is sheared sinusoidally, with a frequency of ω, then the expected stress response is

$$\sigma = G'(\omega)\gamma + G''(\omega)\dot{\gamma}/\omega \tag{3.5}$$

where $G'(\omega)$ is the storage modulus, $G''(\omega)$ is the loss modulus, and $\dot{\gamma}$ is the strain rate. At long times, or for a constant strain ($\omega \rightarrow 0$), $G'(\omega)$ is the shear modulus of the material, and $G''(\omega)/\omega$ is its dynamic viscosity. Additionally, because for 2D networks the stress is not well defined, we instead measure the energy density $w(\gamma)$, as it satisfies the equation $dw/d\gamma = \sigma$. Integrating Eq. 3.5 with respect to γ and substituting the constant-strain approximation, we obtain our model $w(\gamma) = 1/2G\gamma^2 + \eta\dot{\gamma}\gamma + w(0)$ [13].

CHAPTER 4

FILAMENT RIGIDITY AND CONNECTIVITY TUNE THE DEFORMATION MODES OF ACTIVE BIOPOLYMER NETWORKS

This chapter was originally published as Ref. 159 and is coauthored with Samantha Stam, Shiladitya Banerjee, Kim Weirich, Aaron Dinner, and Margaret Gardel. While Samantha Stam deserves the most credit for this work, my contributions include running all the simulations, and producing Fig. 4.3C-D, Fig. 4.4, Fig. 4.5B-C, and Fig. 4.12. I also aided significantly (along with all coauthors) in the writing, particularly the sections describing the simulation results and methods.

Molecular motors embedded within collections of actin and microtubule filaments underlie the dynamics of cytoskeletal assemblies. Understanding the physics of such motor-filament materials is critical to developing a physical model of the cytoskeleton and designing biomimetic active materials. Here, we demonstrate through experiments and simulations that the rigidity and connectivity of filaments in active biopolymer networks regulates the anisotropy and the length scale of the underlying deformations, yielding materials with variable contractility. We find that semi-flexible filaments can be compressed and bent by motor stresses, yielding materials that undergo predominantly biaxial deformations. By contrast, rigid filament bundles slide without bending under motor stress, yielding materials that undergo predominantly uniaxial deformations. Networks dominated by biaxial deformations are robustly contractile over a wide range of connectivities, while networks dominated by uniaxial deformations can be tuned from extensile to contractile through cross-linking. These results identify physical parameters that control the forces generated within motor-filament arrays, and provide insight into the self-organization and mechanics of cytoskeletal assemblies.

4.1 Introduction

Assemblies of semiflexible filaments and molecular motors are active materials [108] that drive many physiological processes such as muscle contraction [52], cytokinesis [39], cytoplasmic transport [118], and chromosome segregation [49]. To actuate these processes, the nanometer-scale displacements of motors and local deformation and sliding of filaments must give rise to coordinated mesoscale deformations. These mesoscale dynamics result in the transmission of cellular-scale forces with different directions (e.g., contractile or extensile) and shapes (e.g., isotropic or anisotropic) which result in shape changes at cellular and tissue length scales. Characterizing deformations in active networks of different molecular compositions is a much needed step toward understanding complex force transmission and shape changes observed in cells and tissues.

Understanding how assemblies of filaments and motors produce a net contractile or extensile force has been extensively explored theoretically [10, 50, 102, 87, 29, 103, 95, 6, 142]. Testing these models experimentally has been challenging due to variability in protein composition from one preparation to another and limitations in the ability to systematically alter physical properties. In vitro networks constructed from actin filaments and myosin II motors are robustly contractile [76, 2, 123, 81]. By contrast, systems of microtubules and molecular motors are either extensile [10, 50, 146, 66, 160] or contractile [160, 43, 167]. One difference between these two active materials is that microtubules are significantly more rigid than actin filaments. Recent work has shown that contractile stress can be generated via motor stress-induced filament buckling [103, 95, 6, 142, 123], indicating an important role for filament rigidity. Alternative microscopic mechanisms to generate extensile or contractile stress by motor-mediated sliding of rigid filaments have also been proposed [10, 50, 102, 87, 29, 6, 160].

Deformations within active matter can be characterized beyond whether they are contractile or extensile. For example, network-scale force transmission is affected by network connectivity, which regulates the length scale of contraction [76, 2, 7, 177, 35]. Moreover, recent data suggests that disordered actomyosin networks contract isotropically, suggesting

the shape of the deformation is important [101, 153]. By contrast, in vivo, anisotropic contraction dominates cell division and muscle contraction [121]. Understanding how to control the deformation anisotropy will further our understanding of how contractile deformations are regulated in vivo.

Here, we directly vary the stiffness and connectivity of filaments within an in vitro biopolymer network through cross-linking and investigate the effects on network deformation. Through quantitative analysis of experimental data, we determine that these mechanical changes influence the anisotropy and contractility of deformations caused by the motor protein myosin II. Networks composed of semi-flexible filaments that can be buckled by motor stresses exhibit robust biaxial contraction. Increasing the filament rigidity results in uniaxial deformation, the contractility of which is regulated by cross-linker density. Extensile deformations are generated at low cross-linker density and contractile deformations occur at high cross-linker density. Using corresponding agent-based simulations, we identify the microscopic deformation modes driving these mesoscale rearrangements. In particular, we find that contractile forces in networks of rigid filaments are transmitted uniaxially by filament sliding. Together, our results indicate how motor-filament interactions can generate forces that result in either extensile or contractile deformations, which vary in shape depending on the filament rigidity and connectivity. From our experimental and simulation data, we propose a phase diagram of active matter constructed from motors and filaments.

4.2 Results

4.2.1 Networks of cross-linked rigid bundles are contractile with a short correlation length

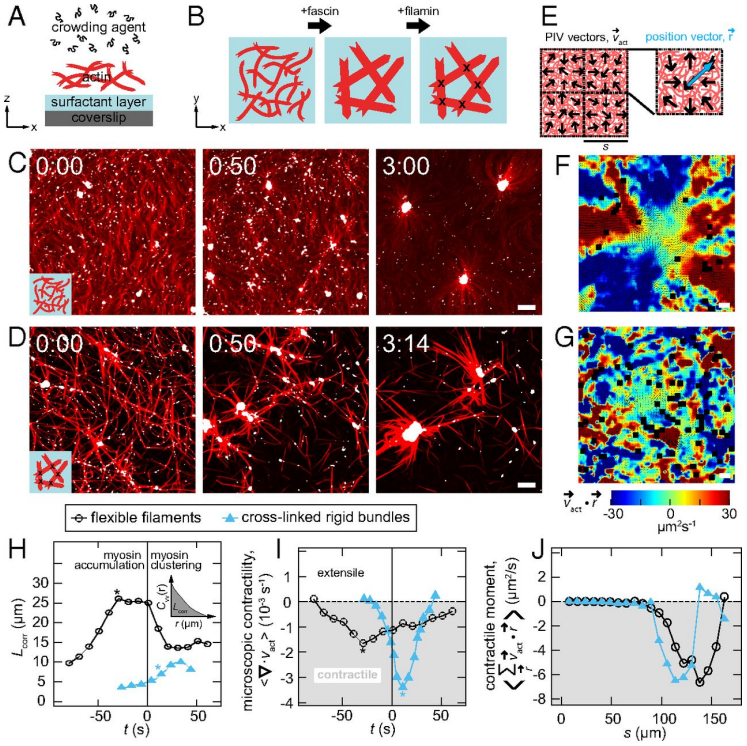

Figure 4.1: Networks of rigid bundles are contractile with a short correlation length (A) Schematic of experimental setup. Actin filaments are crowded to a surfactant-coated coverslip surface to make a dense quasi-2D layer. (B) Fascin is used to make rigid, unipolar actin bundles. Filamin is used to cross-link bundles. (C) Images of semi-flexible filaments (red) in the absence of fascin or filamin after the addition of myosin (white puncta). (D) Images of cross-linked rigid bundles formed by F-actin in the presence of fascin (1:10) and filamin (1:500) after myosin is added. (E) Particle Imaging Velocimetry (PIV) detects local motion of F-actin ($\vec{v}_{act}$, black arrows). Images are split into boxes of size s, and $\vec{r}$ defines a vector from the center of a box to a PIV vector within the box. (F-G) Example spatial maps of the moment of the velocity field for images at -0:40 and 0:00 of panels C & D, respectively. Negative values of $\vec{v}_{act} \cdot \vec{r}$ indicate contractile whereas positive values indicate extension. (H) The correlation length as a function of time for single filaments (open black circles) and cross-linked rigid bundles (closed blue triangles). Inset: Schematic indicating how correlation length is obtained from velocity-velocity correlation. (I) The divergence for both networks as a function of time. The asterisks in H+I indicate the time of minimal divergence, as indicated in (I). (J) The contractile moment as a function of length scale s for both samples. For (C)-(G), scale bars are 10 m. Time stamps are in the minutes:seconds format where 0:00 indicates the time of the maximal myosin puncta density after the initial increase when myosin is added to the sample and prior to the decrease due to myosin clustering in Fig. 4.9A.

To investigate the role of filament rigidity in active motor-filament networks, we construct a quasi-two-dimensional (quasi-2D) layer of actin in vitro by polymerization of 1 μM monomeric actin in the presence of a depletion agent to crowd actin filaments near a passivated surface (Fig. 4.1A) [123, 146]. To increase filament rigidity, we add 0.1 μM of the actin cross-linker fascin, which constructs bundles of 8 7 actin filaments (Supplemental Fig. 4.8). Actin filaments are polar, and their barbed ends are uniformly directed within fascin bundles [74]. Fascin bundles, then, maintain the polarity of single actin filaments but are much more rigid (Fig. 4.1B): the persistence length of bundles is estimated to be 250 m [25], over 10 times that of a single actin filament [55]. Although actin bundling could also affect the interactions between actin and myosin, the myosin filaments in our experiments move along the fascin bundles unidirectionally with an average velocity of 2.5 m/s (Methods), which is close to the unloaded gliding speed of skeletal muscle myosin II [156, 85]. To connect rigid bundles into networks, we add a small amount (0.002 μM) of a second cross-linker, filamin. Filamin is a large (200 nm) and flexible cross-linker that binds overlapping bundles with varying orientations into a quasi-2D network [63, 64].

After assembling actin filaments or bundles, we add myosin II and monitor structural changes in the actin networks via fluorescence microscopy (Methods). Myosin II filaments (white spots) initially accumulate on the networks, and we define the time of the maximum density of myosin puncta as $t = 0$ s (Supplemental Fig. 4.9). Myosin drives changes in actin filament or bundle orientation, position, and shape that ultimately result in the formation of actomyosin asters comprised of polarity-sorted actin filaments oriented radially with large myosin foci at the center (Fig. 4.1C-D, Supplemental Fig. 4.9).

To assess the network motion leading to aster formation, we calculate local displacement vectors of the actin network between frames using particle image velocimetry (PIV) (Fig. 4.1E, Methods). To visualize propagation of contractile or extensile motion, we calculate the moment of the velocity field, $\vec{v}_{act}(\vec{r}) \cdot \vec{r}$, where $\vec{v}_{act}(\vec{r})$ is the local actin PIV vector and $\vec{r}$ is the vector from the center of a square region to the location of the PIV vector [20]

(Fig. 4.1E). Locations where the moment is positive indicate local expansion from the center of the field of view whereas negative values indicate local compression. During the early stages of network reorganization before aster formation, we find that spatial propagation of inwardly or outwardly directed motion is very different in networks of semi-flexible filaments and those of cross-linked rigid bundles (Figs. 1F and 1G). In networks of semi-flexible filaments, motion is highly spatially correlated, with large areas contracting toward the center of the square region in the vertical direction (blue, Fig. 4.1F) and material moving outward in the horizontal direction (red, Fig. 4.1F). In contrast, in the bundled network, motion is restricted to smaller, irregularly shaped, interspersed contractile and extensile regions (Fig. 4.1G).

To characterize the length scale of correlations in the velocity field, we consider the velocity-velocity correlation function:

$$C_{vv}(r) = \frac{\langle \vec{v}_{act}(0) \cdot \vec{v}_{act}(r) \rangle}{\langle |\vec{v}_{act}(0)|^2 \rangle} \tag{4.1}$$

where r is the distance between two velocity vectors $\vec{v}_{act}$. We define a characteristic correlation length, L_{corr}, as the area under the curve of $C_{vv}(r)$ at a given time (inset, Fig. 4.1H). In both networks, L_{corr} initially increases as myosin forces accumulate in the network (Fig. 4.1H). Eventually, L_{corr} decreases as the networks break into clusters. Although L_{corr} has similar trends for both networks, its value is consistently less for the rigid bundle network than for the network of semi-flexible filaments. This is consistent with the spatial heterogeneity in the moment of the velocity field observed in the network of rigid bundles, as compared to that formed with semi-flexible filaments (Figs. 1F and 1G).

Next, we assess net contractility using two different measures. The divergence of $\vec{v}_{act}$, $\nabla \cdot \vec{v}_{act}$, is a measure of contractility on the length scale set by the spacing of PIV vectors, in this case 2.4 m [120]. Negative values indicate local contraction while positive values indicate local expansion. For networks of semi-flexible filaments, the spatial average of $\nabla \cdot \vec{v}_{act}$ is

negative (Fig 1I, open black circles), indicating net contraction, consistent with previous reports [120]. The divergence reaches a maximally negative value as myosin accumulates on the network before separation of actin into clusters, at which point local extension between clusters balances contractility to produce $\langle \nabla \cdot \vec{v}_{act} \rangle \sim 0$ s^{-1}. Similarly, the cross-linked rigid bundle network exhibits a negative divergence that returns to values near 0 s^{-}1 after the onset of network coarsening at 0 s (Fig. 4.1I, filled blue triangles). Thus, the contractility is slightly enhanced in networks of rigid bundles as compared to those of semi-flexible filaments.

To characterize the length scale of contraction, we measure the contractile moment by summing $\vec{v}_{act}(\vec{r}) \cdot \vec{r}$ [20] over non-overlapping square regions of varying side length s (Fig. 4.1J). Negative values of the contractile moment indicate that contractile motion propagates across regions with this length scale [20]. In both networks, $\langle \sum_{\vec{r}} \vec{v}_{act}(\vec{r}) \cdot \vec{r} \rangle$ reaches a minimum for regions of length 100 μm $< s <$ 150 μm. Thus, contraction in both materials can propagate over large length scales. However, the collective motions in the rigid networks consistently occur over shorter length and time scales.

4.2.2 Rigidity controls the anisotropy of contractile deformations

To explore the origin of differing spatial distribution of motion within these contractile networks, we sought to characterize the local deformations. We apply a method previously used to characterize the anisotropy of forces exerted by cells [20]. We consider the tensor

$$M_{ij} = \sum_{\vec{r}} v_{act}(\vec{r})_i r_j \tag{4.2}$$

where i and j denote the in-plane spatial coordinates. By diagonalizing this tensor, we can extract the principle deformation axes. The magnitudes of the eigenvalues, M_{max} and M_{min}, are the major and minor axes, respectively, of an ellipse characterizing the anisotropy of the deformation (Fig. 4.2A). A value of M_{min}/M_{max} of 0 indicates a completely uniaxial deformation, while a value of $M_{min}/M_{max} = 1$ indicates a completely biaxial deformation

(Fig. 4.2A). For a given length scale (s = 20 m), a distribution of M_{min}/M_{max} from deformations across the field of view is obtained at each time point (Fig. 4.2B, Fig. 4.2C). In networks of semi-flexible filaments, the distribution is clearly weighted towards biaxial deformations ($M_{min}/M_{max} > 0.5$) at all times during contraction (Fig. 4.2D). By contrast, in cross-linked rigid bundle networks, the distribution is highly weighted towards uniaxial deformations ($M_{min}/M_{max} < 0.5$) at all times (Fig. 4.2E). We find that these characteristic differences in deformation anisotropy between rigid and semi-flexible networks persist across length scales varying from $s = 6$ m up to 60 m (Fig. 4.10).

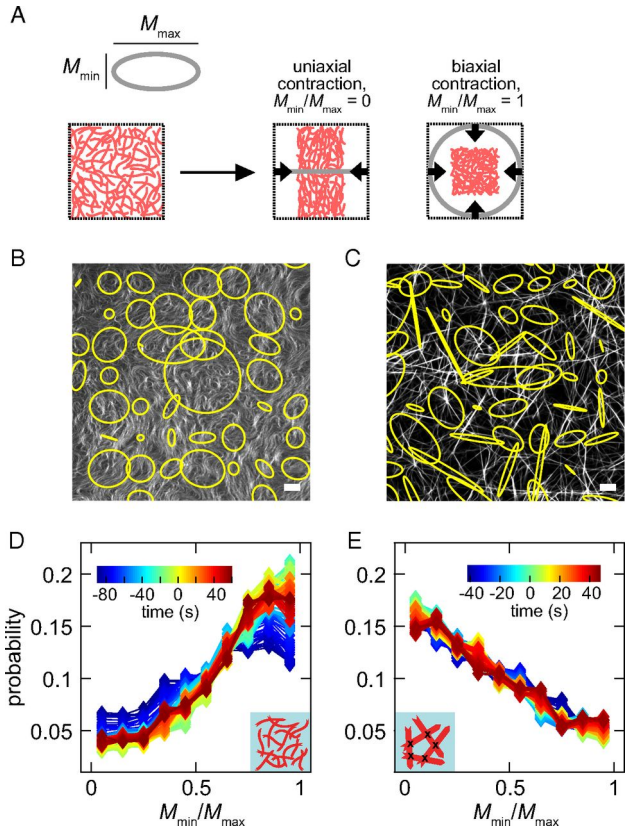

Figure 4.2: Deformations are highly biaxial and uniaxial in networks of semi-flexible filaments and rigid bundles respectively (A) The eigenvalues of the flow dipole moment tensor, M_{min} and M_{max}, are the axes of an ellipse that characterizes the deformation anisotropy, with uniaxial and biaxial contraction illustrated. (B) and (C) Images of deformation anisotropy in networks of semi-flexible filaments (B) and rigid bundles (C). (D) and (E) Distribution of M_{min}/M_{max} at varying times (color scale) at $s = 20$ m for semi-flexible filaments (D) and cross-linked rigid bundles (E). Normalization is such that the 10 points (diamonds) defining each curve sum to 1.

To examine the effect of different deformations on correlated motion and contraction, we next consider the change in the fraction of predominately biaxial ($M_{min}/M_{max} > 0.5$) or uniaxial ($M_{min}/M_{max} < 0.5$) deformations and term these $P_{biaxial}(s)$ and $P_{uniaxial}(s) = 1P_{biaxial}(s)$, respectively (Fig. 4.11). We compare these quantities to the correlation length, Lcorr, and the microscopic contractility as a function of time. Versions of these quantities that are rescaled to range from 0 to 1 are indicated by lower case letters, e.g., $p_{biaxial}(s)$ and l_{corr} (see Methods). For both rigidities, either $p_{biaxial}(s)$ or $p_{uniaxial}(s)$ is positively correlated with l_{corr} and is optimized for a given length scale s (Methods, Fig. 4.11). In networks of semi-flexible filaments, $p_{biaxial}$ is positively correlated with l_{corr} during network contraction (Fig. 4.3A). In contrast, for the cross-linked rigid bundle networks, puniaxial is strongly positively correlated with l_{corr} (Fig. 4.3B and Fig. 4.11B).

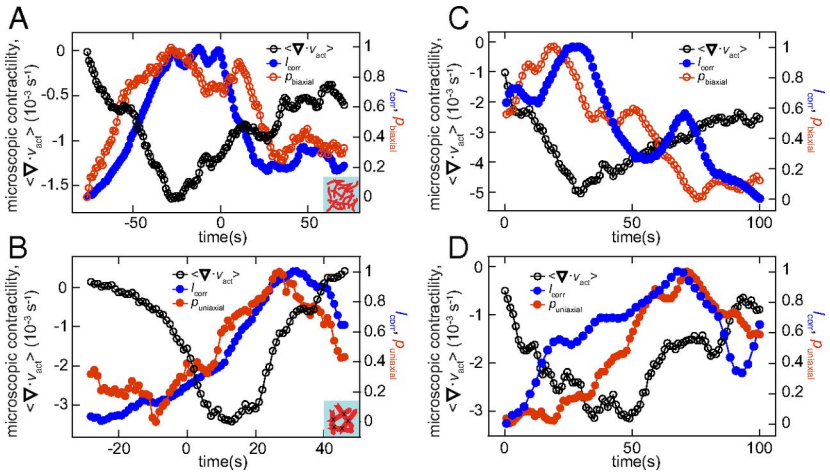

Figure 4.3: Activation of biaxial or uniaxial deformations in semi-flexible filament and rigid bundle networks respectively coincides with correlated motion and contractility. Plot of the divergence (open black circles), correlation length (filled blue circles) and either biaxial probability (A, filled red circles) or uniaxial probability (B, filled red circles) as a function of time for single filaments (A) and cross-linked rigid bundles (B). The length scale chosen to calculate biaxial or uniaxial probability is determined to be the optimal one, as shown in Fig. 4.11 and is s $= 25 - 30$ m in (A) and $55 - 60$ m in (B). (C-D) Analogs of (A) and (B) for simulated networks. In (C) $L_p = 2.5$ m and in (D) $L_p = 250$ m. The length scale for both biaxial and uniaxial probabilities is $s = 20$ m. In the experimental data of (A) and (B), $t = 0$ s indicates the time of maximal myosin puncta density after the initial increase when myosin is added to the sample and prior to the decrease due to myosin clustering in Fig S2A. In the simulations of (C) and (D), $t = 0$ s also indicates the time of maximal myosin puncta density, which in this case occurs immediately at the beginning of the simulation.

These data demonstrate that contractility can occur in networks composed of either semi-flexible or rigid filaments, consistent with previous reports of contractility in various cross-linked biopolymer networks [76, 2, 123, 81, 160]. Our analysis reveals significant differences, however, in the mesoscale shape changes induced within the two networks, with compliant networks supporting biaxial contraction and rigid networks supporting uniaxial deformations.

To determine whether a change in filament stiffness is sufficient to cause an alteration of deformation anisotropy, we use agent-based simulations [44] (Chapter 2). In brief, we model actin filaments as worm-like chains and model cross-linkers and motors as linear springs with two sites (heads) that can attach and detach to the filaments via a Monte Carlo procedure. When attached, motor heads walk toward filament barbed ends at a load-dependent speed. We use Langevin dynamics to evolve each mechanical component of the assembly in response

to internal forces. When parameterized as detailed in [44], this model captures a variety of experimentally observed trends with reasonable quantitative accuracy. We implicitly model bundling, corresponding to experimental fascin-bundled actin, by varying the persistence length of the actin filament (L_p). We explicitly model cross-linking, corresponding to the experimental cross-linker filamin, by a spring with rest length 0.15 m and stiffness 1 pN/m [64]. Myosin minifilaments are modeled similarly, as springs with rest length 0.5 m, unloaded speed $v_0 = 1$ m/s, and stall force 10 pN.

Consistent with experiments, we observe that motors (white rectangles) move actin filaments and rearrange the filaments into asters (Fig. 4.4A, Fig. 4.4B).The microscopic contractility, $\nabla \cdot \vec{v}_{act}$, decreases to negative values and subsequently increases as the networks form asters and contraction stops (Fig. 4.3C and Fig. 4.3D, black circles). The trends in $P_{biaxial}$ (Fig. 4.3C, red circles, Supplemental Fig. 4.12A), $P_{uniaxial}$ (Fig. 4.3D, red circles, Supplemental Fig. 4.12B), and l_{corr} (Fig. 4.3C and Fig. 4.3D, blue circles) are similar to the experimental results as well, but somewhat noisier. The quantitative differences between the computational and experimental results likely derive from the fact that the size of the simulation region necessitates a smaller value of L_p in the simulation ($L_p = 2.5$ m, compared with $L_p = 17$ m for actin) and s in the computational analysis ($s = 20$ m, compared with $s = 25 - 30$ m in Fig. 4.3A and $55 - 60$ m in Fig. 4.3B).

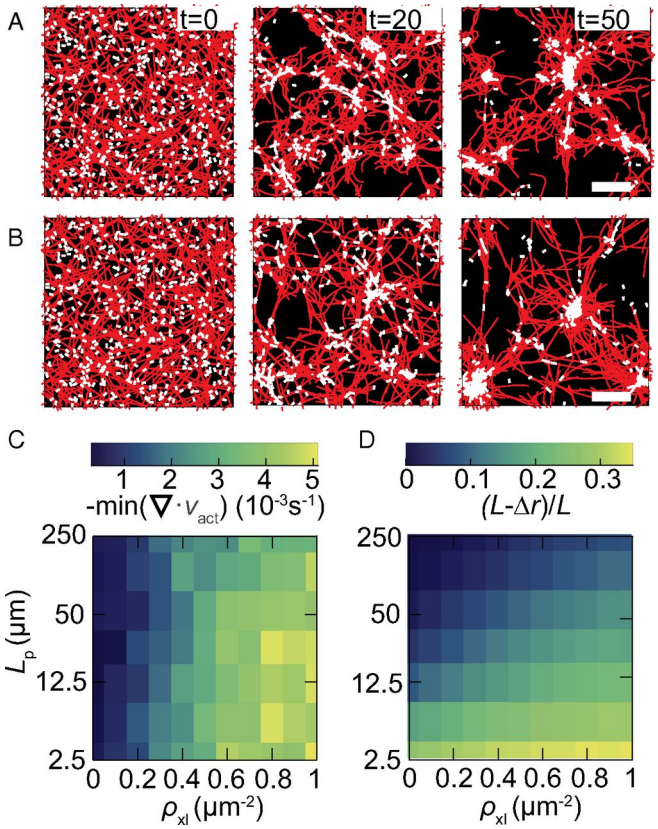

Figure 4.4: Simulations indicate cross-link dependent contractility over a wide range of filament stiffness (A) and (B) Time series images in simulations for network with lower filament stiffness (L_p = 25 m, (A)) and higher filament stiffness (L_p = 250 m, (B)). Actin is shown in red and myosin is white. Scale bars are 10 m. (C) Microscopic contractility at varying filament stiffness and cross-linker density. This is measured by the minimum of the spatially averaged divergence of the actin velocity field weighted by the local actin density in the first 25 s of simulation. (D) Filament compression during the first 25 s of simulation as a function of stiffness and cross-linker density.

4.2.3 Uniaxial contraction arises from filament sliding arrested by cross-linker accumulation

We perform simulations over a range of filament rigidities (2.5 m 250 m) and cross-linker densities (01 m^{-2}). These simulations reveal that microscopic contractility is generally more sensitive to changes in cross-linker density than filament rigidity (Fig. 4.4C). This result is surprising, as we previously identified filament buckling as the microscopic mechanism underlying contractility in networks of semi-flexible actomyosin [123]. To check whether this

mechanism is operative in the simulations, we quantify filament compression, $(L - \Delta r)L$, where L is the filament contour length and Δr is the end-to-end distance. This measure is zero when filaments are perfectly straight ($r = L$) and greater than zero if they are bent. As expected, buckling is prevalent at low filament rigidity (Fig. 4.4D). Here, we note that the shift to increasingly biaxial deformations in the experimental distribution of Mmin/Mmax (Supplemental Fig. 4.10A) occurs concurrently with the development of visible buckling and bending in filaments, indicating that buckling is the underlying cause of biaxial contraction. This shift does not happen in the network of cross-linked rigid bundles, presumably because buckling is suppressed by the increased filament rigidity. Consistent with this observation, there is a sizable region of the simulation parameter space over which contractility occurs in the absence of filament compression (Figs. 4C and 4D).

An alternate microscopic mechanism that could account for the contractility at higher rigidities is myosin-driven actin sliding [10, 102, 87, 6, 160]. Actin sliding drives local contraction when a motor connected to two antiparallel filaments is closer to their pointed ends, and local extension when it is closer to their barbed ends (Fig. 4.5A). In the absence of symmetry-breaking mechanisms, this results in no net force propagation as extensile and contractile deformations balance. However, when filaments overlap, there are more sites for cross-linkers to bind bivalently. This suppresses extensile motions that propagate force into the surrounding network [10, 160].

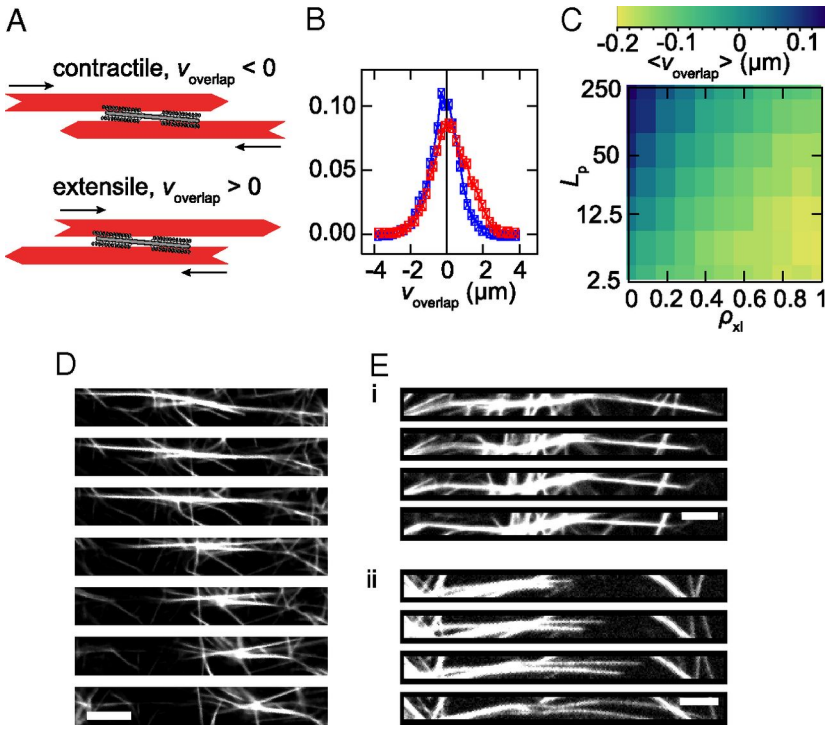

Figure 4.5: Uniaxial contractility is caused by arrested filament sliding (A) A pair of antiparallel filaments are contractile if the myosin is near the pointed ends (top) and extensile is myosin is proximal to the barbed ends (bottom). (B) The distribution of voverlap is shifted to more extensile values for rigid ($L_p = 250$ m) filaments without cross-linking (red squares) compared to the same filaments with $\rho_{xl} = 1\mu\text{m}^{-2}$ (blue squares). This distribution is from the first 10 s of simulation. (C) Average of $v_{overlap}$ over 25 s of simulation with varying filament rigidity and cross-linker density. (D) In experiments with cross-linked rigid bundles, the bundles are observed to slide together and become arrested in the contracted state. The time delay between images from top to bottom is 1 s (E) In the absence of filamin, myosin drives both contractile (i) and extensile (ii) motions of rigid bundle pairs. The time delay between frames from top to bottom in both (i) and (ii) is 1 s. Scale bars are 5 m in (D) and (E).

We examine the probability distribution of relative sliding velocity, $v_{overlap}$, in simulations of rigid ($L_p = 250$ μm) filaments both with ($\rho_{xl} = 1m^{-2}$) and without cross-linkers. The distribution of overlap velocities shifts to negative values with the addition of cross-linkers (Fig. 4.5B). By examining the relative sliding velocity across all parameter values, we observe that the system is contractile ($\langle v_{overlap} \rangle < 0$) over most rigidities and cross-linker densities (Fig. 4.5C). However, at the lowest cross-linker densities and highest filament rigidities, we observe a regime where $\langle v_{overlap} \rangle > 0$, indicating that extensile motions dominate,

consistent with theory [10, 50, 160].

To seek experimental evidence for extensile sliding, we examined pairs of bundles undergoing relative sliding. Indeed, in the presence of cross-links between bundles (1:500 filamin:actin) we observe bundle pairs sliding relative to each other, increasing the overlap, and then stopping (Fig. 4.5D). In a network without cross-links between rigid bundles, we see both bundles that increase their overlap (Fig. 4.5E(i)) and that extend further apart (Fig. 4.5E(ii)). The latter is similar to extensile motions observed in active liquid crystals of microtubules and kinesin [66], but leads to the formation of asters [124, 169]. Thus, our simulations and experiments of rigid filament suggests that cross-linker density can control the transition from contractile to extensile deformations, consistent with recent publications [10, 160, 35].

4.2.4 Motors drive aster formation within rigid bundles without cross-links via uniaxial, extensile forces

To understand the consequences of the microscopic extensile deformations described above, we study the myosin-driven reorganization of rigid actin bundles that lack filamin cross-linkers but are sufficiently dense to have numerous overlaps such that myosin motors can slide and rearrange bundles to eventually form asters (Fig. 4.6A).Asters are comprised of a dense myosin cluster with polarity sorted actin bundles emanating from the center, similar to those previously described (Fig. 4.9A and Fig. 4.6A). The spatial map of the moment of the velocity field reveals small, interspersed, contractile and extensile regions (Fig. 4.6B) with short velocity-velocity correlation lengths (Fig. 4.13). Consistent with simulations (Fig. 4.5C), the divergence of the velocity field indicates net extensile deformation (Fig. 4.6C) and the contractile moment is weakly positive at 100 m (Fig. 4.6D). Although the minimum divergence of the velocity field is weakly negative if the PIV vectors are calculated at sufficiently large time delays and length scales, the divergence values are always less negative than in the other two networks (Fig. 4.14). Consistent with motions dominated by filament sliding, deforma-

tions are predominantly uniaxial (Figs. 6E, Fig. 4.10C).Thus, actin sliding is responsible for short-range extensile, uniaxial deformations that drive local rearrangement of actin bundles into polarity-sorted asters.

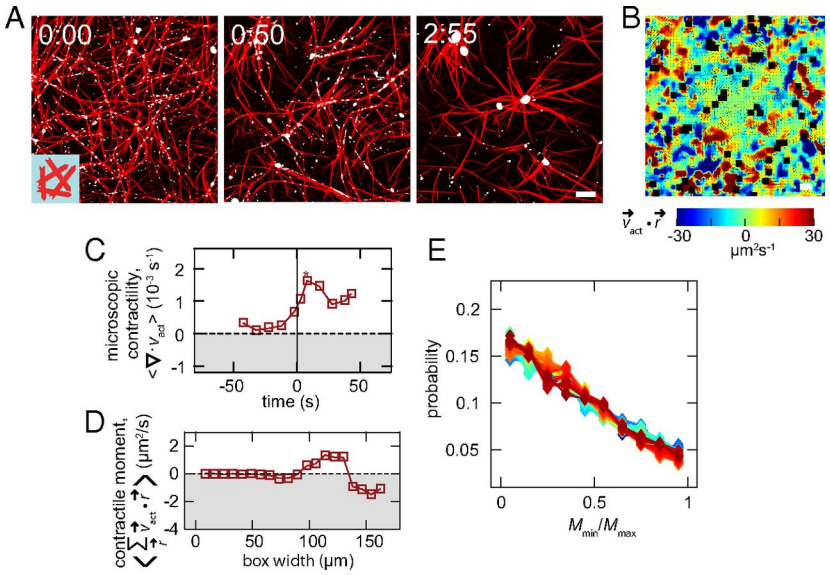

Figure 4.6: Myosin re-organizes rigid bundles lacking filamin cross-links via uniaxial forces. (A) Image sequence of fascin bundles without filamin. Actin is shown in red and myosin in white. (B) Values of $\vec{v}_{act} \cdot \vec{r}$ over a 150 m x 150 m square region. (C) The divergence of $\vec{v}_{act}$ is non-contractile over the course of network rearrangement. (D) The contractile moment, $\langle \sum_{\vec{r}} \vec{v}_{act}(\vec{r}) \cdot \vec{r} \rangle$, calculated over a 30 s interval after the maximum divergence in (C). (E) Distribution of M_{min}/M_{max}, $s = 20$ m, indicates that deformations are predominantly uniaxial.

4.3 Discussion

Our work demonstrates how local shape deformations within active biopolymer networks can be altered by modifications to filament rigidity and cross-link density. Changes to these biophysical parameters alter the microscopic mechanisms of active stress and subsequent structural rearrangements. Using this information, we map three phases of deformations that are characterized by their anisotropy, length scale, and contractility. The different phases are elicited by modifying filament rigidity and connectivity (Fig. 4.7). Each phase is consistent with network conditions favoring one of three microscopic deformation modes:

filament buckling, filament sliding, or arrested filament sliding. We show that buckling results in predominately biaxial deformation modes whereas sliding results in predominately uniaxial deformation modes. These results have implications for how the various physical properties of cytoskeletal networks support different deformations, and how cells or tissue change shape when the resulting forces are propagated to larger length scales. Such control over the shape of the deformations could be used to sculpt active materials both in vitro and in vivo.

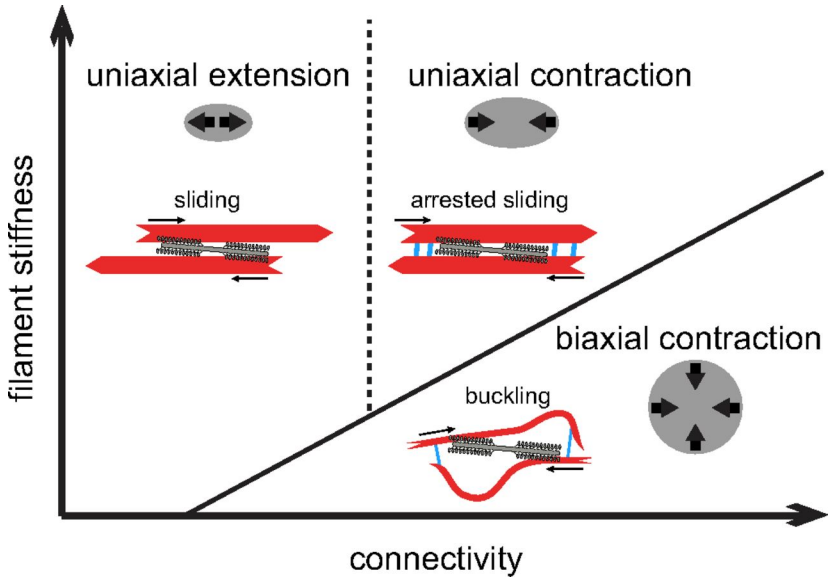

Figure 4.7: Uniaxial and biaxial deformations indicate differences in the mechanism of contractility and force propagation. Starting from the top left of the diagram, the three states we observe are extensile sliding, contractile sliding, and contractile buckling. The shape of the boundaries between these mechanisms are based on the simulation phase diagrams in Fig. 4.4D and Fig. 4.5C. The mechanisms can be identified by the characteristic anisotropy of the transmitted forces, which is predominantly uniaxial for sliding and biaxial for buckling.

We are now in a position to formulate a framework (Fig. 4.7) that can unify previous observations of both extensile and contractile behaviors in active microtubule systems [10, 50, 146, 66, 160, 43, 167] with the robust contractility typically observed in actin networks [76, 2, 123, 81]. Motor-induced filament buckling drives contractility when motor-stresses exceed the Euler buckling force of filaments [103, 95, 6, 123]. For a constant motor density, we expect increased connectivity to enable higher stresses [35, 93], while increased rigidity

raises the force required for buckling (Fig. 4.7, solid black line). When buckling is suppressed, motor-mediated sliding of antiparallel filaments becomes the dominant deformation mode. In this phase, cross-linker density qualitatively changes the motor-mediated deformations of rigid filaments from extensile to contractile (Fig. 4.7, dashed line). When cross-linkers are absent, enhanced motor binding for highly overlapping filaments favors the generation of extensile stresses [10, 50]. When crosslinkers are present, they can bind to highly overlapping filaments and attenuate extensional stresses [10, 160]. In future work, it will be interesting to explore the transitions between other microscopic deformation modes in active motor-filament systems and see how these are controlled by changes or heterogeneity in the local structure and composition (e.g., filament orientation or polarity organization).

We note that many previous studies [76, 2, 123, 81, 43, 167, 7, 124, 169, 83, 33, 4, 175] have equated the formation of asters in actomyosin networks with contractility. Associated theoretical models have assumed that motors always produce contractile force dipoles [77]. However, our analysis shows that similar structures can result from isotropic and anisotropic contractility, as well as anisotropic extension. This underscores the importance of characterizing dynamics rather than relying on final structures alone to elucidate physical mechanisms.

Finally, our analysis strategies may be used for assessing and understanding the underlying physical mechanisms of force propagation in a variety of active biopolymer systems. We modify previous metrics [20] to detect propagation of contraction or extension across varying length scales. We also determine which deformations (biaxial or uniaxial) are responsible for correlated motion. Similar techniques could be used to understand the deformations of motor-filament arrays in the actin and microtubule cytoskeletons during processes including cell migration, cell division, intracellular transport, and formation of the mitotic spindle. Beyond the cytoskeleton, intranuclear molecular motors can drive correlated motion of chromatin [187], and forces produced by whole bacterial or mammalian cells can drive motions such as biofilm contraction or growth [185, 3] or alignment and organization of filamentous extracellular matrices [61, 170, 21]. The physical properties of deformations that occur during

these processes and the mechanisms at the level of biopolymer deformation or translocation have not been explored. Investigations of this nature will reveal which features of active matter dynamics are fundamental across these highly diverse systems and which features are regulated by particular biopolymer and motor network properties.

4.4 SI Materials and Methods

4.4.1 Protein Purification

Actin was purified from rabbit acetone powder (Pel-Freez Biologicals) with a protocol derived from ref. 54 and stored as a monomer in G-buffer (2 mM TrisHCl, pH 8.0, 0.2 mM ATP, 0.2 mM CaCl2, 0.2 mM DTT, and 0.005Fluorescent labeling of actin was done with a tetramethylrhodamine-6- maleimide dye (Life Technologies). Skeletal muscle myosin II was purified from chicken breast [109] and labeled with Alexa- 642 maleimide (Life Technologies) [174]. Filamin was purified from chicken gizzard [27]. Fascin was purified using a GST-tagged construct (ref. 58 and Dave Kovar laboratory, University of Chicago, Chicago). Purification was done using a glutathione Sepharose column (GE Healthcare Life Sciences). The GST tag was then cleaved with thrombin (GST Healthcare Life Sciences) and separated by chromatography (Hi-Trap Q column; GE Healthcare Life Sciences).

4.4.2 Microscopy Sample Preparation

The coverslip surface was passivated against nonspecific adhesion of protein with a surfactant layer, either a lipid bilayer [179] or a fluorinated oil-surfactant layer [146]. To prepare a lipid bilayer, coverslips (no. 1.5; Fish- erbrand) were rinsed with water and ethanol then exposed to UV- ozone for 20 min. The sample chamber was assembled by an- choring a glass cylinder (3166-10; Corning Life Sciences) to the coverslip with vacuum grease. This was filled with vesicle buffer (10 mM phosphate buffer, pH 7.5, and 140 mM sodium chloride) and DOPC vesicles (1,2-dioleoyl-sn-glycero-3-phosphocholine; Avanti Polar Lipids) were added

to a concentration of 100 M and incubated for 15 min to allow bilayer formation. To prepare the oil-surfactant surface, PFPE-PEG-PFPE surfactant (008; RAN Biotechnologies) was dissolved to a concentration of 2Coverslips were cleaned by sonication in water and ethanol, immersed in a 2% vol/vol solution of triethoxy(octyl)silane (440213; Sigma-Aldrich) in isopropanol, and rinsed thoroughly to produce a hydrophobic surface. To constrain the oil to a small region and prevent seeping and flow from the chamber edges, a 2- 2-mm Teflon mask was placed on the coverslip before exposing the coverslip to UV/ozone for 10 min. This removed the hydrophobic silane treatment from all surrounding areas of the coverslip. The sample chamber was then constructed, similarly as with the bi- layer surface, by adhering a glass cylinder to the coverslip using epoxy. The surface of the coverslip within the cylinder was coated with the oil-surfactant solution, and the actin polymeri- zation mixture was immediately added.

The actin polymerization mixture consisted of an oxygen scavenging system to prevent photobleaching [4.5 mg/mL glucose, 2.7 mg/mL glucose oxidase (345486; Calbiochem), 1,700 units/mL catalase (02071; Sigma), and 0.5 vol/vol % -mercaptoethanol], and 0.3% wt/wt 15 cP methylcellulose [123] in 1 F-buffer (10 mM imidazole, pH 7.5, 1 mM MgCl2, 50 mM KCl, 0.2 mM EGTA, and 4 mM ATP). Actin from frozen stocks in G-buffer (above) was added to a final concentration of 1 M with a ratio of 1:10 TMR-maleimide labeled:unlabeled actin monomer. Polymerization of actin was allowed to proceed for 30 min. For bundled samples, fascin stored in 20 mM TrisHCl, pH 8, 10% glycerol, 100 mM NaCl, 0.2 mM EDTA, and 0.01% NaN3 was then added at a ratio of 1:10 fascin:actin monomer and allowed to form bundles for 20 min. Similarly, filamin (10 mM TrisHCl, pH 7.4, 1 mM EDTA, 1 mM DTT, 2 mM MgCl2, and 120 mM NaCl) was added at a ratio of 1:500 filamin: actin monomer and allowed to cross-link for 20 min. Monomeric myosin II was polymerized into myosin filaments separately in the same buffer conditions for 10 min and added at a ratio of 1:13 myosin monomer:actin monomer.

4.4.3 Fluorescence Microscopy

Images were obtained using an inverted microscope (Eclipse Ti-E; Nikon) with a spinning-disk confocal head (CSU-X; Yokagawa Electric) and CMOS camera (Zyla-4.2- USB3; Andor). A 40 1.15 N.A. water-immersion objective (Apo LWD; Nikon) was used for all imaging. Images were collected every 1 s using 568-nm and 647-nm excitation for the actin and myosin, respectively. Image acquisition was under automated control by Metamorph (Molecular Devices).

4.4.4 Image Analysis

Images were aligned using the StackReg (bigwww. epfl.ch/thevenaz/stackreg/) [165] plugin of ImageJ (https://imagej. nih.gov/ij/) [150] to remove drift. Background intensity was sub- tracted using the built-in subtract background plugin of ImageJ. The myosin particle density was calculated in ImageJ and actin velocity vectors were calculated using particle imaging velocimetry software (www.oceanwave.jp/softwares/mpiv/). The grid size used for PIV vector calculation was 2.4 m except for the sys- tematic variation in Fig. 4.13. All further analysis was done using custom MATLAB scripts.

All experimental image analysis plots that report values at different times were smoothed such that each data point repre- sents the average over overlapping 20-s time windows. The values of the contractile moment at different length scales in Fig. 1J, and Fig. 6D were averaged for 30 s starting with the time points of maximal magnitude of $\langle \nabla \cdot \vec{v}_a ct \rangle$ given by the asterisks in Figs. 1I and 6C. The rescaling of quantities in Fig. 3 and Fig. 4.11 was done such that their range spans from 0 to 1, for example, $l_{corr} = (L_{corr} \min(L_{corr}))/\max(L_{corr})$.

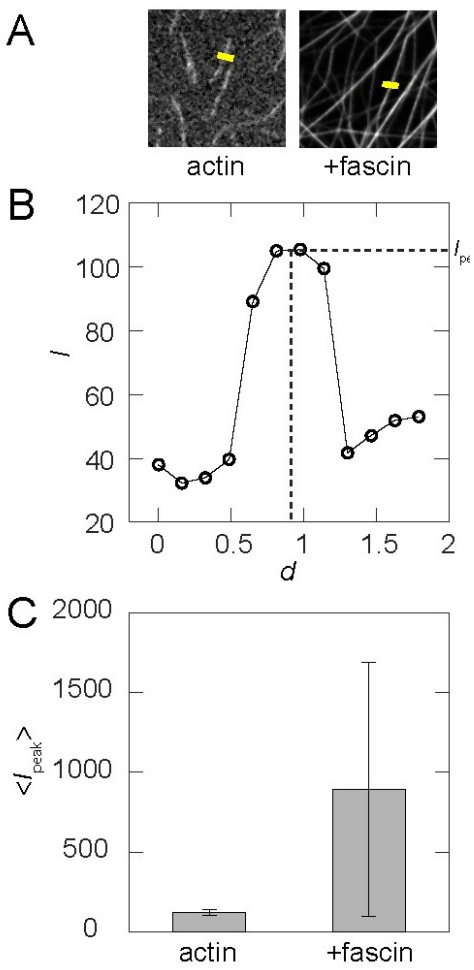

Figure 4.8: Fascin bundles contain approximately eight actin filaments. (A) Intensity scans are taken along lines perpendicular to individual actin filaments (Left) and rigid fascin bundles (Right). (B) The resulting intensity profile has a peak intensity, I_{peak}. (C) The average value of I_{peak} for fascin bundles is approximately eight times that of individual filaments.

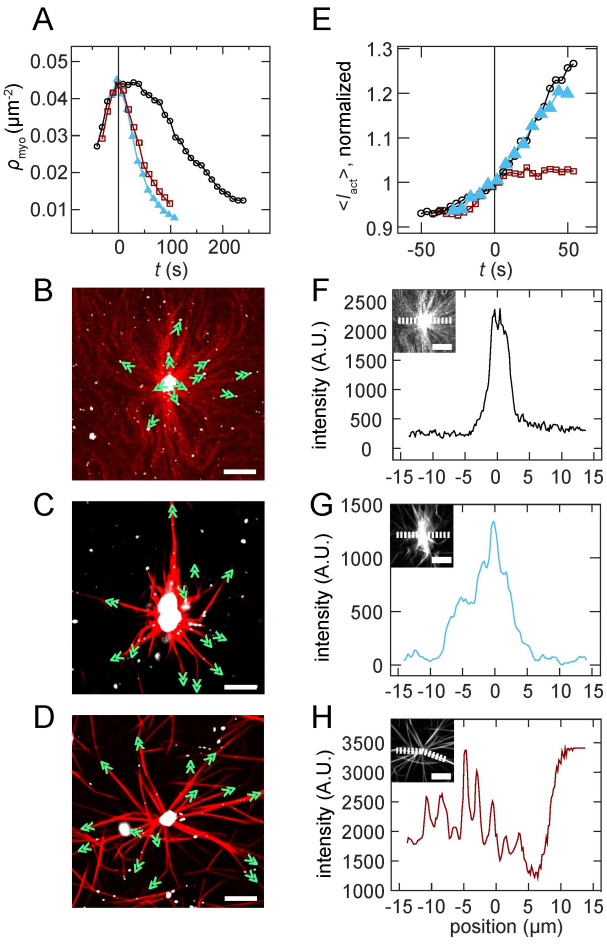

Figure 4.9: Networks form polarity-sorted asters with varying structure. (A) Time t = 0 defines the peak myosin cluster density after myosin filaments accumulate on the surface and begin to coalesce in networks of semiflexible filaments (open black circles), cross-linked rigid bundles (1:10 fascin:actin, 1:500 filamin:actin, filled blue triangles), and rigid bundles without cross-links (1:10 fascin:actin, open red squares). (BD) By tracking the motion of myosin on bundles/filaments that emanate from the aster, the local polarity is assessed and marked on images with the open end of the chevron indicating the direction of motion and direction of the barbed end. Aster polarity in networks of (B) semiflexible filaments, (C) cross-linked rigid bundles (1:10 fascin:actin, 1:500 filamin:actin), and (D) rigid bundles without cross-links (1:10 fascin:actin). (E) ¡Iact¿ in each frame is calculated by averaging the actin over all pixels that exceed a background threshold and then normalizing by the value at time $t = 0$. Densification of actin, indicated by a rise in this value, occurs in networks of semiflexible filaments (open black circles) and cross-linked rigid bundles (filled blue triangles) while rigid bundles without cross-links are rearranged without densification (open red squares). (FH) Intensity scans of clusters formed in the semiflexible filament (F), cross-linked rigid bundle (G), and uncross-linked rigid bundle (H) networks. As a consequence of the densification illustrated in E, actin is highly concentrated in the center of the asters in F and G . In contrast, the aster in H has intensity peaks diffusively spread throughout the structure. (Scale bars in BD and FH , Insets : 10 m.)

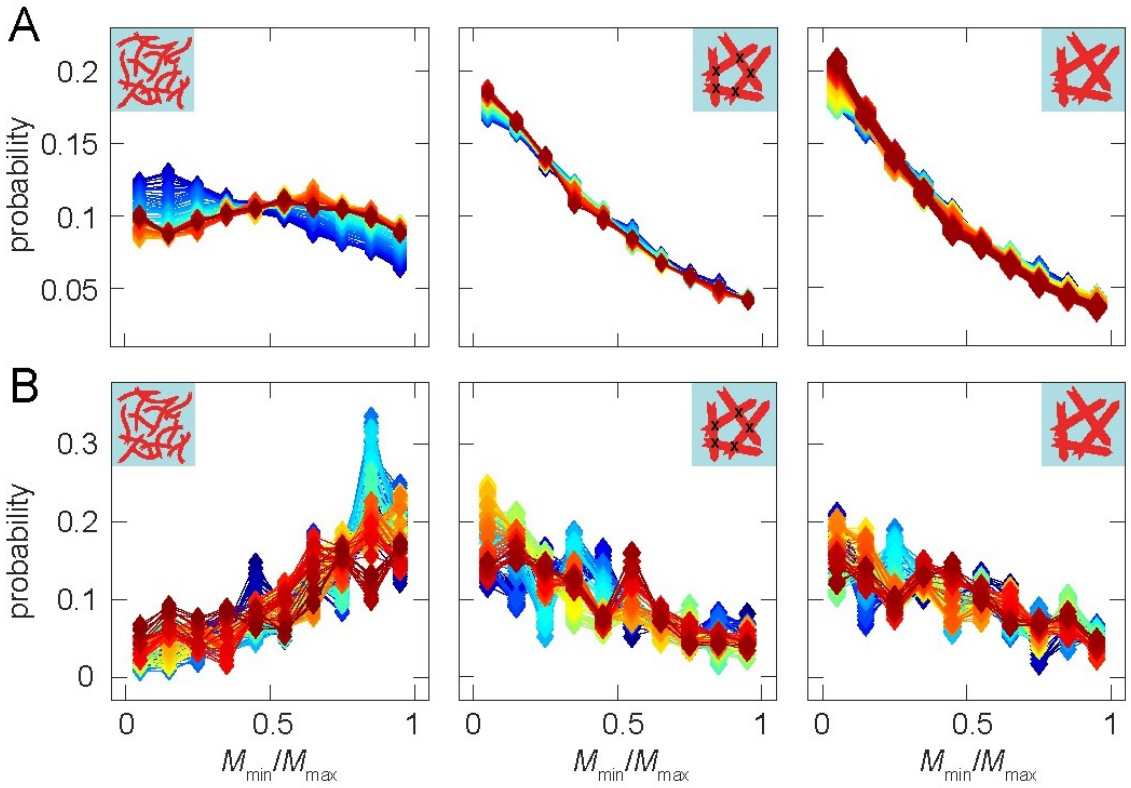

Figure 4.10: Networks have different contributions of biaxial and uniaxial deformations at varying length scales. (A) Distributions of Mmin/Mmax with s = 6 m for network of semiflexible filaments, cross-linked rigid bundles, and uncross-linked rigid bundles from left to right. (B) Distributions of Mmin/Mmax for the same samples as in A with s = 60 m.

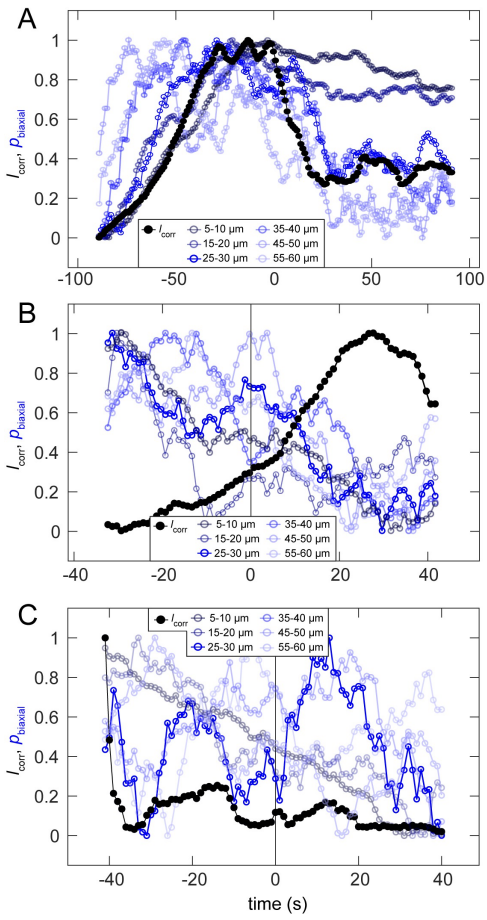

Figure 4.11: $p_{biaxial}$ at varying length scales has different trends over time for different networks. (A) $p_{biaxial}$ at all varying length scales, s (open blue circles, legend indicates value of s), initially increases and then decreases in networks of semiflexible filaments. At an intermediate value of s the trend follows that of the correlation length, l_{corr} (filled black circles). (B) $p_{biaxial}$ at varying s (open blue circles) decreases upon addition of myosin in networks of cross-linked rigid bundles, while l_{corr} (filled black circles) increases. (C) $p_{biaxial}$ (open blue circles) at small s decreases after myosin addition in networks of uncross-linked bundles but does not have a clear trend on longer length scales. Unlike the other two networks, l_{corr} decreases after myosin addition (filled black circles). For all curves, the values are shifted and scaled to range from 0 to 1.

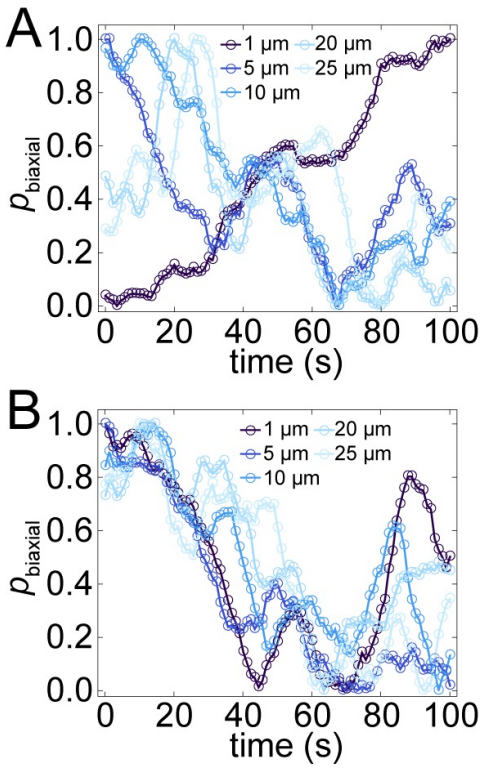

Figure 4.12: $p_{biaxial}$ at varying length scales against time in simulated networks. (A) $p_{biaxial}$ values at varying length scales, s (open blue circles, legend indicates value of s), in simulated contracting networks of semiflexible filaments. (B) $p_{biaxial}$ at varying s (open blue circles) initially decreases in simulated contracting networks of rigid bundles.

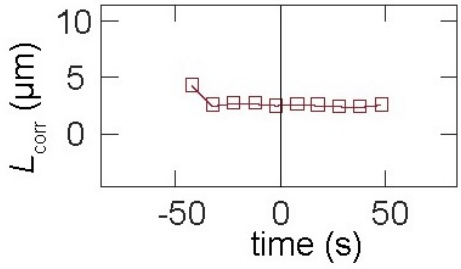

Figure 4.13: Data for network of rigid bundles without cross-links. Unscaled L_{corr} as a function of time.

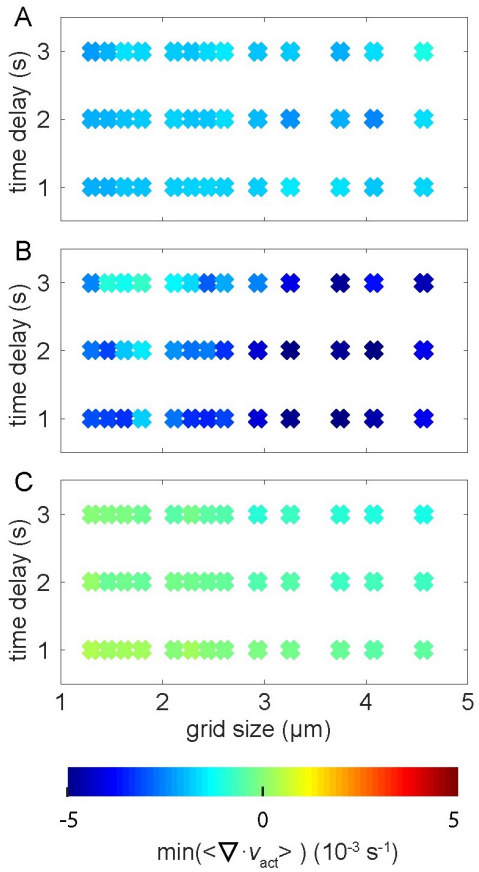

Figure 4.14: Minimum of $\langle \nabla \cdot \vec{v}_{act} \rangle$ for PIV vectors calculated with varying time delay and length scale. The minimum of the spatially averaged divergence is indicated by the color scale for semiflexible filaments (A), cross-linked rigid bundles (B), and rigid bundles without cross-links (C).

Table 4.1: Parameter Values

Symbol	Description (units) (references)	Value
	Actin Filaments	
N_f	Number of filaments	500
N_B	Number of beads per filament	11
l_a	Link rest length (μm)	1
k_a	Stretching force constant (pN/μm)	1
κ_B	Bending modulus (pNμm^2)	$[0.01, 1]$
	Myosin Motors	
ρ_m	Motor density (μm^{-2})	0.2
l_m	Rest length (μm)	0.5
k_m	Stiffness (pN/μm)	1
k_m^{on}	Maximum attachment rate (s^{-1})	1
k_m^{off}	Maximum detachment rate (s^{-1})	0.1
v_0	Unloaded speed (μm/s)	1
F_s	Stall force of myosin (pN)	10
	Crosslinkers	
ρ_{xl}	Crosslink density (μm^{-2})	$[0, 1]$
l_{xl}	Rest length (Filamin) (μm)	0.150
k_{xl}	Stiffness (pN/μm)	1
k_{xl}^{on}	Maximum attachment rate (s^{-1})	1
k_{xl}^{off}	Maximum detachment rate (s^{-1})	0.1
	Environment	
Δt	Dynamics timestep (s)	0.00002
T_F	Total simulated time (s)	200
X, Y	Length and width of assay (μm)	50
g	Grid density (μm^{-1})	1
T	Temperature (K)	300
ν	Dynamic viscosity (Pa·s)	0.001

CHAPTER 5

MECHANICAL AND KINETIC FACTORS DRIVE SORTING OF ACTIN CROSSLINKERS

This chapter is coauthored with Cristian Suarez, Jonathan Winkelman, David Kovar, Aaron Dinner, Gregory Voth, and Glen Hocky.

In cells, actin binding proteins (ABPs) segregate to different cytoskeletal networks to perform distinct functions, such as forming filopodia to enable cell migration, or polarizing actin bundles to enable cell division. Recent experimental work has uncovered a passive mechanism that may control spatial localization of ABPs: the binding of a short crosslinker protein to two actin filaments can promote the binding of other short crosslinkers and inhibit the binding of longer crosslinkers. In this work, we hypothesize that this spatial localization is due to the fact that actin is semiflexible and cannot bend over short lengths. We develop a mathematical theory and a kinetic Monte Carlo simulation to elucidate specific quantitative predictions of this hypothesis. Experiments confirm the predictions but reveal an unanticipated dependence of crosslinker domain size on the kinetics of actin filament polymerization and crosslinker binding affinity. We use simulations of a coarse-grained but molecularly explicit model to characterize the interplay of mechanical and kinetic parameters and in turn to understand the observed behavior. Our work demonstrates a physical mechanism by which cells can organize molecular material to drive biological processes, and it can guide the choice and/or design of crosslinkers for engineered protein-based materials.

5.1 Introduction

Networks formed from polymers of actin proteins perform diverse mechanical tasks throughout cells, such as enabling migration [136, 105], adhesion [132], mechanosensing [34] and division [104]. Actin filaments in these networks are connected by crosslinkers, actin binding proteins (ABPs) that link multiple filaments. A large variety of crosslinkers exist, with

diverse kinetic and mechanical properties [104]. For example, the Arp2/3 complex nucleates actin into crosslinked and branched networks at the leading edge of migrating cells, harnessing energy from actin polymerization to generate protrusive forces [180, 136]. The force propagating actin cables that maintain a cell's shape, or which are contained within a cytokinetic ring, each use their own actin crosslinking protein to form the appropriate geometry required for that process [113]. Many ABPs may be involved in a particular cellular mechanism; for example the cytokinetic ring of yeast employs formins to nucleate actin filaments, the crosslinker α-actinin to connect these filaments into anti-parallel bundles, and myosins to contract the bundles and ultimately divide the cell [172, 135]. ABP kinetics play subtle roles in these processes, e.g., we previously showed that the kinetics of binding, rather than the binding affinity of α-actinin are crucial for proper ring formation and constriction [98].

Regulating the spatial and temporal ABP organization in a noisy, crowded cellular environment is understandably complex, and determining the mechanisms involved is an active area of research. Some of this regulation may require explicit signaling pathways; for example generation of branched nextworks by the Arp2/3 complex can be activated by upstream activation of a Rho GTPase [141, 58]. In addition to these signaling-based mechanisms, recent works have detailed a *passive* mechanism by which competition between different components for the same substrate can allow self-regulation and localization in the cytoskeleton [16, 162, 183, 23]. We recently showed that α-actinin and fascin, two actin crosslinkers which are primarily found separated into different actin networks within cells can self-segregate in a simplified *in vitro* reconstitution of a branched Arp2/3 complex-nucleated network, and even segregate within the same two-filament actin bundle (Fig. 5.1A) [183]. An outstanding challenge is to determine which of the biochemical characteristics of actin, fascin, and α-actinin yield sorting, and in that way determine if this mechanism may be generalizable to other polymers or crosslinkers.

An important difference between fascin and α-actinin is their size; fascin is small (8 nm),

and therefore forms tight bundles, while α-actinin is larger (35 nm) and therefore forms more widely spaced bundles [75, 60, 183]. While α-actinin bundles filaments without regard to polarity, fascin only bundles filaments that are parallel (i.e., that have their growing, barbed end facing the same direction) [26, 12]. This means that the structures observed in our previous work (example shown in Fig. 5.1(A)) are parallel bundles in which the spacing between filaments alternates between approximately 8 and 35 nm. To change the spacing in the bundle, actin filaments must bend significantly over length scales shorter than its persistence length $L_p = 17$ μm [131], which is energetically unfavorable.

Thermodynamically, domain formation is similar to a phase separation where each of two components prefers themselves, and a surface tension prevents mixing. We therefore hypothesized that this surface tension stems from the energetic penalty incurred when actin filaments bend to change the bundle spacing [183]. The energetic cost of bending must be compensated by entropic factors, such as the benefit of binding more crosslinkers.

We use this hypothesis to develop a theoretical model that enables investigating the full range of mechanical and kinetic crosslinker properties that may lead to domain formation in actin bundles. Our theoretical analysis shows that actin polymerization and bundling affinity work together to determine the size of domains. We refine this prediction based on results from new *in vitro* experiments as well as coarse-grained simulations, and conclude that in addition to bundling affinity, the affinity of crosslinkers to single filaments promotes domain formation in low density actin environments. We further use coarse-grained simulations to predict how the lengths of crosslinkers and the flexibility of actin affect crosslinker segregation in equilibrium systems with constant length actin filaments and test our predictions using a lattice model. Thus, our theoretical models explain our experimental observations and elucidate passive mechanisms for ABP sorting in both non-equilibrium (growing actin) and equilibrium (constant-length actin) environments.

5.1.1 Factors leading to domain formation

In our previous work, we modeled domain formation as a 1D process by which new crosslinkers are added to the barbed end of a growing two-filament bundle and do not unbind [183]. These assumptions were motivated by our experimental observations that bundling occurred at approximately the same rate as filament polymerization, and domain boundaries, once formed, remained fixed for the duration of the experiment [183]. Using our model, we were able to fit an effective kinetic competition parameter $\epsilon = 4.8 k_B T$ to our experimental results (where k_B is Boltzmann's constant, and T is temperature) [183]. Since $e^{-\epsilon/k_B T} = k^{\text{on}}_{\text{diff}}/k^{\text{on}}_{\text{same}}$, this means that the rate for adding a different crosslinker and starting a new barbed-end domain ($k^{\text{on}}_{\text{diff}}$) was about 120-fold slower than the rate for continuing the same domain ($k^{\text{on}}_{\text{same}}$).

However, fitting this model does not make any connection to the underlying hypothesis that this kinetic competition is due to the cost of bending actin. To derive a similar model from first principles, we estimate the cost of bending actin such that, e.g., a fascin domain can switch to an α-actinin with a gap length of l_g along the filament. As shown in the diagram in Fig. 5.1B, the filament must bend twice at an angle θ for the filament bundle to switch domains (the geometry with one filament straight and the other bent is based on cryoelectron microscopy images of domain switches in Ref. [183]). In the absence of filament fluctuations, we estimate $\theta \approx \arcsin\left(\Delta l_{xl}/l_g\right)$ where Δl_{xl} is the difference in length between the two crosslinkers. Since the energy cost of bending an angle θ over a distance l_g for a worm-like chain is $k_B T L_p \theta^2/2l_g$ [144, 44], where L_p is the filament persistence length, k_B is Boltzmann's constant, and T is temperature, the total energy cost to bend twice to switch domains is

$$U(l_g) = \frac{k_B T L_p}{l_g} \arcsin^2\left(\frac{\Delta l_{xl}}{l_g}\right) \tag{5.1}$$

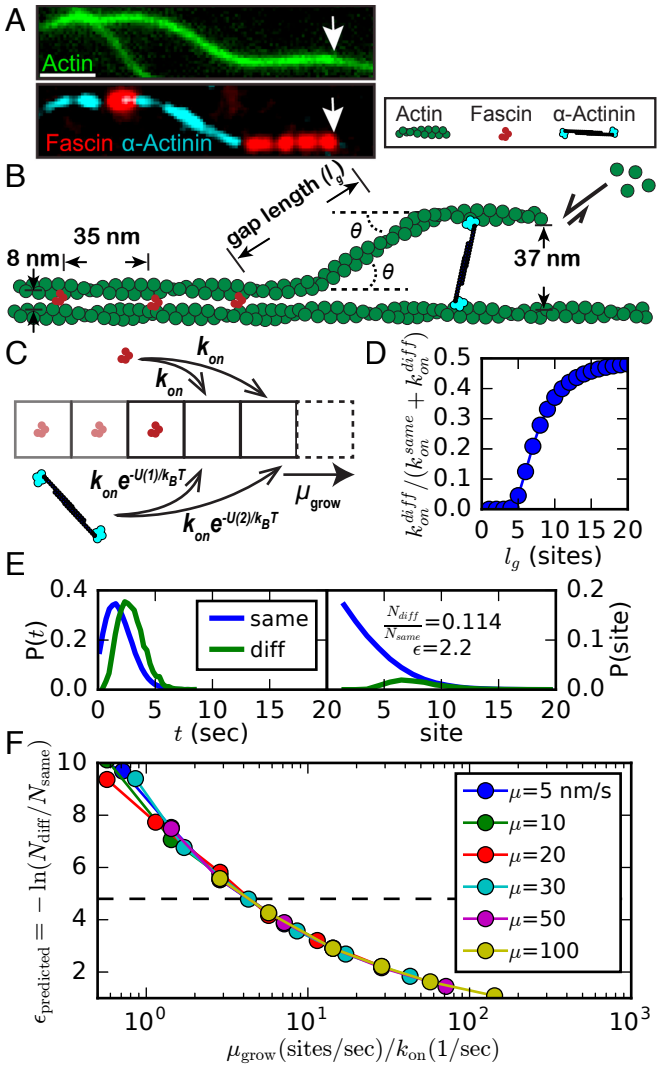

Figure 5.1: Energetic cost of filament bending leads to kinetic competition. (A) Experimental 3-color TIRF microscopy image showing two crosslinkers, fascin (red) and α-actinin (cyan) in domains on a two-filament actin bundle (green, arrows indicate polymerizing barbed end). Scale bar is 2 μm. Adapted from Ref. [183]. (B) Schematic of a two filament bundle growing at the barbed (right) end transitioning from a tight fascin bundle to a wider-spaced α-actinin bundle in an idealized geometry. The filament bends twice at an angle θ leaving a gap along the filament contour of length l_g. (C) Simple numerical model where new crosslinker binding sites are added at a rate $\mu_{\rm grow}$, and crosslinkers are added at a rate governed by Eq. 5.1 (with l_g in units of 1 site=35 nm). (D) Likelihood of adding the other ('diff') crosslinker at the barbed end at a given number of binding sites from the interface governed by Eq. 5.1, assuming equal concentrations and affinity of crosslinkers. (E) Example results from the model in (C), with $\mu_{\rm grow}$=2.86 sites/sec and $k_{\rm on}$=0.05/sec to a given site. Left: histogram of the amount of time that passes before binding the same or different crosslinker type. Right: histogram of how far from the current domain the next crosslinker adds. Inset: frequency of addition of switching bundle type, and the computed $\epsilon = -\ln(N_{\rm diff}/N_{\rm same})$. (F) Many experiments collapse onto one curve, showing that the amount of competition at the growing end depends only the ratio of growth rate to bundling rate. The dashed line shows the value fit from experiments in Ref. [183]. In (D-F), $L_p = 17$ μm and $\Delta l_{xl} = 29$ nm.

In experiment, l_g can be potentially modulated by varying the concentration of actin monomer, and hence its polymerization rate. Faster polymerization yields larger gaps, and therefore a higher probability of switching. To test this hypothesis, we incorporated (5.1) into our kinetic Monte Carlo lattice model from Ref. 183. Briefly, we model polymerization as a process whereby new sites for bundling are added at the barbed end (rightmost square in Fig. 5.1C) of a 1D lattice at a rate determined by the rate of actin polymerization. As sites are added they are probabilistically filled by one of two types of crosslinker. If the crosslinker is the same type as the barbed end domain, it is added at a constant rate k_{on}. If the crosslinker is different, then the rate is lower, $k_{\text{on}}e^{-U(l_g)/k_BT}$, but increases with distance from the barbed end domain. We test our model with $L_p = 17$ μm (corresponding to F-actin) and $\Delta l_{xl} = 29$ nm (corresponding to the difference in length between fascin and α-actinin), and confirm that the probability of a different crosslinker binding increases with gap length (Fig. 5.1D). Similarly, a domain switch generally requires a longer amount of time and a larger filament gap than a domain extension (Fig. 5.1E). Interestingly, equal site binding probability is reached after only 20 binding sites (~ 0.7 μm), much less than the persistence length of a filament (Fig. 5.1D).

We further hypothesized that it would be possible to inhibit the effect of filament growth by varying other kinetic parameters in the system, such as the binding affinity of the crosslinkers. We scan realistic conditions for filament polymerization rate and binding rates and find that the amount of competition depends only on the ratio of these two quantities (Fig. 5.1F). We find that the level of competition observed in Ref. [183] (dashed line in Fig. 5.1F), corresponds to a polymerization rate that is four-fold faster than the binding rate to a single site; i.e., on average, the filament length increases by 4 binding sites ($\sim$ 150 nm) before a crosslinker binds the bundle. As this length scale is below the resolution of TIRF experiments, it is commensurate with the observation that the bundle is zipped up by crosslinkers at approximately the same rate as the actin polymerizes.

5.1.2 Fascin and α-actinin domain lengths depend on actin polymerization rate

To test the prediction that polymerization rate affects the domain switching rate, and disentangle the role of kinetics in domain formation, we added monomeric actin to a mixture of two actin binding proteins, fascin, and α-actinin, at two different actin concentrations, 0.75 μM and 1.5 μM (Fig. 5.2A). The results (Fig. 5.2B) showed that while α-actinin bundle domain length decreased with faster filament growth rate, surprisingly, fascin bundle domain length increased. This indicates that the kinetics of the individual crosslinkers differed in such a way as to make it advantageous for α-actinin to bind more readily on slower growing filaments than fascin.

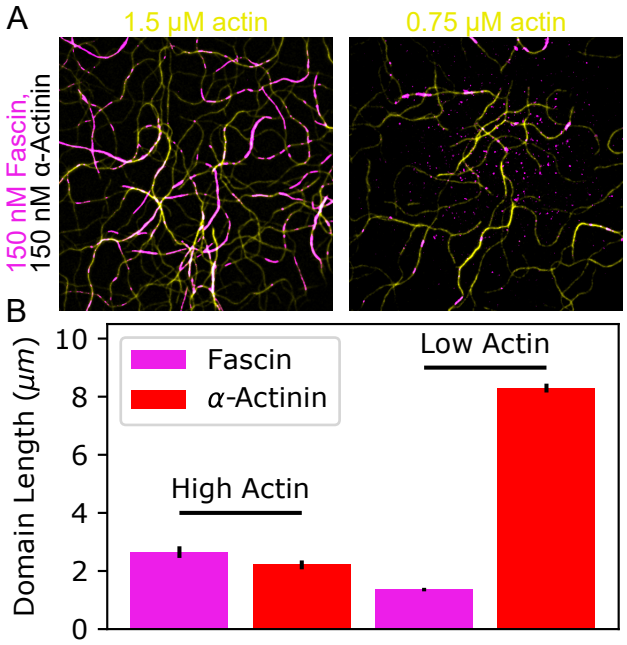

Figure 5.2: Kinetic competition in actin binding proteins. (A) Two-color TIRF image of actin filaments combined with fascin (labeled) and α-actinin (unlabeled) at two different actin concentrations. α-actinin domains are inferred from regions with double actin fluorescence but no fascin. Experiments using labeled α-actinin and labeled *fascin* conform with these results but are harder to quantify (see S.I.). (B) Average domain length for fascin and α-actinin under these two actin concentrations.

We previously showed that under these conditions, fascin and α-actinin dissociated from

actin bundles at similar rates [183]. Their affinity to a single actin filament is, however, different; we observe coating of single filaments by α-actinin, while we do not see significant residence of fascin on single filaments. This may be due to the size and flexibility of α-actinin allowing it to bind to single filaments with both binding domains [60, 26]. It is also possible that they have similar binding on bundles, but the on- and off-rate constants themselves vary by a proportionality factor. We can test if these kinetic factors can lead to a preference for one crosslinker domain on fast growing filaments, and a preference for the other on slow growing filaments, using coarse-grained simulations.

5.1.3 A simulation framework for actin and crosslinkers exhibits domain formation properties

To investigate the kinetic properties of filaments and crosslinkers that yield domain formation, we use AFINES, a coarse-grained molecular dynamics simulation framework built specifically for actin and ABP assemblies (schematic in Fig. 5.3A and model details in Section 5.2) [44, 45]. Filaments are modeled as polar worm-like chains (represented as beads connected by springs) that can grow from their barbed end by increasing the rest length of the barbed end spring at a constant rate, and adding a bead when that rest length is above a threshold. Filaments repel each other via a soft (Hookean) excluded volume interaction. Crosslinkers are modelled as Hookean springs with two ends (heads) that can stochastically bind and unbind from filaments via a Monte-Carlo procedure that preserves detailed balance. To impose that crosslinkers space filaments apart, we include a harmonic bending energy term for crosslinkers, such that crosslinkers prefer to be bound perpendicular to actin filament segments (see Methods). The simulation proceeds in 2D via Brownian dynamics, without volume exclusion from crosslinkers, to enable sufficient rearrangement. Thus, using AFINES we can systematically explore how specific crosslinker rate constants affect domain formation, and study domain formation in noisy conditions, in which bundling requires crosslinker-filament collision, and may be inhibited by filament fluctuations.

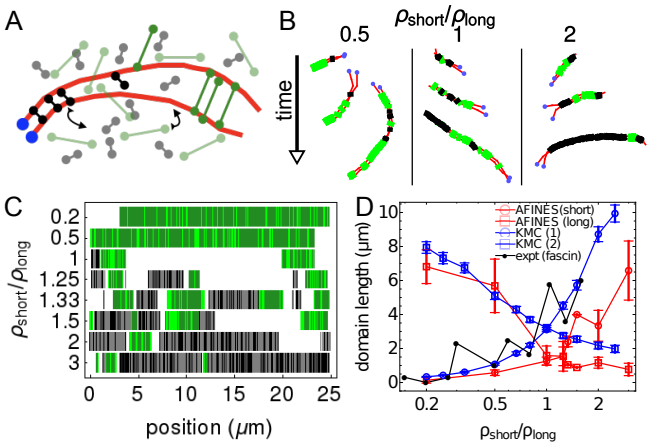

Figure 5.3: Simulation of crosslinker segregation. (A) Schematic of AFINES simulation: two filaments (red bead spring chains) are combined with two populations of crosslinkers, short (black) and long (green) that are represented as hookean springs which can dynamically bind and unbind from filaments. (B) Trajectories of filaments growing and forming crosslinker domains with a constant density of long (green) crosslinker ($\rho_{\text{long}} = 0.25\mu\text{m}^{-2}$) and varying the density of short crosslinker (left to right: $\rho_{\text{short}} = 0.125, 0.25, 0.5\mu\text{m}^{-2}$, respectively). (C) Results from domain calculation for different density ratios. Black (green) lines show discretized position of crosslinkers while gray (forest green) show extracted domains (see Section 5.2). (D) Domain length as a function of density ratio for AFINES simulations of short and long crosslinkers, Kinetic Monte Carlo simulations of two populations of crosslinkers, and experiments with actin, fascin, and α-actinin. Experimental data was first published in [183]. In (C-D), AFINES simulation use $l_{xl}^{\text{long}} = 300\text{nm}$ and $l_{xl}^{\text{short}} = 200\text{nm}$.

To benchmark our simulation against known experimental results, we simulate two growing actin filaments interacting with short and long ABPs (Fig. 5.3B). A similar system constructed of actin, fascin, and α-actinin showed domain lengths were found to depend on the concentration ratio of fascin to α-actinin concentration. To quantify domain length from AFINES simulations, we used an experimentally motivated procedure which produces discrete domain boundaries as shown in Fig. 5.3 (see Methods). Despite many simplifications in AFINES (including a lack of discrete binding sites and torsional freedom of actin) we obtain similar domain lengths as experiment with similar actin growth rates (40 nm/s), a short crosslinker length of $l_{\text{short}} = 200$ nm and long crosslinker length of $l_{\text{long}} = 300$ nm (Fig. 5.3D). While it would be ideal to use crosslinkers that are the same length as in experiment, this was computationally infeasible in the simulation due to the required high

spring stiffness (see Section 5.2 for details); using shorter length differences obtains the same characteristic highly cooperative domain length growth, but with shorter absolute domains (see Section 5.1.5 below).

5.1.4 Non-monotonic bundling efficiencies arise from binding kinetics

We now wish to investigate our earlier experiments to determine how it is possible for two crosslinkers to have equal actin bundle affinities, but form different sized domains on growing filaments. To do so, we parameterize crosslinkers in simulation to have different rate constants for binding to a single filament ($k^{\text{off(on)},1}$) and binding to a bundle ($k^{\text{off(on)},2}$) as shown in Fig. 5.4A (formula in Section 5.2).

We first test the effect of varying single filament affinity while keeping bundling affinities equal (Fig. 5.4B). When crosslinkers have equivalent rate constants (Fig. 5.4B, top row) slower growth yields larger domains for both crosslinkers, consistent with our predictions above (Fig. 5.1). However, if the short crosslinker has lower single filament affinity (Fig. 5.4B middle rows) then growth rate has the opposite effect; domain length remains constant or increases with growth rate, similar to the results observed in experiments for fascin (Fig. 5.2). This behavior is magnified at higher densities of the short crosslinker. At very low single filament affinity (Fig. 5.4B bottom row), domain formation is inhibited, indicating a threshold for the amount of time crosslinkers must remain bound to single filaments to form bundles.

We also use the simulation to test the effect of the short and long crosslinkers having different rate constants but equal (single filament and bundling) affinites, by keeping the ratio of their rate constants equal (i.e., $k^{\text{on}}_{\text{short}}/k^{\text{off}}_{\text{short}} = k^{\text{on}}_{\text{long}}/k^{\text{off}}_{\text{long}}$). In this way we can test whether it is advantageous to be a fast-on/fast-off or a slow-on/slow-off crosslinker. We found that fast-on/fast-off crosslinkers typically yield larger domains than slow-on/slow-off (Fig. 5.4C). Furthermore, fast filament growth may yield larger domains than slow filament growth, as seen in experiment (Fig. 5.4C, top row), but this does not appear to be a trend,

as very fast on/off rates yield larger domains at slower growth rates (Fig. 5.4C, bottom row).

These results indicate that the kinetics of crosslinker binding, and not only bundle affinity, are important for crosslinker segregation under non-equilibrium (polymerization) conditions. Our observations from experiment that increasing growth rate decreased α-actinin ("long") domain length but increased fascin ("short") domain length correspond best with simulation when we decreased the single filament affinity of the short crosslinker slightly (Fig. 5.4B, middle rows). A possible explanation for this result is that single filament affinity and crosslinker diffusion compete in bundle formation. In a slow growth environment, it is more advantageous to remain bound on a single filament than to freely diffuse, because the other (unbound) filament on the bundle is likely nearby. In a fast growth environment, the unbound filament may bend away from the bound filament, so dissociating from the bound filaments enables the spatial exploration necessary to find an ideal bundling location. If affinities are equal, then higher diffusion (enabled by higher rates of attachment/detachment) is advantageous to forming larger domains (Fig. 5.4C).

5.1.5 Mechanical properties of filaments and crosslinkers modulate domain length

Having established how kinetics and mechanics combine to determine domain length, we now explore a range of crosslinker sizes beyond fascin and α-actinin to understand the generality of our mechanism and how it can be used to guide the choice/design of crosslinkers for synthetic protein-based materials. Our earlier analysis suggests that the dominating factors would be crosslinker length difference, and filament persistence length. To minimize the effects of kinetic factors, we fix the densities at $\rho_{\text{short}} = \rho_{\text{long}} = 0.25\ \mu\text{m}^{-2}$, the actin filament length at $L_0 = 25\ \mu$m, and the binding rates of the short and long crosslinkers, $k^{\text{off}}_{\text{short}} = k^{\text{off}}_{\text{long}} = 0.05\ \text{s}^{-1}$ and $k^{\text{on}}_{\text{short}} = k^{\text{on}}_{\text{long}} = 2\ \text{s}^{-1}$. We find that as the difference in length between crosslinkers increases, domains of both crosslinkers appear to be longer (Fig. 5.5A) and for differences

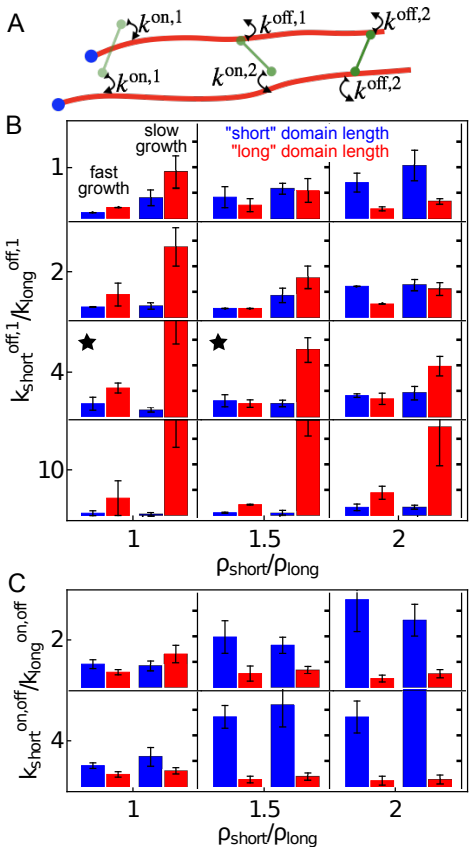

Figure 5.4: Competition between binding kinetics and polymerization in simulation. (A) Schematic of rate constants (see Section 5.2 for details). (B-C) Bar plots show domain lengths (ranging from $0-7$ μm, where each tick mark is 2 μm) of short (blue, $l_{\text{short}} = 200$ nm) and long crosslinkers (red, $l_{\text{long}} = 300$ nm) for fast actin polymerization (left, $k_{grow} = 100$ nm/s) and slow actin polymerization (right, $k_{\text{grow}} = 10$ nm/s) for varying kinetic conditions. Starred plots indicate conditions that most closely resembled experimental results (Fig. 5.2B). (B) Varying the concentration ρ_{short} and single filament dissociation constant $k_{\text{short}}^{\text{off},1}$ of the short crosslinker. Other parameters: $k_{\text{short}}^{\text{on},1(2)} = k_{\text{long}}^{\text{on},1(2)} = 2\text{s}^{-1}$, $k_{\text{short}}^{\text{off},2} = k_{\text{long}}^{\text{off},1(2)} = 0.05\text{s}^{-1}$, and $\rho_{\text{long}} = 0.25$ μm^{-2}. (C) Varying the concentration ρ_{short} of the short crosslinker and rate constants $k_{\text{long}}^{\text{off(on)}}$ of the long crosslinker, such that $k_{\text{long}}^{\text{on}}/k_{\text{long}}^{\text{off}} = k_{\text{short}}^{\text{on}}/k_{\text{short}}^{\text{off}}$. Other parameters: $k_{\text{short}}^{\text{on}} = 2\text{s}^{-1}$, $k_{\text{short}}^{\text{off}} = 0.05\text{s}^{-1}$, and $\rho_{\text{long}} = 0.25$ μm^{-2}. For both crosslinkers, single filament (1) and bundle (2) rate constants are equal. Domain lengths are averaged over the 100 s after the filament reached its full length ($l_{\text{max}} = 15$ μm) and 10 simulations, of which 5 were initialized with a short crosslinker bundle, and 5 were initialized with a long crosslinker bundle Section 5.2. Error bars are SEM.

larger than 30 nm, domain length increases with Δl_{xl}. Similarly, increasing the filament persistence length yields a significant increase in domain length (Fig. 5.5B).

AFINES includes many important aspects that could contribute to the size of domains beyond filament bending, including filament fluctuations, filament entropy lost from binding, and crosslinker entropy lost as they go from solution into a bundle. To test the effect of the energetic cost alone, we use an equilibrium 1D lattice model similar to what was presented earlier to test our kinetic hypothesis (Fig. 5.1B-C), introducing the gap energy (Eq. 5.1) into a Monte Carlo simulation of a "bundle" of fixed length. We used a constant number of binding sites, $L_0/l_b = 676$, where $L_0 = 15$ μm is the filament length and $l_b = 37$ nm is the binding site size. The energy of the lattice is given by,

$$U_{lat} = -(N_S\mu_S + N_L\mu_L) + \sum_{g\in\text{gaps}} U(l_g) \tag{5.2}$$

where $N_{S(L)}$ is the number of short (long) crosslinkers, $\mu_{S(L)}$ are their chemical potentials, $U(l_g)$ uses Eq. 5.1 and and "gaps" is the set of all empty lattice patches between short and long crosslinkers.

We were able to compare our lattice model to AFINES simulations without any free parameters. We determine $\mu_{S(L)}$ directly from AFINES by measuring the number of crosslinkers bound to two filaments in AFINES simulations with only that crosslinker, N_b. Assuming the energies in the corresponding lattice model are Boltzmann distributed, and that the energy of a lattice site not being occupied is 0, while the lattice site being occupied is $-\mu$, we can evaluate the partition function to determine the average lattice occupancy number and thus obtain $N_b = 1/\langle(1+e^{-\mu/k_BT}\rangle)$, or $\mu = -k_BT\ln(1/N_b - 1)$. We compute the final state of the lattice using the Metropolis algorithm: iteratively, we switch a randomly chosen site to a randomly chosen new state with probability $\min(1, \exp(-\Delta U_{lat}/k_BT))$, where ΔU_{lat} is the energy cost incurred by switching [112]. Our results from the lattice simulation conform well with the AFINES simulations (Fig. 5.5B-C) indicating that the mechanical model for

crosslinker segregation is a good predictor for domain length in a non-polymerizing filament.

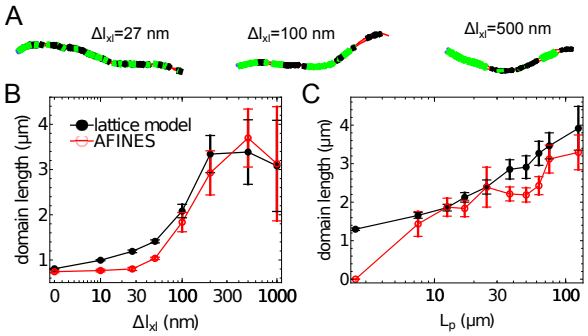

Figure 5.5: Mechanical constraints on filament bending. (A) Example domains from AFINES simulations when varying the crosslinker length difference. (B) Domain lengths (averaged over 10 simulations; error bars are SEM) from AFINES and lattice model as a function of Δl_{xl}. (C) Same as C, but varying filament persistence length L_p.

Discussion and Conclusions

We developed a mechanical theory for the source of phase separation between distinct crosslinker populations in actin bundles first reported in Ref 183. By testing this theory via kinetic Monte Carlo simulation, we were able to make a quantitative prediction about the system's kinetics: increasing actin polymerization rate would decrease the length of crosslinker domains, at constant bundling affinity. We tested this prediction in experiment, by combining actin with fascin and α-actinin, which typically have similar bundling affinities, at different polymerization rates. We found that domain length only decreased for the longer crosslinker, α-actinin, while it increased for fascin, indicating the importance of single filament kinetics.

Using coarse-grained simulations to explore how crosslinker kinetics impact domain length, we determined regimes in which changing polymerization rate could switch the identity of the apparently dominant crosslinker on a crosslinker bundle. Our results indicated that longer crosslinkers may have a higher affinity to a single filament than shorter crosslinkers, even if they exhibit similar bundling rates, which corresponds with our experimental

observations that both domains of α-actinin could bind to the same filament, yielding an effectively higher single filament affinity than fascin. We then used coarse-grained simulations to explore how mechanical properties of crosslinkers and filaments may impact domain length, and found they corresponded well with our mechanical theoretical model. Thus, we predict that bundling proteins with larger domain length differences than α-actinin and fascin (27 nm) and filamentous bio-molecules with larger persistence lengths than actin (17 μm) will have even more capacity to sort crosslinkers than we observed. While it is experimentally difficult to control the length of a crosslinker independently of its binding affinity [97], engineered crosslinkers with tunable length spacers made from DNA may enable controlled experiments in the future.

Our study motivates other future experimental and theoretical directions as well. As we have begun to explore and predict the role of polymerization in domain formation, it would be worthwhile to systematically vary the polymerization rate of actin in experiment and measure the effect on domain length. A possible limitation to our study is that the experimental setup may exhibit interactions between actin and the coverslip, which prevent crosslinkers from unbinding. Coarse grained simulations do not have this limitation, and indeed exhibit domain flux, domain merging, and domain splitting, motivating the same experiment on a passivated or lipid surface, where crosslinkers would be more free to unbind from the bundle.

Future modeling can expand on this work by incorporating further molecular details of actin filaments. For example, actin filaments are composed of two twisted polymers, and this structural characteristic may affect the binding length scale and spacing between crosslinkers of the same type. Other simulations may be able to harness these sorting principles to enable crosslinker sorting at network-size scales. Thus, future simulations and experiment could significantly advance our understanding of the full mechanical constraints on crosslninker sorting in actin bundles, and help determine whether these mechanism are strong enough to separate them into distinct actin networks in a cellular environment.

5.2 Supplementary Information

TIRF Experiments

Actin was purified from rabbit muscle acetone powder and labeled on surface lysines with Alexa488-succinimidylester (Life Technologies, Grand Island, NY) as described [73, 157] . Human α-actinin-4, human fascin 1 were purified and labeleled with Cy5-Monomaleimide (GE Healthcare) or TMR-6-Maleimide (Life Technologies, Grand Island, NY) as described previously [183]. Actin filament bundle lengths were measured using the ImageJ software [150].

AFINES simulation

In AFINES, actin filaments and passive crosslinkers are modeled as coarse-grained entities, whose positions are evolved in time using a combination of molecular dynamics and Monte Carlo simulation. Actin filaments are treated as worm-like chains of $N(t)+1$ beads, at time t, connected by $N(t)$ harmonic springs (links) and $N(t)-1$ angular harmonic springs. Thus, the internal forces on an actin filament can be obtained from the gradient of the potential energy $U_f(t)$:

$$U_f(t) = \frac{k_a}{2} \sum_{i=1}^{N(t)} \left(|\vec{r}_i - \vec{r}_{i-1}| - l_{a,i}(t)\right)^2 + \frac{\kappa_B}{2l_a} \sum_{i=2}^{N(t)} \theta_i^2, \tag{5.3}$$

where $\vec{r}_i$ is the position of the i^{th} bead on a filament, θ_i is the angle between the i^{th} and $(i-1)^{th}$ links, k_a is the stretching force constant, κ_B is the bending modulus, and $l_{a,i}(t)$ is the equilibrium length of a link. The persistence length of the filament is then $L_p = \kappa_B / k_B T$, where k_B is Boltzmann's constant and T is the temperature.

The rest length of all the springs other than the one at the barbed end is constant, such that $l_{a,j}(t) = l_a$ for $j \in \{2 \cdots N(t)\}$. At every timestep the filament grows from the barbed

end via an irreversible Markov process, such that

$$\begin{aligned} l_{a,1}(0) &= l_a \\ P(l_{a,1}(t) + \Delta l_a \mid l_{a,1}(t)) &= k_g \Delta t \end{aligned} \tag{5.4}$$

where $P(l_B|l_A)$ is the probability of the barbed end link having length l_B if on the previous timestep it had length l_A, Δl_a is the increase in segment length, k_g is the rate of segment addition, and Δt is the simulation timestep; $k_g \Delta l_a$ is thus the growth rate. If $l_{a,1}(t) + \Delta l_a > 2l_a$, the barbed end link is split into two links, such that each has rest length l_a, and the total number of segments $N_a(t)$ is incremented by 1. We set a maximum number of segments such that the filament stops growing when $N(t) \geq N_{\max}$.

Springs on different filaments are restricted from overlapping via a soft (Hookean) excluded volume interaction,

$$U_{ij} = \begin{cases} k_{\text{exv}}(1 - \vec{r}_{ij}/r_{\max})^2 & |r_{ij}| < r_{\max} \\ 0 & |r_{ij}| > r_{\max} \end{cases} \tag{5.5}$$

where k_{exv} is the interaction stiffness, r_{ij} is the vector whose norm is the distance of closest approach between the springs i and j, and $r_{\max}$ is a cutoff distance for interaction. Excluded volume forces are propogated to filament beads via the lever rule defined below for crosslinkers (Eq. 5.7).

We model crosslinkers as Hookean springs, with two ends (heads L and R) that can stochastically bind to and unbind from filaments. In addition to our previous implementation [44], we incorporate a bending term into the crosslinker, so that it prefers to bind perpendicular to filaments, and have different binding rates for 1 and 2 heads. Thus, the

potential energy of a crosslinker is

$$
\begin{aligned}
U_{xl} &= U_{xl}^{\text{stretch}} + U_{xl}^{\text{bend}} + U_{xl}^{\text{bind}} \\
U_{xl}^{\text{stretch}} &= \frac{1}{2} k_{xl} (|\vec{r}_R - \vec{r}_L| - l_{xl})^2 \\
U_{xl}^{\text{bend}} &= \kappa_{xl}^B \sum_{i \in \{L,R\}} \frac{(\alpha_i - \pi)^2 I_i}{|\vec{r}_R - \vec{r}_L| + |\vec{r}_i - \vec{r}_{a,i}|} \\
U_{xl}^{\text{bind}} &= -k_B T \left(\ln \left(\frac{k_{xl}^{\text{on},1}}{k_{xl}^{\text{off},1}} \right) (I_L \vee I_R) + \ln \left(\frac{k_{xl}^{\text{on},2}}{k_{xl}^{\text{off},2}} \right) (I_L \wedge I_R) \right)
\end{aligned}
\tag{5.6}
$$

where k_{xl} is the crosslinker stiffness, l_{xl} is its rest length, $\vec{r}_{L(R)}$ is the position of head $L(R)$, $I_{L(R)}$ is 1 if head $L(R)$ is bound and 0 otherwise, κ_{xl}^B is the bending stiffness of the crosslinker, α_i is the angle between the i^{th} bound head and the filament spring to which it is bound, $\vec{r}_{a,i}$ is the position of the nearest actin bead on that filament spring, $k_{xl}^{\text{on,j}}(k_{xl}^{\text{off,j}})$ is the rate constant for a head binding (unbinding) if $j-1$ heads ($j \in \{1,2\}$) are already bound, and $\vee$ ($\wedge$) indicates the binary OR (AND) operation.

When a crosslinker is bound, it moves with the filament to which it is bound. When both crosslinker heads are bound, its tensile force, $\vec{F}_{xl}$ is propagated onto the filament beads neighboring each bound head at position $\vec{r}_{xl}$ via the lever rule,

$$
\vec{F}_i = \vec{F}_{xl} \frac{|\vec{r}_{i+1} - \vec{r}_{xl}|}{|\vec{r}_{i+1} - \vec{r}_i|} \quad \text{and} \quad \vec{F}_{i+1} = \vec{F}_{xl} - \vec{F}_i, \tag{5.7}
$$

where $\vec{F}_i$ is the force on the filament bead at position $\vec{r}_i$.

Binding and unbinding are governed by a Monte Carlo procedure constructed to satisfy detailed balance in the absence of motors. At each timestep of duration Δt, an unbound crosslinker head becomes bound to the i^{th} nearby filament with probability $k_{xl}^{\text{on}} \Delta t P_i$, where P_i is defined as follows. The closest point on the filament is identified, and the change in energy associated with moving the head to it, ΔU_i is computed; $P_i = \min\left[1, \exp\left(-\Delta U_i / k_B T\right)\right]$. When a head becomes bound, its displacement, in the frame of reference of the filament link to which it attached, is stored as $\Delta \vec{r}$. Later, the head can become unbound and displaced

$-\Delta\vec{r}$ with probability $k_{xl}^{\text{off}}\Delta t P$, where $P = \min\left[1, \exp(-\Delta U/k_B T)\right]$ and ΔU is the energy associated with the displacement. Because the dynamics depend on the allowed moves in the Monte Carlo procedure, care must be used in interpreting the values of the rate constants. That said, the values that we obtain by tuning the parameters to yield behaviors consistent with experiments are generally within an order of magnitude of measured rate constants. As binding rate is affected by mechanical energy, and bending energy is added upon binding (U_{xl}^{bend} in Eq. 5.6), our model exhibited a bias such that longer crosslinkers had higher affinity than shorter crosslinkers if they had the same κ_{xl}^{B}; empirically, we found that setting $\kappa_{xl}^{B} = \kappa_{xl}^{B,0}/l_{xl}$ suppressed this bias.

We simulate the system using Brownian dynamics such that the position of an actin bead, motor head, or crosslinker head at time t is generated by the equation

$$\vec{r}(t+\Delta t) = \vec{r}(t) + \vec{F}(\vec{r}(t))\mu\Delta t + \sqrt{\frac{k_B T \mu \Delta t}{2}}\left(\vec{W}(t+\Delta t) + \vec{W}(t)\right), \tag{5.8}$$

where $\vec{F}(\vec{r}(t))$ is the gradient of the potential of the particle, $\vec{W}(t)$ is a vector of random numbers drawn from the standard normal distribution, and we use the Stokes relation $\mu = 1/(6\pi R\nu)$ in the damping term, where R is the size of the particle, and ν is the dynamic viscosity of its environment [92]. We simulate the system in 2D and use periodic boundary conditions to limit boundary effects. A complete list of model parameters used for Figs. 5.3 to 5.5 is provided in Table 5.1.

Guaranteeing that filaments formed bundles in simulation required very high crosslinker concentrations, which required significantly longer computation. In cases that filaments did bundle, we found that increasing crosslinker concentration above $\rho_{xl} = 0.25\mu\text{m}^{-2}$, did not significantly effect our domain length results; only the ratio of concentrations of the two crosslinkers. Thus, in our simulations we use $\rho_{xl} = 0.25\mu\text{m}^{-2}$, but promote forming a bundling via the initial conditions. Specifically, we initialize the two filaments to be parallel, at the same x coordinate, and separated in y by the average crosslinker length. Additionally

Symbol	Description (units) [ref]	Value
	Actin Filaments	
N_f	number of filaments (μm^{-2})	2
$N_{l,0}$	intial number of links per filament	2,25
N_{max}	max number of links per filament	15,25
l_a	link rest length (μm) [129]	1
k_a	stretching force constant (pN/ μm)	5
κ_B	bending modulus (pN μm^2) [131]	$[0.01, 0.5]$
k_g	growth rate (s^{-1})	1
Δl_a	growth length (μm)	$[0.008, 100]$
k_{exv}	excluded volume stiffness (pN μm^2)	0.04
$r_{\max}$	excluded volume cutoff (μm)	0.05
	Short Crosslinkers	
ρ_{xl}	density (μm^{-2})	$[0.05, 0.75]$
l_{xl}	rest length (μm) [40]	0.2
k_{xl}	stiffness (pN/ μm)	10
$\kappa_{xl}^{B,0}$	unnormalized bending stiffness (pN μm^3)	0.04
$k_{xl}^{\text{on},1}$	maximum attachment rate from both unbound (s^{-1})	2
$k_{xl}^{\text{off},1}$	maximum detachment rate from one bound (s^{-1})	$0.05, 0.2$
$k_{xl}^{\text{on},2}$	maximum attachment rate from one bound (s^{-1})	2
$k_{xl}^{\text{off},2}$	maximum detachment rate from both bound (s^{-1})	0.05
	Long Crosslinkers	
ρ_{xl}	density (μm^{-2})	0.25
l_{xl}	rest length (μm) [40]	$[0.2, 1.2]$
k_{xl}	stiffness (pN/ μm)	10
$\kappa_{xl}^{B,0}$	unnormalized bending stiffness (pN μm^3)	0.04
$k_{xl}^{\text{on},1}$	maximum attachment rate from both unbound (s^{-1})	$0.5, 2$
$k_{xl}^{\text{off},1}$	maximum detachment rate from one bound (s^{-1})	$0.0125, 0.05$
$k_{xl}^{\text{on},2}$	maximum attachment rate from one bound (s^{-1})	$0.5, 2$
$k_{xl}^{\text{off},2}$	maximum detachment rate from both bound (s^{-1})	$0.0125, 0.05$
	Environment	
Δt	dynamics timestep (s)	0.00002
t_F	maximum simulated time (s)	2000
X	length of assay (μm)	35
Y	width of assay (μm)	20
g	grid density (μm^{-1})	2.5
T	temperature (K)	300
ν	dynamic viscosity (Pa·s)	0.001

Table 5.1: AFINES Parameter Values

we add a small bundle of crosslinkers (9 crosslinkers with 1 μm) at the barbed end of the filaments, to promote bundle formation. To prevent this initialization procedure from introducing bias, we run separate simulations of bundles initialized with a "short" crosslinker domain and a "long" crosslinker domain, and average over these simulations in our results (Fig. 5.3D, Fig. 5.4B-C, and Fig. 5.5B-C).

Simulation domain length analysis

In AFINES, crosslinker can bind anywhere on filaments (i.e., they do not have discrete binding sites) and they do not have excluded volume interactions (i.e., their positions can overlap.) Therefore, to quantify domain length in simulation, we bin the crosslinkers by their position (relative to the top filament's barbed end) into $l_b = 37$ nm segments of the actin filament, corresponding to the size of an actin binding site. A segment is labeled "long" if it has more of the long crosslinker, "short" if it has more the short crosslinker, and empty otherwise. We define a domain as a consecutive run of at least $n_d = 4$ crosslinkers separated by less than $l_d = 1$ μm, and its length is the distance between the first and last crosslinkers (Fig. 5.3C).

CHAPTER 6

CONCLUSION

By developing a simulation and benchmarking it against known experiments, we were able to address many open-ended questions in actin biophysics. In Chapter 2, we introduced our computational model for cytoskeletal actomyosin. We benchmarked it by testing its computational efficiency, and validated it against well-tested theoretical and experimental characteristics of actomyosin, including actin filament fluctuations, the viscoelasticity of crosslinked actin networks, actin motility assays, and dependence of actin contractility on filament buckling. In this process, we also uncovered new results, including a continuous dependence of the viscoelastic regime of crosslinked actin networks on crosslinker stiffness, a parameter collapse that predicts the speed for filaments in motility assays, and a boundary-independent order parameter for contractility.

In Chapter 3, we used the model to explore structural regimes of cytoskeletal networks, and determine their biophysical function. We reproduced bundled, contracted, and polarity sorted actomyosin structures and developed order parameters that highlighted each. We developed new phase diagrams for these structures by varying actin binding protein affinities, and filament lengths. We then tested two possible functions of these networks: force transmission, and transport. To determine their force transmission, we measured their energetic response to a simple shear, and found that the viscosity and elasticity of networks depended on their motor and crosslinker concentrations, filament lengths, and crosslinker affinities. To determine their transport properties, we added small populations of motors to these structures, and found that homogenously distributed actin yielded persistent motor motion, polarity sorted actin yielded motor traps, and bundled networks exhibited both, depending on the timescale.

In Chapter 4, we used a combination of analysis and simulation to solve an actin network mystery, why did networks of polar actin filament bundles contract in the presence of motors and crosslinkers, if buckling was inhibited? Using image analysis techniques we determined

that these networks contracted via anisotropic strain, as opposed to networks of unbundled actin, which contracted via isotropic strain. By simulating the system, we further validated the experimental result: it was not necessary for filaments to buckle in order for the network to contract. By analyzing individual trajectories of filaments and motors in simulation, we determined that while filament buckling was a likely mechanism for contractility of actin filaments, actin bundle sliding could be the microscopic mechanism that yielded contractility in networks of stiff filaments. This observation was consistent with our image analysis results, as buckling is an isotropic strain while sliding is anisotropic.

In Chapter 5, we continued this exploration of microscopic mechanisms in a different actin context, and addressed how crosslinkers self-sort on growing actin bundles. We extended our simulation model to include filament growth to effectively analyze the systems kinetics, and crosslinkers with angle binding, to yield spatial exclusion. Using energetic modeling, and simulation, we found that ABP sorting exhibited non-trivial dependence on kinetic properties of the system: increased filament growth rate generally yielded less sorting, unless ABPs had a low single filament affinity. This prediction was confirmed in an experiment with two self-sorting bundling ABPs, α-actinin and fascin; the domain lengths of α-actinin decreased with increased polymerization rate, while the domain lengths of fascin increased. This was consistent with our observation in experiment that α-actinin tended to coat single actin filaments, and thus probably had higher single filament affinity, than fascin which was not observed to bind well with single actin filaments. Simulation also highlighted how mechanical properties of the system, including filament rigidity and the lengths of the crosslinkers, can be tuned to yield more or less ABP sorting.

These results could not have been obtained without simulation. In particular, careful tuning of mechanical and kinetic parameters of actin binding proteins, done in every chapter, is not possible in experiment, where actin binding proteins differ from each other in chemical composition, and therefore, usually vary by more than one mechanical or kinetic characteristic. Additionally, as it is possible to rapidly generate many trajectories in simula-

tion, we were able to develop robust order parameters to describe these systems in Chapter 3, which may have been prone to statistical error if they were only tested against a small number of experiments. Finally, as simulation produces exact trajectories of particles, we were able to investigate microscopic mechanisms (e.g., Chapters 4 and 5) beneath global system reorganization that are normally inaccessible to conventional image analysis techniques as the sizes of individual actin filaments and crosslinkers are below the diffraction limit.

Certain aspects of our model remain unrealistic and would be worthwhile to address in future iterations. For example, in experiments of crowded systems of actin, filaments align and form nematic structures [178, 186]. This may emerge in our system by including interactions between actin filaments, such as excluded volume and friction, and simulating in 3D to allow for sufficient rearrangement [96, 111]. Additionally, in the absence of capping protein, actin filament length is constantly changing due to polymerization and depolymerization. This behavior leads to phenomena that actively drive cortical flows by moving filaments, such as filament recycling, and filament treadmilling, and are important for cell motility and cell division [104]. While growth dynamics require non-trivial coarse-graining (for example, contrast our method in Chapter 5 with Ref. 111), a well parameterized implementation may enable active steady states, such as the cyclical contractility exhibited in cellular motility.

Another point of improvement is our implementation of specific actin binding proteins. Myosin thick filaments, have dozens to hundreds of actin binding sites, and this could lead to contractility without crosslinkers due to inactive heads increasing network connectivity [120, 159], as well as anomolous diffusion and cycling in crosslinked actin networks [151]. Thus, increasing the number of binding sites on our myosin objects may affect our results in Chapter 3, by yielding higher contractility at lower motor density, and more pervasive trapped motor behavior. Additionally, we do not limit the number of ABPs that bind to actin filaments, whereas actin has specific binding sites, which may have implications for crosslinker competition, such as that observed in Chapter 5. Significantly more complicated dynamics, such as network branching and filopodia formation, may be modellable by incor-

porating even more complex ABPs interactions into the model, such as crosslinkers that can promote or inhibit filament growth and bind at specific angles.

Even with our minimal model, we were able to explore many regimes of cytoskeletal behavior. We deduced the components, as well as kinetic and mechanical characteristics necessary for building specific actin structures and the dynamic functions different actin structures enable. We parsed molecular mechanisms implicit in actomyosin dynamics, and determined regimes of rigidity and connectivity for different forms of contractility. We explored how kinetic and mechanical aspects of actin filament and ABPs led to self-sorting of crosslinkers in a minimal system. Most importantly, we have developed a computational framework which other scientists can use to explore and predict cytoskeletal behavior, and build on to enable a robust understanding of the diverse active materials properties exhibited by cells.

REFERENCES

[1] Mike P. Allen and Dominic J. Tildesley. *Computer Simulation of Liquids*. Oxford University Press, New York, NY, 1989.

[2] Jose Alvarado, Michael Sheinman, Abhinav Sharma, Fred C. MacKintosh, and Gijsje H. Koenderink. Molecular motors robustly drive active gels to a critically connected state. *Nat. Phys.*, 9(9):591–597, 09 2013.

[3] Munehiro Asally, Mark Kittisopikul, Pau Ru, Yingjie Du, Zhenxing Hu, Tolga aatay, Andra B. Robinson, Hongbing Lu, Jordi Garcia-Ojalvo, and Grol M. Sel. Localized cell death focuses mechanical forces during 3d patterning in a biofilm. *Proc. Natl. Acad. Sci. USA*, 109(46):18891–18896, 2012.

[4] F. Backouche, L. Haviv, D. Groswasser, and A. Bernheim-Groswasser. Active gels: dynamics of patterning and self-organization. *Phys Biol*, 3(4):264–73, 2006.

[5] Shiladitya Banerjee and M Cristina Marchetti. Instabilities and oscillations in isotropic active gels. *Soft Matter*, 7(2):463–473, 2011.

[6] Julio M Belmonte, Maria Leptin, and François Nédélec. A theory that predicts behaviors of disordered cytoskeletal networks. *Mol. Syst. Biol.*, 13(9):941, 2017.

[7] Poul M Bendix, Gijsje H Koenderink, Damien Cuvelier, Zvonimir Dogic, Bernard N Koeleman, William M Brieher, Christine M Field, L Mahadevan, and David A Weitz. A quantitative analysis of contractility in active cytoskeletal protein networks. *Biophys. J.*, 94(8):3126–3136, 2008.

[8] Tamara Carla Bidone, Wonyeong Jung, Daniel Maruri, Carlos Borau, Roger D Kamm, and Taeyoon Kim. Morphological transformation and force generation of active cytoskeletal networks. *PLoS Comput. Biol.*, 13(1):e1005277, 2017.

[9] R Byron Bird, Robert C Armstrong, and Ole Hassager. *Dynamics of polymeric liquids. Vol. 1: Fluid mechanics*. John Wiley and Sons Inc., New York, NY, 1987.

[10] R. Blackwell, O. Sweezy-Schindler, C. Baldwin, L. E. Hough, M. A. Glaser, and M. D. Betterton. Microscopic origins of anisotropic active stress in motor-driven nematic liq. cryst. *Soft Matter*, 12(10):2676–2687, 2016.

[11] Robert Blackwell, Oliver Sweezy-Schindler, Christopher Baldwin, Loren E Hough, Matthew A Glaser, and MD Betterton. Microscopic origins of anisotropic active stress in motor-driven nematic liq. cryst. *Soft Matter*, 12(10):2676–2687, 2016.

[12] Laurent Blanchoin, Rajaa Boujemaa-Paterski, Cécile Sykes, and Julie Plastino. Actin dynamics, architecture, and mechanics in cell motil. *Physiol. Rev.*, 94(1):235–263, 2014.

[13] David H Boal. *Mechanics of the Cell*. Cambridge University Press, 2012.

[14] L Bourdieu, T Duke, MB Elowitz, DA Winkelmann, S Leibler, and A Libchaber. Spiral defects in motility assays: a measure of motor protein force. *Phys. Rev. Lett.*, 75(1):176, 1995.

[15] Crista M Brawley and Ronald S Rock. Unconventional myosin traffic in cells reveals a selective actin cytoskeleton. *Proc. Natl. Acad. Sci. USA*, 106(24):9685–9690, 2009.

[16] Thomas A Burke, Jenna R Christensen, Elisabeth Barone, Cristian Suarez, Vladimir Sirotkin, and David R Kovar. Homeostatic actin cytoskeleton networks are regulated by assembly factor competition for monomers. *Curr. Biol.*, 24(5):579–585, 2014.

[17] Dylan T Burnette, Suliana Manley, Prabuddha Sengupta, Rachid Sougrat, Michael W Davidson, Bechara Kachar, and Jennifer Lippincott-Schwartz. A role for actin arcs in the leading-edge advance of migrating cells. *Nat. Cell Biol.*, 13(4):371, 2011.

[18] Stanislav Burov, S. M. Ali Tabei, Toan Huynh, Michael P. Murrell, Louis H. Philipson, Stuart A. Rice, Margaret L. Gardel, Norbert F. Scherer, and Aaron R. Dinner. Distribution of directional change as a signature of complex dynamics. *Proc. Natl. Acad. Sci. USA*, 110(49):19689–19694, 2013.

[19] C Bustamante, JF Marko, ED Siggia, and S Smith. Entropic elasticity of slambda s-phage dna. *Science*, 265:1599–1600, 1994.

[20] James P. Butler, Iva Marija Tolić-Nørrelykke, Ben Fabry, and Jeffrey J. Fredberg. Traction fields, moments, and strain energy that cells exert on their surroundings. *American J. Physiol. (Lond.)-Cell Physiology*, 282(3):C595–C605, 2002.

[21] M. Cetera, G. R. Ramirez-San Juan, P. W. Oakes, L. Lewellyn, M. J. Fairchild, G. Tanentzapf, M. L. Gardel, and S. Horne-Badovinac. Epithelial rotation promotes the global alignment of contractile actin bundles during drosophila egg chamber elongation. *Nat Commun*, 5:5511, 2014.

[22] Melissa Chesarone-Cataldo, Christophe Guérin, H Yu Jerry, Roland Wedlich-Soldner, Laurent Blanchoin, and Bruce L Goode. The myosin passenger protein smy1 controls actin cable structure and dynamics by acting as a formin damper. *Dev. Cell*, 21(2):217–230, 2011.

[23] Jenna R Christensen, Glen M Hocky, Kaitlin E Homa, Alisha N Morganthaler, Sarah E Hitchcock-DeGregori, Gregory A Voth, and David R Kovar. Competition between Tropomyosin, Fimbrin, and ADF/Cofilin drives their sorting to distinct actin filament networks. *Elife*, 6:e23152, 2017.

[24] Priyamvada Chugh, Andrew G Clark, Matthew B Smith, Davide AD Cassani, Kai Dierkes, Anan Ragab, Philippe P Roux, Guillaume Charras, Guillaume Salbreux, and Ewa K Paluch. Actin cortex architecture regulates cell surface tension. *Nat. Cell Biol.*, 19(6):689–697, 2017.

[25] Mmae Claessens, M. Bathe, E. Frey, and A. R. Bausch. Actin-binding proteins sensitively mediate f-actin bundle stiffness. *Nat. Mater.*, 5(9):748–753, 2006.

[26] David S Courson and Ronald S Rock. Actin crosslink assembly and disassembly mechanics for alpha-actinin and fascin. *J. Biol. Chem.*, pages jbc–M110, 2010.

[27] Susan W Craig, Christine L Lancashire, and John A Cooper. [29] preparation of smooth muscle α-actinin. In *Methods Enzymol.*, volume 85, pages 316–321. Elsevier, 1982.

[28] CJ Cyron, KW Müller, KM Schmoller, AR Bausch, WA Wall, and RF Bruinsma. Equilibrium phase diagram of semi-flexible polymer networks with linkers. *Europhys. Lett.*, 102(3):38003, 2013.

[29] Nilushi L. Dasanayake, Paul J. Michalski, and Anders E. Carlsson. General mechanism of actomyosin contractility. *Phys. Rev. Lett.*, 107(11):118101, 2011.

[30] Enrique M De La Cruz and Margaret L Gardel. Actin mechanics and fragmentation. *J. Biol. Chem.*, 290(28):17137–17144, 2015.

[31] Stephen J DeCamp, Gabriel S Redner, Aparna Baskaran, Michael F Hagan, and Zvonimir Dogic. Orientational order of motile defects in active nematics. *Nat. Mater.*, 14(11):1110, 2015.

[32] Thomas Duke, Timothy E Holy, and Stanislas Leibler. "gliding assays" for motor proteins: A theoretical analysis. *Phys. Rev. Lett.*, 74(2):330, 1995.

[33] Marina Soares e Silva, Martin Depken, Björn Stuhrmann, Marijn Korsten, Fred C MacKintosh, and Gijsje H Koenderink. Active multistage coarsening of actin networks driven by myosin motors. *Proc. Natl. Acad. Sci. USA*, 108(23):9408–9413, 2011.

[34] Adam J Engler, Shamik Sen, H Lee Sweeney, and Dennis E Discher. Matrix elasticity directs stem cell lineage specification. *Cell*, 126(4):677–689, 2006.

[35] Hajer Ennomani, Gaëlle Letort, Christophe Guérin, Jean-Louis Martiel, Wenxiang Cao, François Nédélec, Enrique M De La Cruz, Manuel Théry, and Laurent Blanchoin. Architecture and connectivity govern actin network contractility. *Curr. Biol.*, 26(5):616–626, 2016.

[36] Thorsten Erdmann and Ulrich S. Schwarz. Stochastic force generation by small ensembles of myosin ii motors. *Phys. Rev. Lett.*, 108(18):188101, 2012.

[37] Denis J. Evans and G. P. Morriss. Nonlinear-response theory for steady planar couette flow. *Phys. Rev. A*, 30:1528–1530, Sep 1984.

[38] R. Everaers, F. Jülicher, A. Ajdari, and A.C. Maggs. Dynamic fluctuations of semiflexible filaments. *Phys. Rev. Lett.*, 82(18):3717, 1999.

[39] Juan Pablo Fededa and Daniel W. Gerlich. Molecular control of animal cell cytokinesis. *Nat Cell Biol*, 14(5):440–447, 2012.

[40] Jorge M. Ferrer, Hyungsuk Lee, Jiong Chen, Benjamin Pelz, Fumihiko Nakamura, Roger D. Kamm, and Matthew J. Lang. Measuring molecular rupture forces between single actin filaments and actin-binding proteins. *Proc. Natl. Acad. Sci. USA*, 105(27):9221–9226, 2008.

[41] Jeffrey T. Finer, Robert M. Simmons, James A. Spudich, et al. Single myosin molecule mechanics: piconewton forces and nanometre steps. *Nature*, 368(6467):113–119, 1994.

[42] Giulia Foffano, Nicolas Levernier, and Martin Lenz. The dynamics of filament assembly define cytoskeletal network morphology. *Nat. Commun.*, 7:13827, 2016.

[43] Peter J Foster, Sebastian Fürthauer, Michael J Shelley, and Daniel J Needleman. Active contraction of microtubule networks. *eLife*, 4(4):e10837, 2015.

[44] Simon L Freedman, Shiladitya Banerjee, Glen M Hocky, and Aaron R Dinner. A versatile framework for simulating the dynamic mechanical structure of cytoskeletal networks. *Biophys. J*, 113(2):448–460, 2017.

[45] Simon L Freedman, Glen M Hocky, Shiladitya Banerjee, and Aaron R Dinner. Nonequilibrium phase diagrams for actomyosin networks. *Soft Mat., In Press*, 2018.

[46] Marco Fritzsche, Christoph Erlenkämper, Emad Moeendarbary, Guillaume Charras, and Karsten Kruse. Actin kinetics shapes cortical network structure and mechanics. *Sci. Adv.*, 2(4):e1501337, 2016.

[47] C. Frontali, E. Dore, A. Ferrauto, E. Gratton, A. Bettini, M.R. Pozzan, and E. Valdevit. An absolute method for the determination of the persistence length of native dna from electron micrographs. *Biopolymers*, 18(6):1353–1373, 1979.

[48] Takashi Fujii, Atsuko H Iwane, Toshio Yanagida, and Keiichi Namba. Direct visualization of secondary structures of f-actin by electron cryomicroscopy. *Nature*, 467(7316):724, 2010.

[49] Sharat Gadde and Rebecca Heald. Mechanisms and molecules of the mitotic spindle. *Curr. Biol.*, 14(18):R797–R805, 2004.

[50] T Gao, R Blackwell, MA Glaser, MD Betterton, and MJ Shelley. Multiscale polar theory of microtubule and motor-protein assemblies. *Phys. Rev. Lett.*, 114(4), 2015.

[51] M.L. Gardel, J.H. Shin, F.C. MacKintosh, L. Mahadevan, P. Matsudaira, and D.A. Weitz. Elastic behavior of cross-linked and bundled actin networks. *Science*, 304(5675):1301–1305, 2004.

[52] Mathias Gautel and Kristina Djinovi-Carugo. The sarcomeric cytoskeleton: from molecules to motion. *The J. Exp. Biol.*, 219(2):135, 2016.

[53] Scott F. Gilbert. *Dev. Biol.* Sinauer Associates, Sunderland, MA, 2010.

[54] Daniel T Gillespie. Exact stochastic simulation of coupled chemical reactions. *J. Phys. Chem.*, 81(25):2340–2361, 1977.

[55] F. Gittes, B. Mickey, J. Nettleton, and J. Howard. Flexural rigidity of microtubules and actin-filaments measured from thermal fluctuations in shape. *J. Cell Biol.*, 120(4):923–934, 1993.

[56] Frederick Gittes, Brian Mickey, Jilda Nettleton, and Jonathon Howard. Flexural rigidity of microtubules and actin filaments measured from thermal fluctuations in shape. *J Cell Biol.*, 120(4):923–934, 1993.

[57] Herbert Goldstein. *Classical mechanics*. Pearson Education India, 2011.

[58] Erin D Goley and Matthew D Welch. The arp2/3 complex: an actin nucleator comes of age. *Nat. Rev. Mol. Cell Biol.*, 7(10):713, 2006.

[59] Daniel Gordon, Anne Bernheim-Groswasser, Chen Keasar, and Oded Farago. Hierarchical self-organization of cytoskeletal active networks. *Phys. Biol.*, 9(2):026005, 2012.

[60] Cheri M Hampton, Dianne W Taylor, and Kenneth A Taylor. Novel structures for α-actinin: F-actin interactions and their implications for actin–membrane attachment and tension sensing in the cytoskeleton. *J. Mol. Biol.*, 368(1):92–104, 2007.

[61] Albert K. Harris, David Stopak, and Patricia Wild. Fibroblast traction as a mechanism for collagen morphogenesis. *Nature*, 290(5803):249–251, 1981.

[62] David E. Harris and D.M. Warshaw. Smooth and skeletal muscle myosin both exhibit low duty cycles at zero load in vitro. *J. Biol. Chem.*, 268(20):14764–14768, 1993.

[63] J. H. Hartwig and T. P. Stossel. Cytochalasin b and the structure of actin gels. *J Mol Biol*, 134(3):539–53, 1979.

[64] J. H. Hartwig and T. P. Stossel. Structure of macrophage actin-binding protein molecules in solution and interacting with actin filaments. *J Mol Biol*, 145(3):563–81, 1981.

[65] D. A. Head, A. J. Levine, and F. C. MacKintosh. Distinct regimes of elastic response and deformation modes of cross-linked cytoskeletal and semiflexible polymer networks. *Phys. Rev. E*, 68:061907, Dec 2003.

[66] G. Henkin, S. J. DeCamp, D. T. Chen, T. Sanchez, and Z. Dogic. Tunable dynamics of microtubule-based active isotropic gels. *Philos Trans A Math Phys Eng Sci*, 372(2029), 2014.

[67] Robert Hetland and John Travers. SciPy: Open source scientific tools for Python: rbf - radial basis functions for interpolation/smoothing scattered nd data, 2001.

[68] Hideo Higuchi, Toshio Yanagida, and Yale E. Goldman. Compliance of thin filaments in skinned fibers of rabbit skeletal muscle. *Biophys. J.*, 69(3):1000–1010, 1995.

[69] Tetsuya Hiraiwa and Guillaume Salbreux. Role of turnover in active stress generation in a filament network. *Phys. Rev. Lett.*, 116(18):188101, 2016.

[70] Glen M Hocky, Joseph L Baker, Michael J Bradley, Anton V Sinitskiy, Enrique M De La Cruz, and Gregory A Voth. Cations stiffen actin filaments by adhering a key structural element to adjacent subunits. *The J. Phys. Chem. B*, 120(20):4558–4567, 2016.

[71] H.E. Huxley. The mechanism of muscular contraction. *Science*, 164(3886):1356–1366, 1969.

[72] Yaron Ideses, Adar Sonn-Segev, Yael Roichman, and Anne Bernheim-Groswasser. Myosin ii does it all: assembly, remodeling, and disassembly of actin networks are governed by myosin ii activity. *Soft Matter*, 9(29):7127–7137, 2013.

[73] Herve Isambert, Pascal Venier, Anthony C Maggs, Abdelatif Fattoum, Ridha Kassab, Dominique Pantaloni, and Marie-France Carlier. Flexibility of actin filaments derived from thermal fluctuations. effect of bound nucleotide, phalloidin, and muscle regulatory proteins. *J. Biol. Chem.*, 270(19):11437–11444, 1995.

[74] R. Ishikawa, T. Sakamoto, T. Ando, S. Higashi-Fujime, and K. Kohama. Polarized actin bundles formed by human fascin-1: their sliding and disassembly on myosin ii and myosin v in vitro. *J. Neurochem.*, 87(3):676–685, 2003.

[75] Silvia Jansen, Agnieszka Collins, Changsong Yang, Grzegorz Rebowski, Tatyana Svitkina, and Roberto Dominguez. Mechanism of actin filament bundling by fascin. *J. Biol. Chem.*, pages jbc–M111, 2011.

[76] L. W. Janson, J. Kolega, and D. L. Taylor. Modulation of contraction by gelation solation in a reconstituted motile model. *J. Cell Biol.*, 114(5):1005–1015, 1991.

[77] F. Jlicher, K. Kruse, J. Prost, and J. F. Joanny. Active behavior of the cytoskeleton. *Phys. Rep.*, 449(13):3–28, 2007.

[78] K. E. Kasza, G. H. Koenderink, Y. C. Lin, C. P. Broedersz, W Messner, F Nakamura, T. P. Stossel, F. C. MacKintosh, and D. A. Weitz. Nonlinear elasticity of stiff biopolymers connected by flexible linkers. *Phys. Rev. E*, 79(4):041928, 2009.

[79] Taeyoon Kim. Determinants of contractile forces generated in disorganized actomyosin bundles. *Biomech. Model. Mechan.*, 14(2):345–355, 2014.

[80] Taeyoon Kim, Wonmuk Hwang, Hyungsuk Lee, and Roger D Kamm. Computational analysis of viscoelastic properties of crosslinked actin networks. *PLoS Comput. Biol.*, 5(7):e1000439, 2009.

[81] Simone Koehler and Andreas R. Bausch. Contraction mechanisms in composite active actin networks. *Plos One*, 7(7), 2012.

[82] G. H. Koenderink, M. Atakhorrami, F. C. MacKintosh, and C. F. Schmidt. High-frequency stress relaxation in semiflexible polymer solutions and networks. *Phys. Rev. Lett.*, 96:138307, Apr 2006.

[83] S Kohler, V Schaller, AR Bausch, et al. Structure formation in active networks. *Nat. Mater.*, 10(6):462–468, 2011.

[84] H. Kojima, A. Ishijima, and T. Yanagida. Direct measurement of stiffness of single actin filaments with and without tropomyosin by in vitro nanomanipulation. *Proc. Natl. Acad. Sci. USA*, 91(26):12962–12966, 1994.

[85] S. J. Kron and J. A. Spudich. Fluorescent actin-filaments move on myosin fixed to a glass-surface. *Proc. Natl. Acad. Sci. USA*, 83(17):6272–6276, 1986.

[86] Stephen J. Kron and James A. Spudich. Fluorescent actin filaments move on myosin fixed to a glass surface. *Proc. Natl. Acad. Sci. USA*, 83(17):6272–6276, 1986.

[87] K Kruse and F Julicher. Actively contracting bundles of polar filaments. *Phys. Rev. Lett.*, 85(8):1778–1781, 2000.

[88] Karsten Kruse, Jean-François Joanny, Frank Jülicher, Jacques Prost, and Ken Sekimoto. Asters, vortices, and rotating spirals in active gels of polar filaments. *Phys. Rev. Lett.*, 92(7):078101, 2004.

[89] Karsten Kruse, Jean-Francois Joanny, Frank Jülicher, Jacques Prost, and Ken Sekimoto. Generic theory of active polar gels: a paradigm for cytoskeletal dynamics. *Eur. Phys. J. E Soft Matter*, 16(1):5–16, 2005.

[90] AW Lees and SF Edwards. The computer study of transport processes under extreme conditions. *J. Phys. C: Solid State Phys.*, 5(15):1921, 1972.

[91] Ben Leimkuhler and Charles Matthews. *Molecular Dynamics: with Deterministic and Stochastic Numerical Methods*. Springer, New York, NY, 2015.

[92] Benedict Leimkuhler and Charles Matthews. Robust and efficient configurational molecular sampling via langevin dynamics. *J. Chem. Phys.*, 138(17):174102, 2013.

[93] Martin Lenz. Geometrical origins of contractility in disordered actomyosin networks. *Phys. Rev. X*, 4(4):041002, 2014.

[94] Martin Lenz, Margaret L Gardel, and Aaron R Dinner. Requirements for contractility in disordered cytoskeletal bundles. *New J. Phys.*, 14(3):033037, 2012.

[95] Martin Lenz, Todd Thoresen, Margaret L Gardel, and Aaron R Dinner. Contractile units in disordered actomyosin bundles arise from f-actin buckling. *Phys. Rev. Lett.*, 108(23):238107, 2012.

[96] Gaëlle Letort, Antonio Z Politi, Hajer Ennomani, Manuel Théry, Francois Nedelec, and Laurent Blanchoin. Geometrical and mechanical properties control actin filament organization. *PLoS Comput. Biol.*, 11(5):e1004245, 2015.

[97] Yujie Li. *The dynamic F-actin crosslinker alpha-actinin is tailored for contractile ring assembly during cytokinesis in Schizosaccharomyces pombe*. PhD thesis, The University of Chicago, 2014.

[98] Yujie Li, Jenna R Christensen, Kaitlin E Homa, Glen M Hocky, Alice Fok, Jennifer A Sees, Gregory A Voth, and David R Kovar. The f-actin bundler α-actinin ain1 is tailored for ring assembly and constriction during cytokinesis in fission yeast. *Mol. Biol. Cell.*, 27(11):1821–1833, 2016.

[99] Harrison W Lin, Mark E Schneider, and Bechara Kachar. When size matters: the dynamic regulation of stereocilia lengths. *Curr. Opin. Cell Biol.*, 17(1):55–61, 2005.

[100] Yi-Chia Lin, Norman Y. Yao, Chase P. Broedersz, Harald Herrmann, Fred C. MacKintosh, and David A. Weitz. Origins of elasticity in intermediate filament networks. *Phys. Rev. Lett.*, 104:058101, Feb 2010.

[101] Ian Linsmeier, Shiladitya Banerjee, Patrick W Oakes, Wonyeong Jung, Taeyoon Kim, and Michael Murrell. Disordered actomyosin networks are sufficient to produce cooperative and telescopic contractility. *Nat. Commun.*, 7:12615, 2016.

[102] T. B. Liverpool and M. C. Marchetti. Bridging the microscopic and the hydrodynamic in active filament solutions. *EPL (Europhys. Lett.)*, 69(5):846, 2005.

[103] Tanniemola B Liverpool, M Cristina Marchetti, J-F Joanny, and J Prost. Mechanical response of active gels. *EPL (Europhys. Lett.)*, 85(1):18007, 2009.

[104] Harvey Lodish, Arnold Berk, S Lawrence Zipursky, Paul Matsudaira, David Baltimore, James Darnell, et al. *Mol. Cell biology*, volume 3. WH Freeman New York, 1995.

[105] Alexis J Lomakin, Kun-Chun Lee, Sangyoon J Han, D A Bui, Michael Davidson, Alex Mogilner, and Gaudenz Danuser. Competition of two distinct actin networks for actin defines a bistable switch for cell polarization. *Nat. Cell Biol.*, 17(11):1435, 2015.

[106] F.C. MacKintosh, J. Käs, and P.A. Janmey. Elasticity of semiflexible biopolymer networks. *Phys. Rev. Lett.*, 75(24):4425–4428, 1995.

[107] Michael Mak, Muhammad H Zaman, Roger D Kamm, and Taeyoon Kim. Interplay of active processes modulates tension and drives phase transition in self-renewing, motor-driven cytoskeletal networks. *Nat. Commun.*, 7:10323, 2016.

[108] M.C. Marchetti, J.F. Joanny, S. Ramaswamy, T.B. Liverpool, J. Prost, Madan Rao, and R Aditi Simha. Hydrodynamics of soft active matter. *Rev. Mod. Phys.*, 85(3):1143–1189, 2013.

[109] Sarkis S Margossian and Susan Lowey. [7] preparation of myosin and its subfragments from rabbit skeletal muscle. In *Methods Enzymol.*, volume 85, pages 55–71. Elsevier, 1982.

[110] John F Marko and Eric D Siggia. Stretching dna. *Macromolecules*, 28(26):8759–8770, 1995.

[111] William M McFadden, Patrick M McCall, Margaret L Gardel, and Edwin M Munro. Filament turnover tunes both force generation and dissipation to control long-range flows in a model actomyosin cortex. *PLoS Comput. Biol.*, 13(12):e1005811, 2017.

[112] Nicholas Metropolis, Arianna W Rosenbluth, Marshall N Rosenbluth, Augusta H Teller, and Edward Teller. Equation of state calculations by fast computing machines. *J. Chem. Phys.*, 21(6):1087–1092, 1953.

[113] Alphée Michelot and David G Drubin. Building distinct actin filament networks in a common cytoplasm. *Curr. Biol.*, 21(14):R560–R569, 2011.

[114] Walter Mickel, Stefan Münster, Louise M Jawerth, David A Vader, David A Weitz, Adrian P Sheppard, Klaus Mecke, Ben Fabry, and Gerd E Schröder-Turk. Robust pore size analysis of filamentous networks from three-dimensional confocal microscopy. *Biophys. J.*, 95(12):6072–6080, 2008.

[115] Marc Z Miskin, Gurdaman Khaira, Juan J de Pablo, and Heinrich M Jaeger. Turning statistical physics models into materials design engines. *Proc. Natl. Acad. Sci. USA*, 113(1):34–39, 2016.

[116] Lishibanya Mohapatra, Bruce L Goode, Predrag Jelenkovic, Rob Phillips, and Jane Kondev. Design principles of length control of cytoskeletal structures. *Annu. Rev. Biophys.*, 45:85–116, 2016.

[117] Kei W Müller, Christian J Cyron, and Wolfgang A Wall. Computational analysis of morphologies and phase transitions of cross-linked, semi-flexible polymer networks. *P. R. Soc. A*, 471(2182):20150332, 2015.

[118] E. Munro, J. Nance, and J. R. Priess. Cortical flows powered by asymmetrical contraction transport par proteins to establish and maintain anterior-posterior polarity in the early c-elegans embryo. *Dev. Cell*, 7(3):413–424, 2004.

[119] Edwin Munro, Jeremy Nance, and James R Priess. Cortical flows powered by asymmetrical contraction transport par proteins to establish and maintain anterior-posterior polarity in the early c. elegans embryo. *Dev. Cell*, 7(3):413–424, 2004.

[120] Michael Murrell and Margaret L. Gardel. Actomyosin sliding is attenuated in contractile biomimetic cortices. *Mol. Biol. Cell*, 25(12):1845–1853, 2014.

[121] Michael Murrell, Patrick W Oakes, Martin Lenz, and Margaret L Gardel. Forcing cells into shape: the mechanics of actomyosin contractility. *Nat. Rev. Mol. Cell Biol.*, 16(8):486, 2015.

[122] Michael Murrell, Todd Thoresen, and Margaret Gardel. Reconstitution of contractile actomyosin arrays. *Methods Enzymol.*, 540:265–282, 2014.

[123] Michael P. Murrell and Margaret L. Gardel. F-actin buckling coordinates contractility and severing in a biomimetic actomyosin cortex. *Proc. Natl. Acad. Sci. USA*, 109(51):20820–20825, 2012.

[124] FJ Nedelec, Thomas Surrey, Anthony C Maggs, and Stanislas Leibler. Self-organization of microtubules and motors. *Nature*, 389(6648):305, 1997.

[125] François Nédélec. Computer simulations reveal motor properties generating stable antiparallel microtubule interactions. *J. Cell Biol.*, 158(6):1005–1015, 2002.

[126] Francois Nedelec and Dietrich Foethke. Collective langevin dynamics of flexible cytoskeletal fibers. *New J. Phys.*, 9(11):427, 2007.

[127] François Nédélec, Thomas Surrey, and AC Maggs. Dynamic concentration of motors in microtubule arrays. *Phys. Rev. Lett.*, 86(14):3192, 2001.

[128] Richard Niederman and Thomas D. Pollard. Human platelet myosin ii in vitro assembly and structure of myosin filaments. *J. Cell Biol.*, 67(1):72–92, 1975.

[129] Theo Odijk. The statistics and dynamics of confined or entangled stiff polymers. *Macromolecules*, 16(8):1340–1344, 1983.

[130] Theo Odijk. Theory of lyotropic polymer liq. cryst. *Macromolecules*, 19(9):2313–2329, 1986.

[131] A. Ott, M. Magnasco, A. Simon, and A. Libchaber. Measurement of the persistence length of polymerized actin using fluorescence microscopy. *Phys. Rev. E*, 48:R1642–R1645, Sep 1993.

[132] J Thomas Parsons, Alan Rick Horwitz, and Martin A Schwartz. Cell adhesion: integrating cytoskeletal dynamics and cellular tension. *Nat. Rev. Mol. Cell Biol.*, 11(9):633–643, 2010.

[133] Mathieu Pinot, Franck Chesnel, JZ Kubiak, Isabelle Arnal, FJ Nedelec, and Zoher Gueroui. Effects of confinement on the self-organization of microtubules and motors. *Curr. Biol.*, 19(11):954–960, 2009.

[134] Steve Plimpton. Fast parallel algorithms for short-range molecular dynamics. *J. Comput. Phys.*, 117(1):1–19, 1995.

[135] Thomas D Pollard. Mechanics of cytokinesis in eukaryotes. *Curr. Opin. Cell Biol.*, 22(1):50–56, 2010.

[136] Thomas D Pollard and Gary G Borisy. Cellular motility driven by assembly and disassembly of actin filaments. *Cell*, 112(4):453–465, 2003.

[137] Konstantin Popov, James Komianos, and Garegin A Papoian. Medyan: Mechanochemical simulations of contraction and polarity alignment in actomyosin networks. *PLoS Comput. Biol.*, 12(4):e1004877, 2016.

[138] J Prost. *The physics of Liq. Cryst.* Number 83. Oxford University Press, New York, NY, 1995.

[139] J Prost, F Jülicher, and JF Joanny. Active gel physics. *Nat. Phys.*, 11(2):111–117, 2015.

[140] Daniel Riveline, Albrecht Ott, Frank Jülicher, Donald A Winkelmann, Olivier Cardoso, Jean-Jacques Lacapère, Soffia Magnúsdóttir, Jean-Louis Viovy, Laurence Gorre-Talini, and Jacques Prost. Acting on actin: the electric motility assay. *Eur. Biophys. J.*, 27(4):403–408, 1998.

[141] Rajat Rohatgi, Le Ma, Hiroaki Miki, Marco Lopez, Tomas Kirchhausen, Tadaomi Takenawa, and Marc W Kirschner. The interaction between N-WASP and the Arp2/3 complex links Cdc42-dependent signals to actin assembly. *Cell*, 97(2):221–231, 1999.

[142] Pierre Ronceray, Chase P Broedersz, and Martin Lenz. Fiber networks amplify active stress. *Proc. Natl. Acad. Sci. USA*, 113(11):2827–2832, 2016.

[143] Benoît Roux. *Molecular Machines*. World Scientific, Singapore, 2011.

[144] Michael Rubinstein and Ralph H. Colby. *Polymer Physics*. Oxford University Press, Oxford, United Kingdom, 2003.

[145] Guillaume Salbreux, Guillaume Charras, and Ewa Paluch. Actin cortex mechanics and cellular morphogenesis. *Trends Cell Biol.*, 22(10):536–545, 2012.

[146] Tim Sanchez, Daniel TN Chen, Stephen J DeCamp, Michael Heymann, and Zvonimir Dogic. Spontaneous motion in hierarchically assembled active matter. *Nature*, 491(7424):431, 2012.

[147] Volker Schaller, Christoph Weber, Christine Semmrich, Erwin Frey, and Andreas R Bausch. Polar patterns of driven filaments. *Nature*, 467(7311):73–77, 2010.

[148] Tamar Schlick. *Molecular modeling and simulation: an interdisciplinary guide: an interdisciplinary guide*, volume 21. Springer Science & Business Media, 2010.

[149] KM Schmoller, O Lieleg, and AR Bausch. Structural and viscoelastic properties of actin/filamin networks: cross-linked versus bundled networks. *Biophys. J.*, 97(1):83–89, 2009.

[150] Caroline A Schneider, Wayne S Rasband, and Kevin W Eliceiri. Nih image to imagej: 25 years of image analysis. *Nat. Methods*, 9(7):671, 2012.

[151] Monika Scholz, Stanislav Burov, Kimberly L Weirich, Björn J Scholz, S. M. Ali Tabei, Margaret L Gardel, and Aaron R Dinner. Cycling state that can lead to glassy dynamics in intracellular transport. *Phys. Rev. X*, 6(1):011037, 2016.

[152] Monika Scholz, Kimberly L Weirich, Margaret L Gardel, and Aaron R Dinner. Tuning molecular motor transport through cytoskeletal filament network organization. *bioRxiv*, page 277947, 2018.

[153] M. Schuppler, F. C. Keber, M. Kroger, and A. R. Bausch. Boundaries steer the contraction of active gels. *Nat. Commun.*, 7, 2016.

[154] Jakub Sedzinski, Maté Biro, Annelie Oswald, Jean-Yves Tinevez, Guillaume Salbreux, and Ewa Paluch. Polar actomyosin contractility destabilizes the position of the cytokinetic furrow. *Nature*, 476(7361):462, 2011.

[155] Yair Shokef and Samuel A Safran. Scaling laws for the response of nonlinear elastic media with implications for cell mechanics. *Phys. Rev. Lett.*, 108(17):178103, 2012.

[156] James A. Spudich, Stephen J. Kron, and Michael P. Sheetz. Movement of myosin-coated beads on oriented filaments reconstituted from purified actin. *Nature*, 315(6020):584–586, 1985.

[157] James A Spudich and Susan Watt. The regulation of rabbit skeletal muscle contraction i. biochemical studies of the interaction of the tropomyosin-troponin complex with actin and the proteolytic fragments of myosin. *J. Biol. Chem.*, 246(15):4866–4871, 1971.

[158] Samantha Stam, Jon Alberts, Margaret L. Gardel, and Edwin Munro. Isoforms: Confer characteristic force generation and mechanosensation by myosin ii filaments. *Biophys. J.*, 108(8):1997–2006, 2015.

[159] Samantha Stam, Simon L. Freedman, Shiladitya Banerjee, Kimberly L. Weirich, Aaron R. Dinner, and Margaret L. Gardel. Filament rigidity and connectivity tune the deformation modes of active biopolymer networks. *Proc. Natl. Acad. Sci. USA*, 114(47):E10037–10045, 2017.

[160] Kasimira T Stanhope, Vikrant Yadav, Christian D Santangelo, and Jennifer L Ross. Contractility in an extensile system. *Soft Matter*, 13(23):4268–4277, 2017.

[161] Jonathan Stricker, Tobias Falzone, and Margaret L. Gardel. Mechanics of the f-actin cytoskeleton. *J. Biomech.*, 43(1):9–14, 2010.

[162] Cristian Suarez and David R Kovar. Internetwork competition for monomers governs actin cytoskeleton organization. *Nat. Rev. Mol. Cell Biol.*, 17(12):799, 2016.

[163] Thomas Surrey, François Nédélec, Stanislas Leibler, and Eric Karsenti. Physical properties determining self-organization of motors and microtubules. *Science*, 292(5519):1167–1171, 2001.

[164] S. M. Ali Tabei, Stanislav Burov, Hee Y Kim, Andrey Kuznetsov, Toan Huynh, Justin Jureller, Louis H Philipson, Aaron R Dinner, and Norbert F Scherer. Intracellular transport of insulin granules is a subordinated random walk. *Proc. Natl. Acad. Sci. USA*, 110(13):4911–4916, 2013.

[165] Philippe Thevenaz, Urs E Ruttimann, and Michael Unser. A pyramid approach to subpixel registration based on intensity. *IEEE transactions on image processing*, 7(1):27–41, 1998.

[166] Lewis G Tilney, Edward H Egelman, David J DeRosier, and JC Saunder. Actin filaments, stereocilia, and hair cells of the bird cochlea. ii. packing of actin filaments in the stereocilia and in the cuticular plate and what happens to the organization when the stereocilia are bent. *The J. Cell Biol.*, 96(3):822–834, 1983.

[167] T. Torisawa, D. Taniguchi, S. Ishihara, and K. Oiwa. Spontaneous formation of a globally connected contractile network in a microtubule-motor system. *Biophys. J.*, 111(2):373–385.

[168] Seiji Umemoto and James R Sellers. Characterization of in vitro motility assays using smooth muscle and cytoplasmic myosins. *J. Biol. Chem.*, 265(25):14864–14869, 1990.

[169] R. Urrutia, M. A. McNiven, J. P. Albanesi, D. B. Murphy, and B. Kachar. Purified kinesin promotes vesicle motility and induces active sliding between microtubules in-vitro. *Proc. Natl. Acad. Sci. USA of the United States of America*, 88(15):6701–6705, 1991.

[170] David Vader, Alexandre Kabla, David Weitz, and Lakshminarayana Mahadevan. Strain-induced alignment in collagen gels. *PLOS ONE*, 4(6):e5902, 2009.

[171] Ronald D Vale, Fady Malik, and Diane Brown. Directional instability of microtubule transport in the presence of kinesin and dynein, two opposite polarity motor proteins. *J. Cell Biol.*, 119(6):1589–1596, 1992.

[172] Dimitrios Vavylonis, Jian-Qiu Wu, Steven Hao, Ben O'shaughnessy, and Thomas D Pollard. Assembly mechanism of the contractile ring for cytokinesis by fission yeast. *Science*, 319(5859):97–100, 2008.

[173] Claudia Veigel, Justin E. Molloy, Stephan Schmitz, and John Kendrick-Jones. Load-dependent kinetics of force production by smooth muscle myosin measured with optical tweezers. *Nat. Cell Biol.*, 5(11):980–986, 2003.

[174] Alexander B Verkhovsky and Gary G Borisy. Non-sarcomeric mode of myosin ii organization in the fibroblast lamellum. *The J. Cell Biol.*, 123(3):637–652, 1993.

[175] S. K. Vogel, Z. Petrasek, F. Heinemann, and P. Schwille. Myosin motors fragment and compact membrane-bound actin filaments. *Elife*, 2, 2013.

[176] Sam Walcott, David M. Warshaw, and Edward P. Debold. Mechanical coupling between myosin molecules causes differences between ensemble and single-molecule measurements. *Biophys. J.*, 103(3):501–510, 2012.

[177] Shenshen Wang and Peter G. Wolynes. Active contractility in actomyosin networks. *Proc. Natl. Acad. Sci. USA*, 109(17):6446–6451, 2012.

[178] Kimberly L Weirich, Shiladitya Banerjee, Kinjal Dasbiswas, Thomas A Witten, Suriyanarayanan Vaikuntanathan, and Margaret L Gardel. Liquid behavior of cross-linked actin bundles. *Proc. Natl. Acad. Sci. USA*, 114(9):2131–2136, 2017.

[179] Kimberly L Weirich, Jacob N Israelachvili, and D Kuchnir Fygenson. Bilayer edges catalyze supported lipid bilayer formation. *Biophys. J.*, 98(1):85–92, 2010.

[180] Matthew D Welch, Akihiro Iwamatsu, and Timothy J Mitchison. Actin polymerization is induced by arp 2/3 protein complex at the surface of listeria monocytogenes. *Nature*, 385(6613):265, 1997.

[181] Jan Wilhelm and Erwin Frey. Elasticity of stiff polymer networks. *Phys. Rev. Lett.*, 91(10):108103, 2003.

[182] Cyrus A Wilson, Mark A Tsuchida, Greg M Allen, Erin L Barnhart, Kathryn T Applegate, Patricia T Yam, Lin Ji, Kinneret Keren, Gaudenz Danuser, and Julie A Theriot. Myosin ii contributes to cell-scale actin network treadmilling through network disassembly. *Nature*, 465(7296):373–377, 2010.

[183] Jonathan D Winkelman, Cristian Suarez, Glen M Hocky, Alyssa J Harker, Alisha N Morganthaler, Jenna R Christensen, Gregory A Voth, James R Bartles, and David R Kovar. Fascin-and α-actinin-bundled networks contain intrinsic structural features that drive protein sorting. *Curr. Biol.*, 26(20):2697–2706, 2016.

[184] Daisuke Yamazaki, Shusaku Kurisu, and Tadaomi Takenawa. Regulation of cancer cell motil. through actin reorganization. *Cancer Sci.*, 96(7):379–386, 2005.

[185] Jing Yan, Andrew G. Sharo, Howard A. Stone, Ned S. Wingreen, and Bonnie L. Bassler. Vibrio cholerae biofilm growth program and architecture revealed by single-cell live imaging. *Proc. Natl. Acad. Sci. USA*, 113(36):E5337–E5343, 2016.

[186] Rui Zhang, Nitin Kumar, Jennifer L Ross, Margaret L Gardel, and Juan J de Pablo. Interplay of structure, elasticity, and dynamics in actin-based nematic materials. *Proc. Natl. Acad. Sci. USA*, page 201713832, 2017.

[187] A. Zidovska, D. A. Weitz, and T. J. Mitchison. Micron-scale coherence in interphase chromatin dynamics. *Proc. Natl. Acad. Sci. USA*, 110(39):15555–60, 2013.